

## 2021 届博士学位论文

# $^{87}\text{Rb}$ 玻色-爱因斯坦凝聚体的激发谱和相干现象

作者姓名 Sadiq Nawaz Khan

指导教师 张靖 教授

学科专业 光学

研究方向 超冷原子物理

培养单位 量子光学与光量子器件国家重点实验室

光电研究所

学习年限 2017 年 9 月至 2021 年 6 月

二〇二一年六月

山西大学

2021 届博士学位论文

# $^{87}\text{Rb}$ 玻色-爱因斯坦凝聚体的激发谱和相干现象

作者姓名 Sadiq Nawaz Khan

指导教师 张靖 教授

学科专业 光学

研究方向 超冷原子物理

培养单位 量子光学与光量子器件国家重点实验室

光电研究所

学习年限 2017 年 9 月至 2021 年 6 月

二〇二一年六月

**Thesis for Doctor's degree, Shanxi University, 2021**

Excitation spectrum and coherent phenomena in  $^{87}\text{Rb}$  Bose-Einstein condensates

Student Name	Sadiq Nawaz Khan
Supervisor	Prof. Jing Zhang
Major	Optics
Specialty	Ultracold atomic physics
Department	State Key Laboratory of Quantum Optics and Quantum Optics Devices Institute of Opto-Electronics
Research Duration	2017.09-2021.06

June, 2021

# Contents

ABSTRACT .....	VII
摘要 .....	X
Chapter 1: The Bose-Einstein condensation: Some important topics .....	1
1.1 Bose-Einstein Condensate as a platform for multidisciplinary science.....	1
1.2 Historical events leading to the realization of BEC.....	2
1.3 Density of a BEC and Temperature requirement .....	3
1.3.1 Role of trapping potential.....	4
1.3.2 Radius and shape of the BEC.....	7
1.4 Forces on an atom in a radiation field .....	9
1.4.1 Absorption of radiation by moving atoms .....	10
1.5 Thesis distribution .....	11
References .....	12
Chapter 2: Experimental setup .....	19
2.1 Saturation Absorption Spectroscopy .....	19
2.2 Magneto-Optical Trap (MOT).....	21
2.3 Compressed MOT and optical molasses.....	29
2.4 Optical pumping and evaporation in optically plugged magnetic trap.....	31
2.5 Evaporation in Dipole trap.....	35
2.6 Transfer to $ 1, 1\rangle$ state.....	38
2.7 Imaging the BEC .....	39
References .....	42
Chapter 3: Study of an N-Type atomic level system in a Bose-Einstein condensate.....	45
3.1 Introduction.....	45
3.2 Realization of an N-Type System in $^{87}\text{Rb}$ .....	47
3.3 Hamiltonian of the N-Type System .....	48
3.3.1 Equations of motion for the system density matrix .....	53
3.3.2 Solution to the equations of motion .....	55
3.4 Dressed state picture of the N-type System .....	56
3.5 Experimental procedure .....	58
3.6 Further properties of the N-type system .....	60

3.7 Summary and conclusions .....	65
References .....	67
Chapter 4: Photoassociation of the $^{87}\text{Rb}$ BEC near the D1 line threshold .....	71
4.1 Single photon photoprocesses between two atoms.....	71
4.2 Photoassociation of atoms in a BEC.....	73
4.3 Photoassociation threshold and asymptotic potentials .....	74
4.4 Photoassociation of $^{87}\text{Rb}$ near the D1 line threshold .....	76
4.4.1 Experimental Setup and experimental procedure .....	76
4.4.2 The PA spectra .....	79
4.4.3 Laser locking schemes for the Case 1 and Case 2 spectra .....	79
4.4.4 Discussion on the spectra .....	80
4.4.5 Trap loss spectra and its comparison to the Bragg scattering spectra.....	87
4.4.6 Anomalous broadening of the upper excited hyperfine transition .....	89
4.4.7 Red shift of the PA lines due to increase in power .....	90
4.5 Summary of the chapter .....	93
References .....	94
Chapter 5: Temporal dynamics of BEC in a 1D Optical Lattice.....	99
5.1 Kapitza-Dirac diffraction of the BEC.....	99
5.1.1 The grating picture of lattice diffraction .....	99
5.1.2 The Raman picture of lattice diffraction .....	100
5.2 Superradiance .....	105
5.3 Superradiance Lattice .....	108
5.4 Superposition of the SL on a phase modulated BEC.....	112
5.5 The Experiment and discussion .....	113
5.5.1 Experimental setup.....	114
5.5.2 Experimental sequence.....	116
5.6 Experimental Data .....	117
5.6.1 Effect of lattice power .....	117
5.6.2 Effect of delay on Peaks A1 and A2 .....	120
5.6.3 Effect of the dipole trap.....	122
5.6.4 Probe scattering when the coupling laser is turned OFF first .....	123

5.6.7 Effect of different powers in the two lattice beams .....	124
5.6.8 Effect of moving lattice.....	127
5.7 Summary.....	129
References .....	131
Appendix A .....	135
A.1 Biasing Circuit for IGBT .....	135
A.2 Adder Circuit .....	135
A.3 Feedback Circuit .....	136
A.4 Circuit for AOM switch ON/OFF.....	137
A.5 Circuit for Analog Optical Isolator/Analog box .....	138
A.6 Optical setup .....	139
A.7 RF driver (POS-PAS) circuit .....	140
A.8 PID for laser locking.....	141
A.9 Detector.....	142
A.10 OPLL Schematic.....	143
A.11 Circuit for Digital Optical Isolator/Digital Box.....	144
A.12 Amplifier circuit for shutter ON/OFF.....	145
Summary and outlook .....	146
Research achievements.....	148
Acknowledgments .....	149
Personal Profile .....	151
承 诺 书.....	152
学位论文使用授权声明 .....	153

# ABSTRACT

The 20<sup>th</sup> century saw a multitude of progress in every field of science and technology, especially in theoretical and experimental physics. One of the progresses in the field of atomic, molecular and optical physics was the prediction and the realization of the Bose-Einstein condensation of atomic gas at very low temperatures. The  $^{87}\text{Rb}$  BEC was the first to be realized in 1995 and many other atomic species were condensed shortly. The field of BEC later branched into several directions/disciplines while the BEC was acting as a starting point. These disciplines use the BEC to simulate complex physical systems in the laboratory with exceptional control over the tuning of the system parameters that would be difficult or sometimes impossible in the real world systems. This thesis also presents a series of such experiments which do not fall under a single specialty of physics but all are performed in the  $^{87}\text{Rb}$  BEC as a starting point and thus qualify under the umbrella of ultra-cold atomic physics.

In the starting two chapters, several theoretical and experimental topics (relevant to the field of BEC in general and to our laboratory setup in special) are discussed for the sake of completeness and then the three experiments performed as part of my PhD work are discussed in the remaining chapters. The necessary electronic circuit sketches and optical beam setups are listed in the appendix A in the end of the thesis.

The first of these experiments is the realization of the N-type system in the BEC by the application of three lasers to the BEC. Two of the lasers are phase locked by the optical phase lock loop system while the third one is locked independently and can still introduce and maintain the coherent effects in the  $^{87}\text{Rb}$  BEC. The N-type system is studied under the absorption imaging detection technique and all of the band structure/absorption spectral features are successfully retrieved using this method. This study serves as an important step in the use of BEC in applications like quantum information, atomic coherent experiments and the quantum memory. The behavior of the N-type system in the BEC under different driving and coupling laser detuning and intensities is both theoretically (using the density matrix method) and experimentally studied and its features are discussed. A very good

qualitative agreement of the theoretical and experimental data shows the power of absorption imaging as a probing tool and also of the BEC as an ideal platform for such atomic coherence experiments.

The second experiment is related to the formation of the  $^{87}\text{Rb}_2$  excited-state near-threshold molecules using the  $5^2\text{P}_{1/2}$  level as the threshold point, a process called photoassociation. This is done by shining a single laser tuned below and above the two excited hyperfine states of the said level. In our study, more than 40 quantized excited states are created and detected using two detection methods. The  $^{87}\text{Rb}$  BECs prepared in both the lower as well as the upper hyperfine ground state are excited to these excited molecular (dimer) states and both of the detection methods can detect the created molecular states but with variable accuracy. These states are never detected before and several of the previous attempts using magneto-optic traps (MOTs) or hotter atoms showed a continuous loss (in contrast to the quantized loss that we have detected) in this region of the frequency spectrum. The very low temperature of the BEC and the low power requirements by the BEC enabled us to create and detect these states with great precision. The effect of power broadening and energy shift of these states with the increasing laser power is also studied. An interesting feature is observed near the atomic resonance of the  $^{87}\text{Rb}$  which becomes anomalously broadened due to the mixing of the nearby excited molecular states. This broadening is so strong that the typical Lorentzian line-shape of the atomic resonance is destroyed and which is retrieved back only when a very weak photoassociation laser power is used. Similar broadening was observed in the pioneering experiments of atomic spectroscopy but the nearby quantized states were never detected at that time. We have observed from the experimental data that the use of Bragg scattering from an optical lattice in the BEC for the detection of these excited molecular states produces better results as compared to the trap loss/absorption imaging method. The possible reasons for this are also discussed in this thesis. I do not give any theoretical treatment of the detected molecular states and leave it for future study for the theoretical physics community.

The last experiment is performed with a superradiance lattice superposed on a phase modulated BEC. First the BEC is exposed to a blue detuned lattice for a variable time interval and then the superradiance lattice is turned ON to collect the phase information



using the superradiance scattering light. The BEC wave-function evolves under the first blue detuned lattice and at variable time delays the phase acquired by the wave-function is different. The superradiance lattice scattering carries this phase modulation information and acts as an in-situ method for the measurement of the phase imprinted on the BEC without waiting for the BEC to expand for a certain time of flight (TOF). The phase modulation affects the superradiance scattering in the form of oscillations in the intensity as a function of time and agrees well with the previously existing theory qualitatively. This experiment also includes the study and comparison of the effects of a moving lattice in two opposite directions on the net phase imprinted on the BEC. The phase imprinted by two simultaneous optical lattices (a super-lattice) at different powers of each lattice is also studied and the phase information revealed by the oscillation scattering light intensity agrees very well with what the theory should predict. The in-situ probing of the BEC phase removes the possible noise sources that are typically inherent to the TOF imaging probing experiments. This experiment is suitable for the study of the depths of complex optical lattice potentials which are hard to measure using the conventional methods.

**Key words:** Bose-Einstein condensates; Photoassociation; Laser induced atomic coherence; Superradiance lattice

## 摘要

20 世纪在科学技术的各个领域都取得了巨大的进步，尤其是在理论物理和实验物理方面。原子、分子和光学物理领域的进展之一是预测和实现了原子气体在极低温度下的玻色-爱因斯坦凝聚。 $^{87}\text{Rb}$  BEC 是 1995 年第一个实现玻色爱因斯坦凝聚的原子，随后其他许多原子很快也实现了凝聚。后来，以 BEC 作为一个起点，发展出了和玻色爱因斯坦相关的其他几个方向/学科。这些学科在 BEC 的基础上通过调节优化实验系统参数在实验室中模拟复杂的物理系统，这在现实世界的系统中是很困难的，有时甚至是不可能的。本文还介绍了一系列不属于单一物理专业的一系列实验，它们都是以  $^{87}\text{Rb}$  BEC 为起点进行的，因而符合超冷原子物理的范畴。

为了整个论文的完整起见，在开头的两章中，讨论了几个理论和实验观点(一般与 BEC 领域相关，特别与我们的实验室装置相关)，然后在剩下的几章中讨论了作为我博士工作中的三个实验。在本文最后的附录 A 中列出了所需的电子电路草图和光路装置。

第一个实验是利用三束激光在 BEC 中实现 N 型系统。其中两个激光器用光学锁相环系统锁相，第三个激光器独立锁相，仍然可以引入并维持  $^{87}\text{Rb}$  BEC 中的相干效应。在吸收成像技术下对 N 型系统进行了研究，并利用该方法成功地反演了所有的带结构/吸收光谱特征。这是 BEC 在量子信息、原子相干实验和量子存储等领域应用的重要一步。本文从理论上(利用密度矩阵方法)和实验上研究了不同驱动和耦合激光失谐和强度下 BEC 中 N 型系统的行为，并讨论了其特征。理论和实验数据符合的一致性表明了吸收成像作为探测工具的能力，也表明了 BEC 是做原子相干实验的理想平台。

第二个实验是关于以  $5^2\text{P}_{1/2}$  能级为阈值点形成  $^{87}\text{Rb}_2$  激发态近阈值分子的过程，这一过程称为光缔合。这是通过照射一个调谐在上述能级的两个激发态以下和以上的单一激光来实现的。在我们的研究中，通过两种检测方法有 40 多个量子化激发态被创建和检测。在超精细基态附近制备的  $^{87}\text{Rb}$  BECs 被激发到这些激发的分子(二聚体)态，用两种探测方法都可以检测生成的分子态，但精度不同。这些分子态以前从未被检测到过，而之前使用磁光阱(MOTs)或更热的原子进行的几次尝试显示，频谱

在这个区域出现了连续的损耗(与我们检测到的量子化损耗相反)。BEC 的非常低的温度和 BEC 的低功率要求,使我们能够产生一些分子态并且检测这些状态的精度很高。我们同时还研究了这些能级随激光功率增加而产生的功率展宽和能量位移的影响。在  $87\text{Rb}$  的原子共振附近观察到一个有趣的现象,它由于附近激发态的混合而变得异常加宽。这种展宽是如此之强,以至于原子共振的典型洛伦兹线形被破坏,只有在使用非常弱的光联合激光功率时才能探测到。类似的展宽现象也曾在原子光谱学的先驱实验中观察到,但当时从未检测到附近的量子化态。我们从实验数据中观察到,与陷阱损耗/吸收成像方法相比,利用光学晶格中的布拉格散射来检测这些激发态产生了更好的结果。本文还对造成这种现象的原因进行了探讨。对于检测到的分子态,我不做任何理论处理,而是把它留给理论物理范畴进行未来的研究。

最后,将超辐射晶格叠加在相位调制的 BEC 上进行了实验。首先,在可变的时间间隔内将 BEC 暴露在蓝色失谐晶格中,然后打开超辐射晶格,利用超辐射散射光收集相位信息。BEC 波函数在第一个蓝失谐晶格下的演化,在可变的时间延迟下,波函数得到的相位是不同的。超辐射晶格散射携带了这一相位调制信息同时作为一种无需等待 BEC 膨胀一段时间飞行(TOF)就可以测量 BEC 上携带的相位的原位方法。相位调制对超辐射散射的影响表现为强度随时间的振荡形式,并在定性上与已有理论相一致。本实验还包括研究和比较两个相反方向的移动晶格对 BEC 上印迹的净相的影响。同时研究了两个同步光晶格(超晶格)在每个晶格的不同功率下的相位印迹,振荡散射光强所揭示的相位信息与理论所预测的非常吻合。BEC 相位的原位探测消除了 TOF 成像探测实验固有的可能噪声源。本实验适用于传统方法难以测量的复杂光晶格势的深度研究。

**关键词:** 玻色爱因斯坦凝聚; 光缔合; 激光诱导原子相干; 超辐射光晶格



# **Chapter 1: The Bose-Einstein condensation: Some important topics**

## **1.1 Bose-Einstein Condensate as a platform for multidisciplinary science**

The BEC is such a tunable platform that it has become the testbed for the experimental quantum simulations of several fields of science in a similar way as predicted by Feynman<sup>[1]</sup> and is free from the long range coulomb interactions faced by the trapped ion systems<sup>[2]</sup>. For example, the BEC can be subjected to varying fields to induce or simulate patterns that are prevalent in galaxy filamentation<sup>[3]</sup> or the Unruh's radiation found near the black holes<sup>[4]</sup>. In addition to that, the study of many body interactions and the consequent emergent phenomena can be studied with ultra-cold atoms<sup>[5-10]</sup>. Although the BEC state is can be represented by a single wave-function, the interactions of the atoms making the BEC can be represented by a mean-field approximation. These interactions are tunable both optically and magnetically<sup>[11, 12]</sup>. Microscopic manipulation of atoms and the realization of nano-scale geometrical potentials is another field where ultra-cold atoms of the BEC find its way<sup>[13, 14]</sup>. Solid states physics environments are often simulated in BECs by loading them into optical lattices made from the interference fringes of laser beams<sup>[15-22]</sup>. Quantum optics and quantum information systems are also investigated in BECs by exploiting the practically zero thermal broadening of the linewidth and the suitable density of atoms in a BEC<sup>[23, 24]</sup>.

Similarly, molecules are condensed to the degenerate state using the BEC as a starting point<sup>[25]</sup>. Chemical physics related problems, like the excitation of molecules to excited states not allowed by selection rules or to very weakly bound states and the study of long and short range potentials are now easily and routinely tackled using BECs<sup>[26-28]</sup>. The coherence of matter waves of the BEC is used to perform precise gravitational force measurements and is proposed to detect the gravitational waves and also study the gravitational physics mixing with quantum physics<sup>[29]</sup>. In fact, the applications and potentials of the BEC are so enormous that it requires a dedicated book<sup>[30]</sup> but on the other hand, the same tabletop experimental setup can be easily modified for simulating any kind

of experimental environment as discussed above. The achievement of the BEC was not easy as it took a long time for several of the techniques used in the BEC preparation process to mature first. However, BEC production is now so matured that it is routinely produced on the international space station (ISS) being controlled remotely from the earth<sup>[31]</sup>.

## 1.2 Historical events leading to the realization of BEC

All the gasses at room temperature are composed distinguishable particles that obey classical statistics called the Maxwell-Boltzmann statistics. This statistics gives the number of distinguishable particles having a specific set of energies at room temperatures. Distinguishable means that each particle has a distinct set of energy, momentum and position and that their wave-functions do not overlap. However, when the temperature is cooled down, that the deBroglie wavelength  $\lambda_{dB}$  as well as the density of the gas increases. At very low temperatures,  $\lambda_{dB}$  becomes comparable to the inter-particle spacing and their wave-functions start to overlap and the quantum effects starts to show off and the particles starts to have identical energy, momentum and position (identical wave-functions called quantum numbers). The quantum effects then decides how many particles can share the same set of quantum numbers depending on whether the particles are Bosons (integer spin) or Fermions (half integral spin). Satyendranath Bose and Albert Einstein found that Bosons tend to clump up together as the temperature approaches the critical temperature<sup>[32, 33]</sup>. Experimental observation of BEC in dilute gasses was not possible until the maturity of several laser cooling and evaporative cooling techniques which then in 1995 lead to the first creation of BEC<sup>[34]</sup> in  $^{87}\text{Rb}$  and later in other atoms<sup>[35-40]</sup>.

Fermions on the other hand, are particles that can't occupy the same quantum state but they also become superfluid below the energy degeneracy temperature<sup>[41, 42]</sup>. Fermions have also been experimentally cooled down to degenerate fermi gas (DFG) temperature<sup>[43-48]</sup> using similar experimental strategies used for the creation of BECs. An interesting property of Fermions is that two Fermions below the degeneracy temperature can combine to form Bosonic molecules which then have the properties of a BEC<sup>[30, 49-51]</sup>.

The experimental achievement of the BECs and the DFGs were realized only after the laser spectroscopy, laser cooling and trapping techniques, magnetic trapping and the related

theory matured over several decades<sup>[52-59]</sup>. In the following, a brief introduction is given related to the important parameters that can identify a BEC from any other form of matter.

### 1.3 Density of a BEC and Temperature requirement

Both the density of the gas and the deBroglie wavelength (dependent on temperature and mass) of the particles are very important quantities. These quantities yield another quantity which is a measure of how much quantum-ness a system have e.g. the phase space density  $D = n\lambda_{dB}^3$  which, when reaches the value of 1, the classical statistics can no more describe the distribution of the particles and quantum statistics is needed. For comparison, the phase space density of  $^{87}\text{Rb}$  atoms at room temperature in typical vacuum systems (found in ultra-cold atomic physics experiments) is around  $10^{-22}$ . At a higher value of the phase space density ( $D \sim 2.612$ ), all the Bosons will accumulate in the same ground state of a confining potential (whether magnetic or optical). This condensed state of matter is what is now called the Bose-Einstein condensate or simply a BEC. This condensed portion of the gas can be very high in number (millions of atoms can occupy the ground state of the confining potential) and thus a BEC is a macroscopic system displaying quantum mechanical behavior. The single wave-function is also of macroscopic size and display a coherent macroscopic phase distribution over the BEC and can exhibit the interference phenomenon<sup>[60, 61]</sup>. The number density (particles per unit volume) in a BEC is in the range of  $10^{13}$ - $10^{15} \text{ cm}^{-3}$  as compared to the normal molecular number density in the ambient air which is  $10^{19} \text{ cm}^{-3}$ <sup>[30]</sup>. The lower density of the BEC allows for good optical access for the manipulation of atoms in different experiments in the BEC and for the achievement of the BEC in the first place. Other factors that set the low density requirement is the particle-particle interactions. Inter-particle interactions at higher densities turn the gas into liquid (or solid or even molecular) state before the BEC stage arrives. That is why some atomic species having strong interactions even at such low densities need special magnetic fields for tuning of their scattering lengths to avoid the strong inter-particle interactions while near the BEC temperatures<sup>[62, 63]</sup>. Also, to get a large number of atoms in the single ground state, lower density and low interactions are desired as in the case of superfluid  $^4\text{He}$  where the zero momentum state atom number is very small due to the inter-particle interactions due to high

density<sup>[64, 65]</sup>. The number density in liquid and solid state of matter is  $10^{22} \text{ cm}^{-3}$  and inside the nucleus it is  $10^{38} \text{ cm}^{-3}$ . The requirement of low density of the BEC also requires that the temperature of the gas (to be condensed into a single quantum state) should be very low to make it behave quantum mechanically. Indeed, the temperature required for the observation of the quantum behavior decreases with the density. For example, quantum behavior in nuclei can be observed at temperatures as high as  $10^{11} \text{ K}$  while for BEC it is in the sub-micro Kelvin range.

The above requirements and limitations led to the search of atomic species which does not change its gaseous atomic form even at lower temperature. The first candidate was the hydrogen atom<sup>[66]</sup> which was cooled using cryogenic techniques but it was still far above the required BEC critical temperature. However, the magnetic trapping techniques developed during these experiments together with the availability of tunable lasers lead to the final achievement of BEC in 1995.

### 1.3.1 Role of trapping potential

The temperature of the BEC can be calculated using some simple arguments. The current experimental methods of creating the BEC uses the evaporation of hotter atoms for the cooling of the remaining atoms inside a confining trap (may be magnetic or optical). In the final stages of the evaporation process, the trapping potential is weak and can be approximated by a harmonic oscillator type potential

$$V(r) = \frac{1}{2}m(\omega_x^2x^2 + \omega_y^2y^2 + \omega_z^2z^2) \quad (1.1)$$

where  $\omega_i$  are the trapping frequencies in the three directions. The density of states for a harmonic potential of Eq. (1.1) then becomes

$$g(\epsilon) = \frac{1}{2(\hbar\bar{\omega})^3}\epsilon^2 \quad (1.2)$$

where  $\bar{\omega} = (\omega_x\omega_y\omega_z)^{1/3}$  is the geometric mean of the three trapping frequencies and  $\epsilon$  is the energy of a given state. Now, for a Bosonic gas at very low temperature  $T$  where quantum behavior is prominent, the gas particles will try to distribute among the available energy states according to the Bose-Einstein statistics distribution function



Chapter 1: The Bose-Einstein condensation: Some important topics

$$f(\epsilon) = \frac{1}{e^{(\epsilon-\mu)/k_B T} - 1} \quad (1.3)$$

where  $k_B$  is the Boltzmann constant and the chemical potential  $\mu$  is coming from the requirement of atom number conservation. From Eq. (1.3), we can see that for  $\epsilon = 0$  i.e. the ground state, when the temperature is near zero,  $\lim_{T \rightarrow 0} e^{-\mu/T} \approx 1$  and thus Eq. (1.3) will blow up (give a large number of particles in the ground state) showing that the atoms are occupying the ground state of the trapping potential. The ground state atoms represents the condensed part of the total gas but there will be still atoms in other states depending on how much strong is the trapping potential. The number of atoms in the condensed part will however be very large. The total number of atoms (sum of condensed ground state atoms  $N_0$  and non-condensed excited state atoms  $N_{exc}$ ) can be found by

$$N_T = N_0 + N_{exc} = \sum_{\epsilon} f(\epsilon) \quad (1.4)$$

The summation can be converted into integration if the energy separation between the trapping potential states is small however, then we should also write the condensed part separately, as

$$N_T = N_0 + N_{exc} = N_0 + \int_0^{\infty} g(\epsilon) f(\epsilon) d\epsilon \quad (1.5)$$

Suppose  $\epsilon = p^2/2m + V$ , where  $p$  is the momentum and  $m$  is the mass of the particle and  $V$  is the trapping potential. Let us first consider a general case of the trapping potential and introduce the variable  $x = p^2/2mk_B T$  and by definition of the density of states in a general potential  $g(\epsilon) = \frac{V}{4\pi^2} \left(\frac{2m}{\hbar^2}\right)^{3/2}$  ( $V$  being the volume of the trapping potential holding the atoms), then the excited state part of the atoms (Eq. 1.5) becomes

$$n_{exc} = \frac{N_{exc}}{V} = \frac{2}{\sqrt{\pi} \lambda_{dB}^3} \int_0^{\infty} \frac{\sqrt{x}}{z^{-1} e^x - 1} dx \quad (1.6)$$

where  $n_{exc} = \frac{N_{exc}}{V}$  is the number density of the excited states atoms held by the trapping

potential  $V$ . The deBroglie wavelength is defined by  $\lambda_{dB} = \left(\frac{2\pi\hbar^2}{mk_B T}\right)^{\frac{1}{2}}$  and the parameter  $z = e^{\frac{[\mu-V]}{k_B T}}$  carries the information of the trapping potential and interesting consequences follow

from this parameter. Solving the Eq. (1.6) for the excited states number density in the trapping potential  $V$  gives

$$n_{exc} = \frac{g_{3/2}(z)}{\lambda_{dB}^3} \quad (1.7)$$

The numerator in Eq. (1.7) is called a polylogarithm function and its general form is given by the summation

$$g_{\gamma}(z) = \sum_{n=1}^{\infty} \frac{z^n}{n^{\gamma}} \quad (1.8)$$

If we consider a uniform potential (say  $V=0$ ) and for ideal gas we use  $\mu \leq 0$ , the parameter  $z = e^{\frac{[\mu-V]}{k_B T}}$  approaches unity and thus  $g_{3/2}(z) = 2.612$  and putting this in Eq. (1.7) shows that at a fixed temperature (for which  $z \rightarrow 1$ ) the density of the excited state atoms will not increase any more but will reach its saturation point (as  $\lambda_{dB}^3$  also does not change at constant temperature so the density approaches  $n_{crit} = 2.612/\lambda_{dB}^3$ ). Now, as the volume of any trapping potential is finite, adding more atoms to the same volume will not go to the excited state as the excited state density is already saturated, thus atoms will now start to go to the ground condensed state and thus macroscopic condensation will occur. This temperature is called the critical temperature and depends on the type and shape of the potential and also on the interatomic interaction strength. Using  $g_{3/2}(z) = 2.612$  in Eq. (1.7) together with the definition of  $\lambda_{dB}$  and solving for the temperature gives this critical temperature, which for the  $V=0$  potential is

$$T_c = \frac{2\pi\hbar^2}{mk_B} \left( \frac{n}{g_{3/2}(1)} \right)^{2/3} \quad (1.9)$$

This is the critical temperature for an ideal gas in a  $V=0$  potential and below this temperature no more atoms will be added to the excited state and all the additional atoms should go to the ground state. At this temperature, all the atoms will still occupy the excited states. So, using Eq. (1.9) and Eq. (1.5) we can find the fraction of the condensed atoms at a temperature below the critical temperature

$$\frac{N_0}{N_T} = 1 - \left( \frac{T}{T_c} \right)^{3/2} \quad (1.10)$$

Now, using the harmonic oscillator potential of Eq. (1.1) and the density of states of Eq. (1.2), Eq. (1.6) gives the expression for the critical temperature

$$T_c = \frac{\hbar\bar{\omega}}{k_B} \left( \frac{N_T}{\zeta(3)} \right)^{1/3} \quad (1.11)$$

where the Riemann zeta function is given by  $\zeta(x) = \sum_{n=1}^{\infty} n^{-x}$ . At a temperature well below the critical temperature, all the atoms should occupy the ground state and thus the atoms in the ground state can be calculated from Eq. (1.11) as

$$N_c = \zeta(3) \left( \frac{k_B T}{\hbar\bar{\omega}} \right)^3 \quad (1.12)$$

again, the fraction of condensed atoms, when not all the atoms are in the ground state of the trapping potential, is given by

$$\frac{N_0}{N_T} = 1 - \left( \frac{T}{T_c} \right)^3 \quad (1.13)$$

Therefore, Eq. (1.1) to (1.13) shows that the nature of the trapping potential affects both the temperature and the fraction of the condensed part of the trapped atoms. Another important point to note is that since the BEC wave-function is the same as the ground state wave-function of the trapping potential, it is thus different for different trapping potentials. The coherence length of the BEC also changes with the trapping potential<sup>[67]</sup>.

All these calculations suppose an ideal non-interacting gas of atoms. However, real gasses do interact and the onset of the critical temperature, the number of atoms in the ground state, the chemical potential and the shape of the ground state wave-function, all are affected by these interactions. The interactions can be taken into account by the use of the non-linear Schrodinger's equation which is also called the Gross-Pitaevskii (GP) equation. These interactions are very important and are utilized by the various experimental schemes used for the realization of condensation temperatures.

### 1.3.2 Radius and shape of the BEC

One particular use of the GP equation is the calculation of the ground state wave-function in the presence of interactions. The GP equation incorporates the interactions in the form of an extra term proportional to the square modulus of the wave-function  $\psi$ , making the Schrodinger's equation non-linear

$$\left( \frac{-\hbar^2}{2m} \nabla^2 + V(r) + g|\psi|^2 \right) \psi = \mu\psi \quad (1.14)$$

where  $g = \frac{4\pi\hbar^2 a}{m}$  is called the scattering strength and  $a$  is called the s-wave scattering length.

Because the temperature is very low, the kinetic energy term of the condensed atoms wave-

function can be dropped (this is called the Thomas-Fermi approximation) thus reducing the Eq. (1.14) to

$$(V(r) + g|\psi|^2)\psi = \mu\psi \quad (1.15)$$

or

$$n(r) = |\psi|^2 = \frac{\mu - V(r)}{g} \quad (1.16)$$

From Eq. (1.16), we can see that the density will drop to zero at  $V(r) = \mu$  (in other words, the BEC boundary does not exist beyond the region when the trapping potential reaches the chemical potential). Putting this value of the potential in Eq. (1.1) gives the Thomas-Fermi radius of the condensed cloud of atoms (or the size of the harmonic oscillator ground state wave-function in the case of a harmonic oscillator type potential)

$$R_j^2 = \frac{2\mu}{m\omega_j^2} \quad (1.17)$$

where  $j=x, y, z$  are the Cartesian axis. The solution of Eq. (1.16) for the harmonic oscillator potential (using Eq. 1.17) gives a parabolic (inverted parabola) type of density distribution

$$n(r) = |\psi|^2 = n_0 \left( 1 - \frac{x^2}{R_x^2} - \frac{y^2}{R_y^2} - \frac{z^2}{R_z^2} \right) \quad (1.18)$$

This (Eq. 1.18) type of density distribution is usually realized in the dipole trapping potentials that at lower depths can be approximated to the harmonic potential. The shapes of the BECs in such traps are indeed elongated in one direction while shortened in the other two directions because the harmonic oscillator type potentials in the optical dipole traps are tighter in one direction and looser in the others.

In the following chapter, various setups and stages of cooling of the atomic gas of  $^{87}\text{Rb}$  are discussed that we (and most of the ultra-cold atom labs around the world) use to arrive to the degenerate temperatures. Here, a theoretical briefing is presented to the cooling process of atoms involving light.

## 1.4 Forces on an atom in a radiation field

The starting point for the cooling of the  $^{87}\text{Rb}$  atoms is its cooling by laser light, therefore, it is important to understand the interaction of atoms with light. In the electric dipole picture of the atom, the interaction of atoms in a light field of electric field amplitude  $E$  is represented by the interaction between the electric field of the light and the induced electron dipole moment  $e.r$  and the resulting interaction energy is  $H = -er.E$ . The gradient of this energy is the radiation force experienced by the atom  $F_{rad} = -\langle \frac{\partial H}{\partial z} \rangle$ . To properly quantify the induced atomic dipole moment (between the ground state  $g$  and excited state  $e$  of the two level atom) and its dependence on the frequency of the applied radiation field, the Rabi frequency is a useful parameter, which is defined by  $\Omega = \frac{-eE}{\hbar} \langle e|r|g \rangle$ . Using this in the definition of the radiation force, we arrive at the equation for the radiation force on the atoms<sup>[68]</sup>

$$F_{rad} = \hbar \left( \frac{\partial \Omega}{\partial z} \rho_{eg}^* + \frac{\partial \Omega^*}{\partial z} \rho_{eg} \right) \quad (1.19)$$

where  $\rho_{eg}$  is the quantum coherence between the two states of the atom introduced by the applied light field and is given by<sup>[69]</sup>

$$\rho_{eg} = i \frac{\Omega}{2(\Gamma/2 - i\delta)(1 + s)} \quad (1.20)$$

where  $\Gamma$ ,  $\delta$  and  $s$  are respectively the linewidth of the atomic transition from  $g$  to  $e$ , the detuning of the applied laser field from the same atomic transition and the saturation

parameter which is defined by  $s = \frac{2\Omega^2/\Gamma^2}{1 + 4\delta^2/\Gamma^2}$ . Putting Eq. (1.20) in Eq. (1.19) and using the

rotating wave approximation (and a lot of algebra) results in the radiation force relationship that can further be separated into two parts i.e.

$$F_{rad} = F_{dip} + F_{scat} \quad (1.21)$$

where the first term of the force called the dipole force, is proportional to the gradient of the laser intensity  $I$  and is given by<sup>[70-72]</sup>

$$F_{dip} = -\frac{\hbar\delta}{2} \cdot \frac{\nabla \left( \frac{I}{I_s} \right)}{1 + I/I_s + 4\delta^2/\Gamma^2} \quad (1.22)$$

and the second term, called the scattering force, which is proportional to the intensity  $I$  of the light, is given by

$$F_{scat} = \frac{\hbar\Gamma k}{2} \cdot \frac{I/I_s}{1 + I/I_s + 4\delta^2/\Gamma^2} \quad (1.23)$$

where the saturation intensity is defined by  $I_s = \pi\hbar c/3\tau\lambda_0^3$  ( $I_s = 3.58 \text{ mW/cm}^2$  for  $^{87}\text{Rb}$  for the D2 line transition), and the relation between the laser intensity and the electric field amplitude of the laser beam is given by  $I = \frac{\epsilon_0 c E^2}{2}$ . Both kinds of forces are exploited during different steps of the sequence in the experimental setup used for the achievement of BEC in the ultra-cold atomic physics labs.

The scattering force is dominant when the laser light detuning from the given atomic transition is not large and is used to cool and trap the atoms during the magneto-optical trapping stage of the cooling process. The scattering force resulting from the absorption of photons is responsible for stripping away the energetically moving atoms from their kinetic energy during. The dipole force term is dominant when the laser detuning is very large and is utilized in the optical dipole trapping stage of the cooling process and also in the sub-Doppler cooling of atoms and in the trapping of atoms in the optical lattices.

#### 1.4.1 Absorption of radiation by moving atoms

The relativistic effect on the position of resonance frequency of the atoms is called the Doppler shift. Doppler shift  $\delta_{dop}^\pm$  is velocity dependent and thus the amount of shift in the transition frequency is directly proportional to the velocity “ $v$ ” of the atom ( $\delta_{dop}^\pm = \delta \mp kv$ ). Since the atoms at room temperature have a large range of velocities, the absorption spectrum of a given sample of atoms also show up as a broadened one, centered at the resonance frequency. The broadening is sometimes several hundreds of times that of the natural linewidth of the given transition. The lasers used in the atomic physics labs are usually frequency locked and thus can only excite a small portion of these room temperature atoms and the remaining atoms remain transparent to the laser light due to the low linewidth of the locked lasers.

If an atom is moving along the  $+z$ -axis and we shine two counter-propagating laser beams along the same axis, then the scattering force of Eq. (1.23) experienced by the atom from each laser beam will be different due to its motion direction. Suppose the force from

the beam travelling opposite to the atomic motion is  $F_+$  and from the beam traveling along the atom is  $F_-$ , then we can write the total scattering force as

$$F_{scat} = F_+ + F_- = \frac{\hbar\Gamma k}{2} \cdot I/I_s \left( \frac{1}{1+I/I_s + \left(\frac{2\delta_{dop}^+}{\Gamma}\right)^2} - \frac{1}{1+I/I_s + \left(\frac{2\delta_{dop}^-}{\Gamma}\right)^2} \right) \quad (1.24)$$

By choosing a proper detuning, this force (Eq. (1.24)) can be made negative which means that the atom can be slowed down in the z-direction. Applying three pairs of orthogonal beams, the atom can be cooled in all the directions, a scheme used in the optical molasses step of the laser cooling process. In terms of photon absorption-emission kicks received by the atom, Eq. (1.24) shows that the kicks received by the atom can be restricted in a particular direction only and the other direction kicks can be suppressed with the help of a proper choice of laser detuning. This property of controlled directional absorption is used in the trapping of the atoms in the magneto-optical traps that we will discuss in the next chapter.

## 1.5 Thesis distribution

The thesis are arranged as follows. The second chapter introduces various experimental setups and terminologies that are related to the experimental production of the BEC. Chapter 3 discusses the simulation of an N-type system in the BEC and presents the absorption imaging/trap loss technique to retrieve the absorption spectrum of the coherent system. Chapter 4 presents the observation more than 40 of the weakly bound excited state molecular states of  $^{87}\text{Rb}_2$  (dimer). The comparison of the spectra recorded with Bragg scattering and absorption imaging is also discussed in view of the amount of noise and the sources of noise in each spectra. Chapter 5 discusses the superradiance lattice and the temporal phase development study of a lattice using the superradiance emission from the superradiance lattice. The temporal phase delay between the dominant superradiance states of the superradiance lattice band is also discussed. The ‘‘appendix A’’ lists the important circuits’ sketches that are used in the experimental setup.

## References

- [1] R.P. Feynman. Simulating physics with computers. *International Journal of Theoretical Physics*, 1982, 21, 467.
- [2] R. Blatt and C. F. Roos. Quantum simulations with trapped ions. *Nature Physics*, 2012, 8, 277.
- [3] Z. Zhang, K. Yao, L. Feng, J. Hu, and C. Chin. Pattern formation in a driven Bose–Einstein condensate. *Nature Physics*, 2020, 16, 652.
- [4] J. Hu, L. Feng, Z. Zhang, and C. Chin. Quantum simulation of Unruh radiation. *Nature Physics*, 2019, 15, 785.
- [5] I. Bloch, J. Dalibard, and W. Zwerger. Many-body physics with ultracold gases. *Rev. Mod. Phys.*, 2008, 80, 885.
- [6] N. Navon, A. L. Gaunt, R. P. Smith, and Z. Hadzibabic. Emergence of a turbulent cascade in a quantum gas. *Nature*, 2016, 539, 72.
- [7] R. J. Fletcher, R. Lopes, J. Man, N. Navon, R. P. Smith, M. W. Zwierlein, and Z. Hadzibabic. Two- and three-body contacts in the unitary Bose gas. *Science*, 2017, 355, 377.
- [8] C. Eigen, J. A. P. Glidden, R. Lopes, E. A. Cornell, R. P. Smith, and Z. Hadzibabic. Universal prethermal dynamics of Bose gases quenched to unitarity. *Nature*, 2018, 563, 221.
- [9] A. Lukin, M. Rispoli, R. Schittko, M. E. Tai, A. M. Kaufman, S. Choi, V. Khemani, J. Léonard, and M. Greiner. Probing entanglement in a many-body–localized system. *Science*, 2019, 364, 256.
- [10] M. E. Tai, A. Lukin, M. N. Rispoli, R. Schittko, T. Menke, D. Borgnia, P. M. Preiss, F. Grusdt, A. M. Kaufman, and M. Greiner. Microscopy of the interacting Harper–Hofstadter model in the two-body limit. *Nature*, 2017, 546, 519.
- [11] C. Chin, R. Grimm, P. Julienne, and E. Tiesinga. Feshbach resonances in ultracold gases. *Rev. Mod. Phys.*, 2010, 82, 1225.
- [12] T. L. Nicholson, S. Blatt, B. J. Bloom, J. R. Williams, J. W. Thomsen, J. Ye, and Paul S. Julienne. Optical Feshbach resonances: Field-dressed theory and comparison with experiments. *Phys. Rev. A*, 2015, 92, 022709.



- [13] K. Wen, Z. Meng, P. Wang, L. Wang, L. Chen, L. Huang, L. Zhou, X. Cui and J. Zhang. Observation of sub-wavelength phase structure of matter wave with two-dimensional optical lattice by Kapitza-Dirac diffraction. *Scientific Reports*, 2020, 10, 5870.
- [14] A. V. Gorshkov, L. Jiang, M. Greiner, P. Zoller, and M. D. Lukin. Coherent Quantum Optical Control with Subwavelength Resolution. *phys. Rev. Lett.*, 2008, 100, 093005.
- [15] E. Zohar, J. I. Cirac and B. Reznik. Quantum simulations of lattice gauge theories using ultracold atoms in optical lattices. *Rep. Prog. Phys.*, 2015, 79, 014401.
- [16] U. J. Wiese. Ultracold quantum gases and lattice systems: quantum simulation of lattice gauge theories. *Annalen der Physik*, 2013, 525, 777.
- [17] L. W. Clark, B. M. Anderson, L. Feng, A. Gaj, K. Levin, and C. Chin. Observation of Density-Dependent Gauge Fields in a Bose-Einstein Condensate Based on Micromotion Control in a Shaken Two-Dimensional Lattice. *Phys. Rev. Lett.*, 2018, 121, 030402.
- [18] N. Goldman, G. Juzeliūnas, P. Öhberg, and I. B. Spielman. Light-induced gauge fields for ultracold atoms. *Rep. Prog. Phys.*, 2014, **77**, 126401.
- [19] W. S. Bakr, A. Peng, M. E. Tai, R. Ma, J. Simon, J. I. Gillen, S. Fölling, L. Pollet, and M. Greiner. Probing the Superfluid-to-Mott Insulator Transition at the Single-Atom Level. *Science*, 2010, 329, 547.
- [20] J. Simon, W. S. Bakr, R. Ma, M. E. Tai, P. M. Preiss, and M. Greiner. Quantum simulation of antiferromagnetic spin chains in an optical lattice. *Nature*, 2011, 472, 307.
- [21] W. S. Bakr, P. M. Preiss, M. E. Tai, R. Ma, J. Simon, and M. Greiner. Orbital excitation blockade and algorithmic cooling in quantum gases. *Nature*, 2011, 480, 500.
- [22] W. S. Bakr, J. I. Gillen, A. Peng, S. Fölling, and M. Greiner. A quantum gas microscope for detecting single atoms in a Hubbard-regime optical lattice. *Nature*, 2009, 462, 74.
- [23] L. Chen, P. Wang, Z. Meng, L. Huang, H. Cai, D. Wang, S. Zhu, and J. Zhang. Experimental Observation of One-Dimensional Superradiance Lattices in Ultracold Atoms. *Phys. Rev. Lett.*, 2018, 120, 193601.
- [24] P. Wang, L. Chen, C. Mi, Z. Meng, L. Huang, K. S. Nawaz, H. Cai, D. Wang, S. Zhu, and J. Zhang. Synthesized magnetic field of a sawtooth superradiance lattice in Bose-Einstein condensates. *npj Quantum Information*, 2020, 6, 18.

## Excitation spectrum and coherent phenomena in $^{87}\text{Rb}$ Bose-Einstein condensates

- [25] M. W. Zwierlein, C. A. Stan, C. H. Schunck, S. M. F. Raupach, S. Gupta, Z. Hadzibabic, and W. Ketterle. Observation of Bose-Einstein Condensation of Molecules. *Phys. Rev. Lett.*, 2003, 91, 250401.
- [26] K. S. Nawaz, L. Chen, C. Mi, Z. Meng, L. Huang, P. Wang, and J. Zhang. Photoassociation spectroscopy of weakly bound  $^{87}\text{Rb}_2$  molecules near the  $5P_{1/2}+5S_{1/2}$  threshold by optical Bragg scattering in Bose-Einstein condensates. *Phys. Rev. A*, 2020, 102, 053326.
- [27] J. G. Danzl, E. Haller, M. Gustavsson, M. J. Mark, R. Hart, N. Bouloufa, O. Dulieu, H. Ritsch, and H. C. Nägerl. Quantum Gas of Deeply Bound Ground State Molecules. *Science*, 2008, 321, 1062.
- [28] M. Junker, D. Dries, C. Welford, J. Hitchcock, Y. P. Chen, and R. G. Hulet. Photoassociation of a Bose-Einstein Condensate near a Feshbach Resonance. *Phys. Rev. Lett.*, 2008, 101, 060406.
- [29] G. M. Tino, A. Bassi, G. Bianco, K. Bongs, P. Bouyer, L. Cacciapuoti, S. Capozziello, X. Chen, M. L. Chiofalo, A. Derevianko, W. Ertmer, N. Gaaloul, P. Gill, P. W. Graham, J. M. Hogan, L. Iess, M. A. Kasevich, H. Katori, C. Klempt, X. Lu, L. Ma, H. Müller, N. R. Newbury, C. W. Oates, A. Peters, N. Poli, Er. M. Rasel, G. Rosi, A. Roura, C. Salomon, S. Schiller, W. Schleich, D. Schlippert, F. Schreck, C. Schubert, F. Sorrentino, U. Sterr, J. W. Thomsen, G. Vallone, F. Vetrano, P. Villoresi, W. von Klitzing, D. Wilkowski, P. Wolf, J. Ye, N. Yu, and M. Zhan. SAGE: A proposal for a space atomic gravity explorer. *Eur. Phys. J. D*, 2019, 73, 228.
- [30] C. J. PETHICK and H. SMITH. BOSE-EINSTEIN CONDENSATION IN DILUTE GASES. New York, Cambridge University Press. Second ed. 2008.
- [31] D. C. Aveline, J. R. Williams, E. R. Elliott, C. Dutenhoffer, J. R. Kellogg, J. M. Kohel, N. E. Lay, K. Oudrhiri, R. F. Shotwell, N. Yu, and R. J. Thompson. Observation of Bose-Einstein condensates in an Earth-orbiting research lab. *Nature*, 2020, 582, 193.
- [32] S.N. Bose. Plancks Law and Light Quantum Hypothesis. *Zeitschrift für Physik*, 1924, 26, 178.
- [33] A. Einstein. Quantentheorie des einatomigen idealen Gases. *Sitzungsberichte der Preussischen Akademie der Wissenschaften*, 1925, XXII 1924, 261.

## Chapter 1: The Bose-Einstein condensation: Some important topics

- [34] M. H. Anderson, J. R. Ensher, M. R. Matthews, C. E. Wieman, and E. A. Cornell. Observation of Bose-Einstein Condensation in a Dilute Atomic Vapor. *Science*, 1995, 269, 198.
- [35] T. Weber, J. Herbig, M. Mark, H. C. Nägerl, and R. Grimm. Bose-Einstein Condensation of Cesium. *Science*, 2003, 299, 232.
- [36] K. B. Davis, M. -O. Mewes, M. R. Andrews, N. J. van Druten, D. S. Durfee, D. M. Kurn, and W. Ketterle. Bose-Einstein Condensation in a Gas of Sodium Atoms. *Phys. Rev. Lett.*, 1995, 75, 3969.
- [37] C. C. Bradley, C. A. Sackett, J. J. Tollett, and R. G. Hulet. Evidence of Bose-Einstein Condensation in an Atomic Gas with Attractive Interactions. *Phys. Rev. Lett.*, 1995, 75, 1687.
- [38] S. L. Cornish, N. R. Claussen, J. L. Roberts, E. A. Cornell, and C. E. Wieman. Stable  $^{85}\text{Rb}$  Bose-Einstein Condensates with Widely Tunable Interactions. *Phys. Rev. Lett.*, 2000, 85, 1795.
- [39] G. Modugno, G. Ferrari, G. Roati, R. J. Brecha, A. Simoni, and M. Inguscio. Bose-Einstein Condensation of Potassium Atoms by Sympathetic Cooling. *Science*, 2001, 294, 1320.
- [40] A. Robert, O. Sirjean, A. Browaeys, J. Poupard, S. Nowak, D. Boiron, C. I. Westbrook, and A. Aspect. A Bose-Einstein Condensate of Metastable Atoms. *Science*, 2001, 292, 461.
- [41] E. Fermi. Zur Quantelung des idealen einatomigen Gases. *Zeitschrift für Physik*, 1926, 36, 902.
- [42] P.A.M. Dirac. On the Theory of Quantum Mechanics. *Proc. Roy. Soc. A*, 1926, 112, 661.
- [43] T. B. Ottenstein, T. Lompe, M. Kohnen, A. N. Wenz, and S. Jochim. Collisional Stability of a Three-Component Degenerate Fermi Gas. *Phys. Rev. Lett.*, 2008, 101, 203202.
- [44] B. DeMarco and D. S. Jin. Onset of Fermi Degeneracy in a Trapped Atomic Gas. *Science*, 1999, 285, 1703.
- [45] S. Aubin, S. Myrskog, M. H. T. Extavour, L. J. LeBlanc, D. McKay, A. Stummer, and J. H. Thywissen. Rapid sympathetic cooling to Fermi degeneracy on a chip. *Nature Physics*, 2006, 2, 384.

- [46] K. M. O'Hara, S. L. Hemmer, M. E. Gehm, S. R. Granade, and J. E. Thomas. Observation of a Strongly Interacting Degenerate Fermi Gas of Atoms. *Science*, 2002, 298, 2179.
- [47] S. R. Granade, M. E. Gehm, K. M. O'Hara, and J. E. Thomas. All-Optical Production of a Degenerate Fermi Gas. *Phys. Rev. Lett.*, 2002, 88, 120405.
- [48] T. Fukuhara, Y. Takasu, S. Sugawa, and Y. Takahashi, Quantum Degenerate Fermi Gases of Ytterbium Atoms. *Journal of Low Temperature Physics*, 2007, 148, 441.
- [49] M. Greiner, C. A. Regal, and D. S. Jin. Emergence of a molecular Bose-Einstein condensate from a Fermi gas. *Nature*, 2003, 426, 537.
- [50] S. Jochim, M. Bartenstein, A. Altmeyer, G. Hendl, S. Riedl, C. Chin, J. H. Denschlag, and R. Grimm. Bose-Einstein Condensation of Molecules. *Science*, 2003, 302, 2101.
- [51] M.W. Zwierlein, C.A. Stan, C.H. Schunck, S.M.F. Raupach, S. Gupta, Z. Hadzibabic, and W. Ketterle. Observation of Bose-Einstein Condensation of Molecules. *Phys. Rev. Lett.*, 2003, 91, 250401.
- [52] T. W. Hänsch and A. L. Schawlow. Cooling of gases by laser radiation. *Optics Comm.*, 1975, 13, 68.
- [53] A. Ashkin. Trapping of atoms by resonance radiation pressure. *Phys. Rev. Lett.*, 1978, 40, 729.
- [54] S. Andreev, V. Balykin, V. Letokhov, and V. Minogin. Radiative slowing and reduction of the energy spread of a beam of Sodium atoms to 1.5K in an oppositely directed laser beam. *JETP Lett.*, 1981, 34, 442.
- [55] W. D. Phillips and H. Metcalf. Laser deceleration of an atomic beam. *Phys. Rev. Lett.*, 1982, 48, 596.
- [56] J. Dalibard and C. Cohen-Tannoudji. Laser cooling below the Doppler limit by polarization gradients: simple theoretical models. *J. Opt. Soc. Am. B*, 1989, 6, 2023.
- [57] J. Dalibard and C. Cohen-Tannoudji. Dressed-atom approach to atomic motion in laser light: the dipole force revisited. *J. Opt. Soc. Am. B*, 1985, 2, 1707.
- [58] P. J. Ungar, D. S. Weiss, E. Riis, and S. Chu. Optical molasses and multilevel atoms: Theory. *J. Opt. Soc. Am. B*, 1989, 6, 2058.

## Chapter 1: The Bose-Einstein condensation: Some important topics

- [59] D. S. Weiss, E. Riis, Y. Shevy, P. J. Ungar, and S. Chu. Optical molasses and multilevel atoms: Experiment. *J. Opt. Soc. Am. B*, 1989, 6, 2072.
- [60] M. R. Andrews, C. G. Townsend, H.-J. Miesner, D. S. Durfee, D. M. Kurn, and W. Ketterle. Observation of Interference Between Two Bose Condensates. *Science*, 1996, 275, 637.
- [61] S. M. Barnett, S. Franke-Arnold, A. S. Arnold and C. Baxter. Coherence length for a trapped Bose gas. *J. Phys. B: At. Mol. Opt. Phys.*, 2000, 33, 4177.
- [62] G. Roati, M. Zaccanti, C. D'Errico, J. Catani, M. Modugno, A. Simoni, M. Inguscio, and G. Modugno.  $^{39}\text{K}$  Bose-Einstein Condensate with Tunable Interactions. *Phys. Rev. Lett.*, 2007, 99, 010403.
- [63] R. L. D. Campbell, R. P. Smith, N. Tammuz, S. Beattie, S. Moulder, and Z. Hadzibabic. Efficient production of large  $\text{K}^{39}$  Bose-Einstein condensates. *Phys. Rev. A*, 2010, 82, 063611.
- [64] F. LONDON. The  $\lambda$ -Phenomenon of Liquid Helium and the Bose-Einstein Degeneracy. *Nature*, 1938, 141, 643.
- [65] F. LONDON. On the Bose-Einstein Condensation. *Phys. Rev.*, 1938, 54, 947.
- [66] C.E. Hecht. The Possible Superfluid Behaviour of Hydrogen Atom Gases and Liquids. *Physica*, 1959, 25, 1159.
- [67] M. Hugbart, J. A. Retter, F. Gerbier, A. F. Varón, S. Richard, J. H. Thywissen, D. Clément, P. Bouyer and A. Aspect. Coherence length of an elongated condensate. *Eur. Phys. J. D*, 2005, 35, 155.
- [68] H. J. Metcalf and P. V. der Straten. *Laser Cooling and Trapping*. Springer, Illustrated Edition ed. 1999.
- [69] C.J. Foot. *Atomic Physics*. Oxford, Oxford Master Series In Physics. 2004.
- [70] David J. McCabe. The formation of ultracold rubidium molecules using ultrafast photoassociation. PhD Thesis, St Cross College. Oxford. 2009: Clarendon Laboratory, University of Oxford, (UK).
- [71] V. I. Balykin, V. G. Minogin and V. S. Letokhov. The Electromagnetic trapping of cold atoms. *Reports on Progress in Physics*, 2000, 63 1429.

Excitation spectrum and coherent phenomena in  $^{87}\text{Rb}$  Bose-Einstein condensates

[72] B. M. Garraway and V. G. Minogin . Theory of an optical dipole trap for cold atoms. *Phys. Rev. A*, 2000, 62, 043406.

## Chapter 2: Experimental setup

In this chapter I will discuss briefly the processes and systems employed to arrive at the Bose-Einstein condensate. Although there are many similar (but not the same) systems used all around the world in different groups (for example see Ref.<sup>[1]</sup>), but here I will keep the discussion very specific to the systems and sequences used in those system that are used in our lab. This chapter will hopefully serve as a starting point for future non-Chines students intending to join our lab as a Master/PhD student.

### 2.1 Saturation Absorption Spectroscopy

The starting point of the cooling of the atomic gas is the atomic magneto-optical trap (MOT). The MOT uses a magnetic field gradient and stable laser frequencies to trap and cool the gas initially. To accurately address the narrow energy levels of atoms, the tunable diode lasers (TOPTICA DL 100 and DL 100 Pro) are frequency stabilized using saturation absorption spectroscopy (SAS) technique. The basic physics behind the SAS is discussed by many books<sup>[2]</sup> and the various optical components to realize this technique is shown in Fig. 2.1. In this technique, the laser frequency is stabilized using a reference atomic transition. The vapor cell containing  $^{87}\text{Rb}$  (and  $^{85}\text{Rb}$ ) atoms (in Fig. 2.1) provides this reference. A weak probe laser beam and a strong pump laser beam are passed counter-propagating to each other in the cell and only the atoms in resonance with both of the laser beams will contribute to the SAS locking signal. The strong pump beam will deplete these atoms from the ground state and thus this will show up as peaks in the weak probe laser beam intensity which is monitored by the detector. This detector signal is then fed to the locking electronics which locks the laser frequency to a given transition. Since the atoms have a broad Doppler absorption profile, the pump and probe beams are counter-propagated so that only the non-broadened linewidth of the same set of atoms is addressed by each beam. In SAS setups where the acousto-optic modulators (AOMs) are not used, the peaks in the probe beam transmission intensity only occur for atoms at rest or moving perpendicularly to both of the beams. However in atomic physics experiments, the offset frequency locking of the laser is most of the times needed, and this is done using AOM in the path of the strong pump beam. This kind of SAS is called the modulation transfer

## Excitation spectrum and coherent phenomena in $^{87}\text{Rb}$ Bose-Einstein condensates

spectroscopy as the modulation needed for the operation of the lock-in detection (to generate the error signal for the PID) is done via the AOM and not via the laser directly. The AOM shifts the frequency of the strong pump beam while the weak probe laser beam frequency is

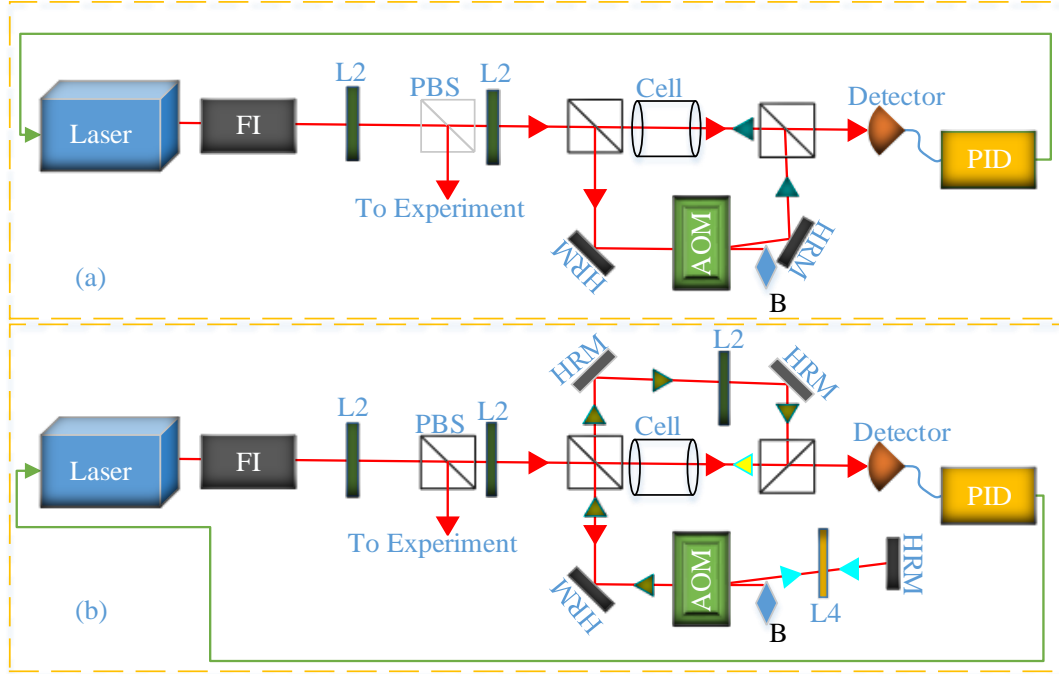


Figure 2.1. The SAS setup where (a) shows the single pass configuration and (b) shows the double pass configuration. FI: Faraday Isolator, L2: Half-wave plate, L4: Quarter-wave plate, PBS: Polarizing beam splitter, HRM: High reflection mirror, AOM: Acousto-optic modulator, PID: Proportional-Integral-Differential circuit, B: Beam blocker, Cell: Vapor cell containing the  $^{87}\text{Rb}$  atoms. The offset frequency locking is always equal to half of the frequency shift introduced by the AOM in the SAS setup.

not shifted. Now, the weak probe and strong pump laser beams will be simultaneously in resonance with those atoms having a Doppler shifted energy level equal to half the frequency shift introduced by the AOM. These atoms will be moving away or towards one beam and in the opposite direction to the other beam depending on the mode of the AOM used (+1 or -1 diffraction mode of the AOM being used). In the same manner, the frequency of the laser is offset locked depending on the sign of the mode of the AOM and the frequency of the AOM. The Doppler width of the atomic sample used in the SAS and the frequency tuning range of the AOM limits the amount of offset locking frequency to which the laser can be locked. Fig. 2.1(a) shows the single pass SAS and 2.1(b) shows the double pass SAS



scheme depending on how many times the pumping beam is shifted by the AOM. The detector takes the signal to a lock-in amplifier (acting as a phase-sensitive detector) which then (with the help of a proportional–integral–derivative (PID) circuit) locks the frequency of the laser by modulating its current and its cavity length (via a piezo-actuator mounted grating).

The AOM is driven by a radio-frequency (RF) circuit (homemade using the Mini Circuits POS and PAS ICs) and is further modulated by the Lock-in amplifier (using an adder circuit given in Appendix A) for phase sensitive detection of the weak probe signal. The back reflections from the multiple optical components are stopped by the Faraday Isolator thus keeping the laser cavity stable against any competition of the modes from the reflected light.

### 2.2 Magneto-Optical Trap (MOT)

The fact that photons carry a linear momentum of  $p = \hbar k$ , (where  $k$  is the wave-vector of the traveling laser field) incites the thought of momentum conservation in light-matter interaction. In other words, the photon does transfer this momentum to the atom during each absorption-emission cycle and the atomic momentum changes by the amount of absorption-emission cycles and also on the direction of the absorbed and emitted photon. Since the direction of the absorption photon is in our control (as we can control the direction of the incident laser photons) while the emission process is totally random, we can transfer momentum to the atom during the absorption process in a single specific direction<sup>[3]</sup>. This way, the kinetic energy of the atom can be reduced in that particular direction by a large number of absorption cycles as the random emission process would result in zero net momentum transfer to the atom. But to achieve these large number of absorption-emission cycles on the same atom, the atom must be held in the path of the incident laser beam. This is done in an experimental setup called the three dimensional magneto-optical trap (3D MOT) whose schematic is shown in Fig. 2.2. The 3D MOT is a hybrid trap as it consists of three pairs of orthogonal beams and a magnetic field distribution such that the field at the center region, where the three pairs of beams intersect, is zero. As the frequency of the

trapping laser is fixed at a certain detuning, after a certain absorption-emission cycles, the atomic motion will be reduced so much that the atoms will be now out of resonance of the applied laser field due to the Doppler shift. Thus, the atoms will no longer be cooled by the laser beams. This is called the Doppler limit<sup>[4]</sup> of the atomic temperature  $T_{dop} = \frac{\hbar\Gamma}{2k_B}$  ( $^{87}\text{Rb}$  has a Doppler limited temperature of 146  $\mu\text{K}$ ) where  $\Gamma$  is the natural linewidth of the D2 line of the  $^{87}\text{Rb}$  atom and  $k_B$  is the Boltzmann constant. The magnetic field of the 3D MOT can overcome this problem (up to some extent) by tuning the energy levels (by Zeeman shifting them) and thus the atoms can undergo more absorption-emission cycles. The sub-Doppler cooling mechanisms also help cool the atoms below the Doppler limit<sup>[5]</sup>. The magnetic field also provides the necessary restoring force together with the radiation force from the six laser beams to hold the atoms in the center of the MOT.

The 3D MOT is realized by applying six red detuned counter-propagating beams along the three orthogonal directions to each other at the center of an ultra-high vacuum (UHV) cell in the presence of a quadrupole magnetic field. The vacuum in the 3D MOT cell is maintained at less than  $10^{-10}$  Pa with the help of an ion pump (150 liters 4UHV ion pump by Agilent Technologies). The coils producing the magnetic field gradient are biased in the anti-Helmholtz configuration and thus the magnetic field at the center of the two coils is zero while increases linearly when we go away from the center<sup>[6]</sup>. Each of the coil is made by  $8 \times 22$  turns of a 1 mm thin copper wire (wound in circles of 7.5 cm radius). The cell center is coincided with that of the zero of the magnetic field and the intersection point of the six MOT beams as shown in Fig. 2.2. The magnetic field serves to tune the atomic absorption levels using the Zeeman shift in such a way that the atoms at the center of the cell receive lesser kicks compared to the ones away from the center for a certain detuning of the laser. The polarization of the six beams is made circular using quarter wave-plates. All of the horizontal beams have  $\sigma^+$  polarization when seen moving towards the cell and the vertical beams are  $\sigma^-$ —polarized when seen moving towards the cell. However, for an atom moving along one beam (for example along one of the  $\sigma^+$ -polarized beam), it will see the opposite direction beam as oppositely polarized ( $\sigma^-$ —polarized). This is why the atom will be only in resonance with the beam moving against its direction of motion and the other

## Chapter 2: Experimental setup

beam (along its motion direction) will be red shifted due to the Doppler and the Zeeman shift. Therefore, the atoms feel a restoring force towards the center of the cell and are trapped there for as long as the magnetic and optical fields are ON<sup>[7]</sup>. This configuration of  $\sigma^+$ / $\sigma^-$  polarization in the horizontal/vertical beams is due to the directions of the magnetic field lines with respect to the two (vertical/horizontal) directions<sup>[8]</sup>. The position dependent Zeeman shifted detuning of the laser beams from the atomic transition can be written as  $\delta^{\pm}_{MOT} = \delta \mp k \cdot v \pm \alpha x$ , where the first term is the laser detuning from the absolute (non-shifted) atomic transition, the second term is the Doppler broadening due to motion of the atom and the third term is the position dependent Zeeman shift.

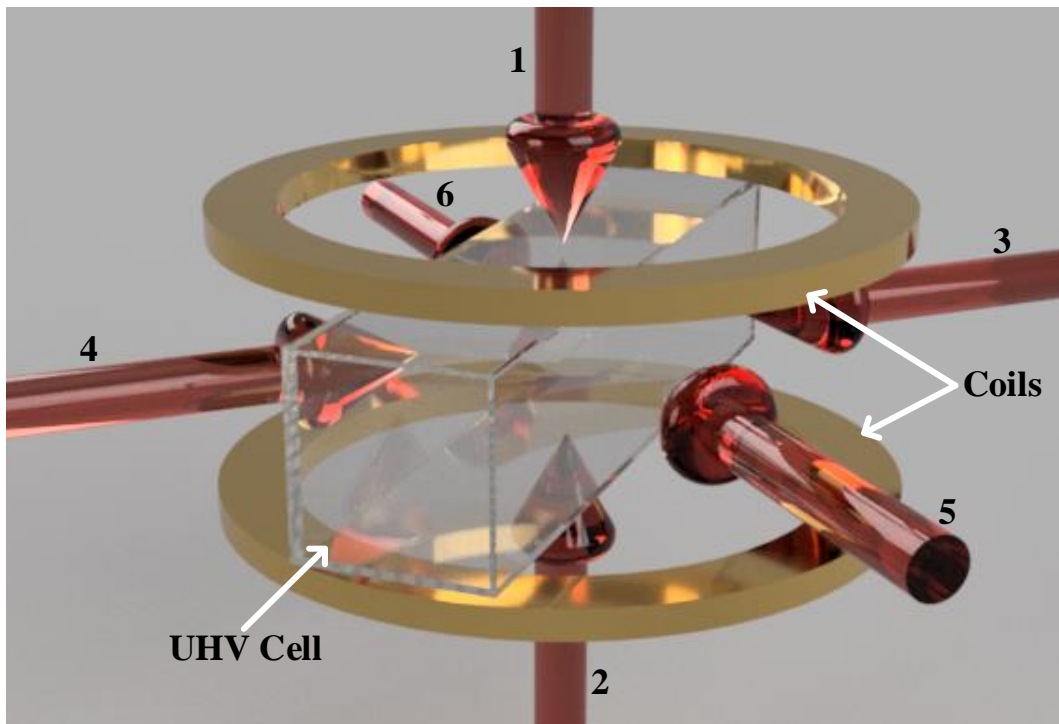


Figure 2.2. The schematic of a 3D MOT configuration. Six (cooling or trapping+repumping) laser beams along the three orthogonal directions oppose the motion of atoms inside the ultra-high vacuum (UHV) cell placed at the center of the two current carrying coils (shown as Coil up and Coil down in Fig. 2.3). The hole in the cell connecting the 3D MOT side to the 2D MOT side by the differential pressure tube is not shown.

Putting this value of the detuning in Eq. (1.24), the scattering force on the atom in the MOT becomes,

$$\begin{aligned}
 F_{scat}(x, v) &= F_+ + F_- \\
 &= \frac{\hbar\Gamma k}{2} \\
 &\cdot I/I_s \left( \frac{1}{1 + (I/I_s) + (2\delta_{MOT}^+/\Gamma)^2} \right. \\
 &\quad \left. - \frac{1}{1 + (I/I_s) + (2\delta_{MOT}^-/\Gamma)^2} \right)
 \end{aligned} \tag{2.1}$$

which, on simplification becomes

$$F_{scat}(x, v) = \frac{4\hbar k (I/I_s) (2\delta/\Gamma)}{\left[1 + (I/I_s) + (2\delta/\Gamma)^2\right]^2} (kv + \alpha x) \equiv -\beta v - \kappa x \tag{2.2}$$

with  $\kappa = \alpha\beta/k$ . Eq. (2.2) thus shows that the force on the atoms is dependent on the velocity and position of the atoms and also depends on the intensity of the six beams and it acts to damp the atomic motion. This force is strong enough to capture the atoms coming from the 2D MOT (and from the background vapor) in the atomic beam but as long as their velocity is smaller than the capture velocity of the MOT, which is calculated from this force. The loading rate of the MOT is highly dependent on the power (and detuning) of the six laser beams and also on the density of the background vapor pressure (or the atom pumping rate from the 2D MOT to the 3D MOT)<sup>[9]</sup>.

The magnetic field gradient in the MOT stage in our setup is 4 G/cm which is generated by running 0.8 A of current through the MOT coils (at 2.8 V). The coils are water cooled by bathing them in flowing water at 15 °C. A Delta Elektronika (SM70-45D) power supply is used to drive the two coils with the help of a computer controlled switch. The sketch of this switching circuit for the current flowing in the MOT/Feshbach coils is shown in Fig. 2.3. This kind of switch helps utilize the same pair of coils for the dual purpose of MOT/Magnetic quadrupole trap and for Feshbach magnetic field and eliminates the need for using a pair of separate coils for the generation of magnetic field for the Feshbach resonances (this setup is also used for <sup>39</sup>K BEC production where we need the Feshbach field, which I will not discuss in this thesis). Each switch S1-4 in the circuit of Fig. 2.3 is a

## Chapter 2: Experimental setup

set of three parallel IGBT modules (APT50GR120JD30 by Microsemi) which can withstand higher currents during the Magnetic quadrupole trapping and Feshbach stages of experiments. The biasing circuit for controlling these IGBTs is listed in Appendix A. The power supply is programmed via an RS232 connection from the Control PC analog output. The Control PC analog output channel is isolated from the high voltage Delta Elektronika (SM70-45D) power supply by passing the programming voltage via an isolator circuit first and then feeding it to the power supply programming port through the RS232 connector. The circuit for the Isolator is also listed in the Appendix A.

The laser light for the six cooling MOT beams is derived from a Toptica DL 100 laser operating at 780 nm. The setup for the optical beams and the frequency shifting scheme for the BEC preparation process is given in Appendix A. The cooling laser is locked from the  $F=2$  to  $F \simeq 3$  hyperfine level of the D2 line as shown in Fig. 2.4. This energy scheme for the cooling laser is suitable for cooling the atoms as this is a cyclic transition and the atom will always de-excite to the  $F=2$  level due to the restriction of selection rules ( $\Delta F = 0, \pm 1$ ), stopping it to decay to the  $F=1$  level. However, the atoms in the MOT will still decay to the  $F=1$  hyperfine level due to hyperfine changing collisions with other atoms (inelastic collisions) and thus another laser called the repump laser (we use MOG laboratories model ECD-003) must be used (although at much lower power) to excite the atoms back to the  $F \simeq 2$  level. From here, the selection rules allow the atoms to decay back to the  $F=1, 2$  states and thus the cyclic cooling transition process is not depleted for atoms in the  $F \simeq 2$  level. The repump laser is also frequency stabilized by the SAS method. The cooling laser frequency in the 3D MOT beams is detuned by -16.8 MHz from the  $F=2$  to  $F \simeq 3$  transition with the help of the AOMs shown in the optical setup of Fig. A.6 in Appendix A. The repump laser frequency at the 3D MOT stage is detuned by -0.45 MHz from the  $F=1$  to  $F \simeq 2$  transition, which is almost at resonance.

The frequencies of both the cooling and the repump lasers are not constant during different stages of the experiment and thus these laser beams are actively frequency shifted using AOMs (called the shift AOMs). The AOM driving circuits (the frequency component of the POS-PAS circuits) are controlled from the analog channels box of the Control PC without the use of isolator circuit in between as the POS-PAS does not operate at high

## Excitation spectrum and coherent phenomena in $87\text{Rb}$ Bose-Einstein condensates

voltages. Similarly, the amplitudes of these lasers are not constant throughout the experiment and thus in the same way we control the amplitude of the AOM RF input from the amplitude component of the AOM driving circuits (POS-PAS circuits) via the analog channel of the Control PC.

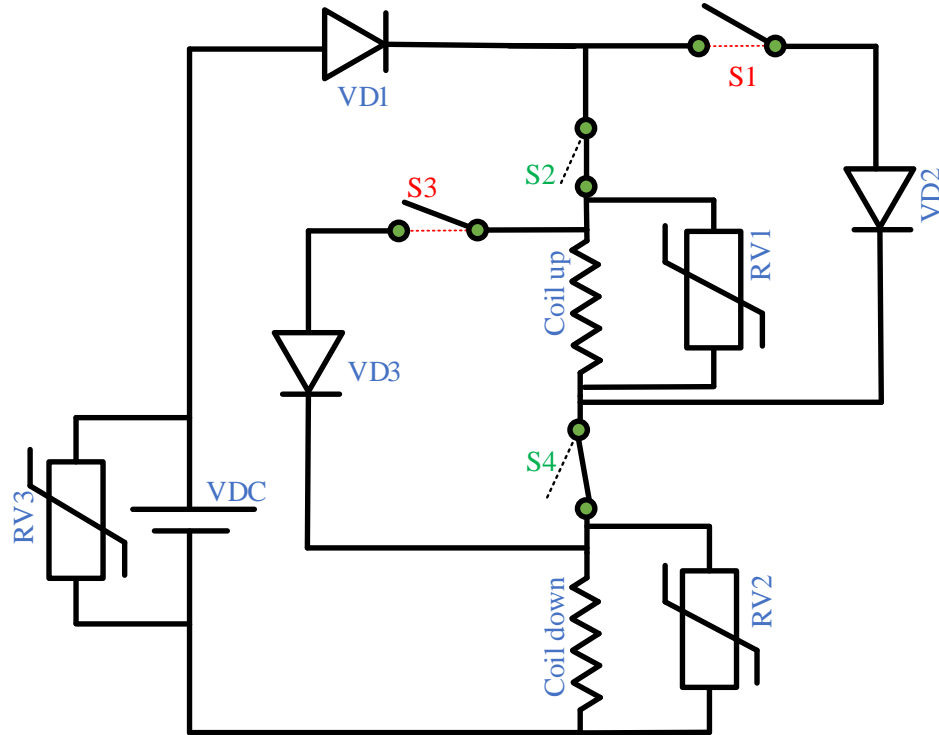


Figure 2.3. The MOT/Feshbach dual switch used to control the current through the MOT/Feshbach coils shown as Coil up and Coil down in this sketch. S1-S4: Each switch S is a set of 3 IGBT modules in parallel controlled by a single ON/OFF control signal, VDC: The Delta Elektronika power supply, VD1-3: High power threaded Phase Control Silicone Thyristor SCR Rectifiers (ZP-200A, 1600 V by Beijing Chunshu Rectifier CO., LTD) (all of are of the same value), RV1-3: V251DB40 Varistors (by Littelfuse, Inc.), (all the Varistors are of the same value). When switches S1 and S3 are ON and S2 and S4 are OFF, the coils produces MOT/Magnetic quadrupole field and when the switches S2 and S4 are ON and S1 and S3 are OFF then the resulting magnetic field between the coils is uniform and is used for Feshbach resonance experiments. The circuit switching the IGBT switches is given in Appendix A.

The POS-PAS circuit and the analog channels box are listed in the appendix A. The AOMs also work as fast switches but to fully block all the laser light, we also use mechanical shutters in combination with the AOMs. The shutters are controlled from the digital channel box of the Control PC and work at 24 V DC and thus an amplifier circuit is needed to lift

## Chapter 2: Experimental setup

up the digital channel output of 3.2 V DC to 24 V DC. The circuits of the digital channel box of the Control PC and the amplifier circuit for the 24 V DC are listed in appendix A.

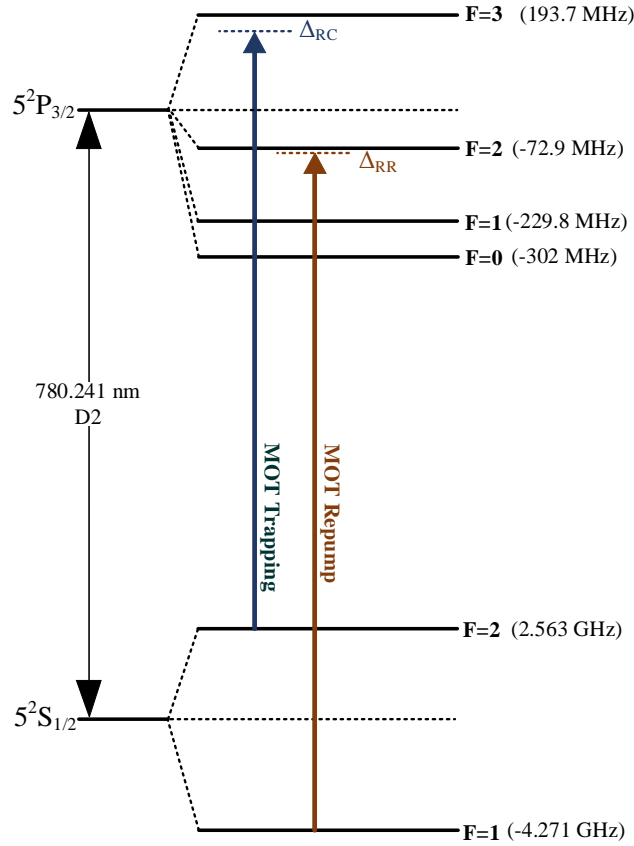


Figure 2.4. The D2 line energy level diagram of  $^{87}\text{Rb}$  atom showing the MOT cooling (trapping) and MOT repump laser locking frequencies/locking schemes.

As discussed above, the 3D MOT is loaded from a 2D MOT which is a beam of atoms confined by orthogonal beams in two directions (passing several time through the cell) and allowed in one direction to move towards the 3D MOT through the differential pressure tube as shown in Fig. 2.5. The  $^{87}\text{Rb}$  atoms enter the 2D MOT cell from the  $^{87}\text{Rb}$  oven heated continuously at  $45^\circ\text{C}$  via flowing current through a heat tape wrapped around the oven (the oven is a metallic cylinder housing the  $^{87}\text{Rb}$  ampule). Two push beams along the atomic beam help the atoms to enter the 3D MOT from the 2D MOT. The push beams are respectively, a red detuned beam ( $-10.2\text{MHz}$  at  $4\text{ mW}$ ) and a blue detuned beam ( $+15\text{ MHz}$  at  $1\text{ mW}$ ) from the  $F=2$  to  $F \simeq 3$  transition.

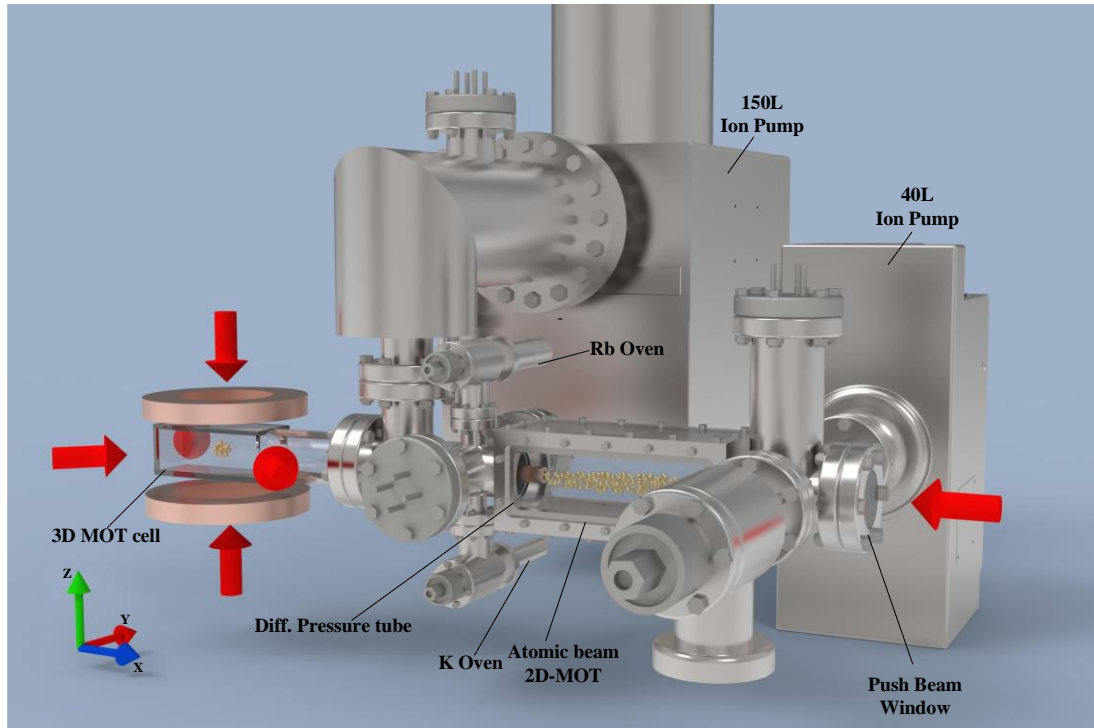


Figure 2.5. The experimental setup for the realization of BEC showing various components. The six MOT beams are shown in the left corner of the Fig. together with the MOT/Feshbach coils and the UHV cell. The 150 L ion pump empties into the 3D MOT side of the vacuum chamber and the 40 L ion pump empties into the 2D MOT side of the chamber while the two sides are connected by the differential pressure tube. The atomic beam in the 2D MOT cell is shown without the MOT beams. The  $^{87}\text{Rb}$  source is shown. Since our system is also capable of producing  $^{39}\text{K}$  BEC, the  $^{39}\text{K}$  source is also visible. The push beam is shown on the right side of the setup entering the 2D MOT from the window.

The power of the cooling laser is not enough for the two MOTs, so, around 22 mW of the laser output is sent into a Toptica BOOSTA semiconductor laser amplifier which amplifies it to around 500 mW. The repump laser power is enough for both of the MOTs and around 26 mW of the repump laser power is divided into two parts and each part is sent into the two MOTs. The 500 mW cooling laser power is also divided into two parts and each part is sent to the respective MOTs. The 3D MOT part is sent via 6 optical fibers together with the repump power of the 3D MOT. The power (cooling and repump) in the four horizontal 3D MOT beams is two times that of the two vertical beams.



## Chapter 2: Experimental setup

The two MOTs are kept at low pressure by the Agilent Starcell ion pumps (150 L/s for the 3D side and 40 L/s for the 2D side, each controlled by the Agilent 4 UHV ion pump controller) as shown in Fig. 2.5. For further accurate observation of the vacuum, two Agilent XGS-600 Vacuum Gauge Controllers actively monitor the degree of vacuum with the help of vacuum gauges (one for 3D MOT and one for 2D MOT). Three pairs of rectangular shaped coils (called the earth coils) are also used in Helmholtz configuration around the 3D MOT for the cancellation of any stray magnetic fields (earth field or the magnetic fields from other components in the lab). These coils also serve for providing the necessary quantization field during optical pumping and also during the state transfer using microwave (from  $F=2$  to  $F=1$ ). The 2D MOT coils are powered by the non-programmable GW Instek GPS-x303 Series power supplies (each pair of coil powered by one power supply, switching is done by IGBTs) while the earth coils are powered by the RS232 programmable Delta Elektronika ES 030-10 power supplies and its switching is done with the help of the same IGBT switching modules mentioned above. All the coils, except the earth field coils, are water cooled so that their performance stays the same throughout the whole experimental procedure.

### 2.3 Compressed MOT and optical molasses

The MOT beams are arranged in such a fashion that it can reduce the temperature of the atoms to less than the Doppler limit by the sub-Doppler cooling mechanism (Sisyphus cooling) but the high power requirements of the MOT limits this temperature due to light recoil and light assisted inelastic collisions. However, we still can achieve sub-Doppler temperatures in the MOT<sup>[10]</sup>. Using low power beams would reduce the initial trapped atoms number and therefore, the optical molasses cooling using low laser power and largely detuned frequency is performed after the initial trapping in the MOT<sup>[11-13]</sup>. The details about the physics behind the sub-Doppler cooling can be found in Ref.<sup>[14-17]</sup> which lists the availability of the Zeeman levels and the polarization gradient potentials experienced by these Zeeman levels during the optical molasses cooling procedure. The dipole forces experienced by these Zeeman levels act on the atoms and the atoms feel retarding potentials while moving through these polarization gradient molasses made by the counter-

propagating circularly polarized MOT beams. Excitation at the maxima of the potentials and de-excitation at the minima of potentials results in the Sisyphus cooling (sub-Doppler cooling) of the atoms.

The MOT only collects and pre-cool the atoms but the various procedures following the MOT aims only at cooling the atoms. First the atoms after the MOT stage are compressed by increasing the magnetic field gradient using the MOT coils to 22 G/cm. This stage is called the compressed MOT (CMOT) stage and it lasts for 150 ms. During this stage, the repump power is kept the same but the cooling laser power is reduced to just 10% of its value during the MOT stage. The repump laser detuning is changed to -20.5 MHz from its transition shown in Fig. 2.4, and the cooling laser detuning at this level is -22.5 MHz.

After this, the optical molasses step follows in which the magnetic field of the quadrupole coils is turned OFF abruptly and the cooling beam and repump beam detunings are respectively changed to -38 MHz and -32 MHz while their intensities are increased to the 3D MOT level. The molasses step lasts for 6.7 ms and the largely detuned laser beams reduces the light assisted losses while the increased intensity provides the necessary potential depth for the Sisyphus cooling excitation de-excitation mechanisms. Theoretically, this molasses step should reduce the temperature of the atoms to the single photon recoil energy limit  $k_B T_{rec} = \frac{(\hbar k)^2}{2m}$ , where  $T_{rec}$  is the recoil temperature of the atom.

However, practically the temperature achieved after the molasses is several tens of the recoil temperature due to multiple recoil energy transfers between the atoms and the cooling laser photons due to the higher power requirements of the Sisyphus cooling technique. The theoretical value of  $T_{rec}$  for  $^{87}\text{Rb}$  is 180 nK which is very near to the critical temperature. Therefore, the optical molasses just falls short of achieving the BEC temperatures and we use the evaporation in the magnetic trap to further cool the atoms in the absence of the cooling laser. The molasses can cool but can't trap the atoms and thus its duration is kept short to avoid any loss of atoms (especially due to gravity as the kinetic energy of the atoms after molasses is so low that it would take them around 30 s to travel 1 cm of distance<sup>[18]</sup>).

## 2.4 Optical pumping and evaporation in optically plugged magnetic trap

The magnetic quadrupole trap evaporation of the atoms takes advantage of the re-thermalization of the atoms with each other and then letting escape of the hottest ones so that the remaining atoms gets cooled. Previously, the hottest atoms were forcefully evaporated by reducing the magnetic trap depth<sup>[19-21]</sup> but we (just like other groups around the world) use the RF evaporation technique by sweeping the frequency of an RF field, to pump only the hottest atoms to the un-trappable states while keeping the magnetic trap depth the same, thus they escape out of the trap taking energy from the sample and resulting in cooling of the atomic sample<sup>[22]</sup>. The magnetic quadrupole trapping field is provided by the same coils used for the MOT field by increasing the current flowing in it. But before that, all the atoms must be transferred to the low field seeking state  $|F = 2, m_F = 2\rangle$ , a process called optical pumping. This is because the low field seeking states will get collected in the center of the magnetic quadrupole trap as the magnetic field strength in the center is minimum. It is impossible to create a magnetic field maximum in free space, so trapping the high field seeking atomic states is not possible<sup>[18]</sup>. The magnetic force experienced by an atom is the gradient of the magnetic potential energy the atoms have  $U = -\mu \cdot B$  in the magnetic field  $B$ , where  $\mu$  is the magnetic moment of the atom and is given by  $\mu = \mu_B g_F m_F$ , which means it is dependent on the magnetic spin state of the atom<sup>[23]</sup>. The sign of the force depends on the value of the Landé  $g$ -factor  $g_F$  and the spin quantum number  $m_F$ . The atoms in the  $|F = 2, m_F = 2\rangle$  state experience the greatest repulsive force and are repulsed to the center of the trap while atoms in high field seeking states (states for which the sign of  $g_F$  and  $m_F$  is not the same) will be attracted towards the higher field direction (high field seeking) and are thus lost from the magnetic quadrupole trap.

The optical pumping is performed by using a  $\sigma^+$ -polarized cooling laser light (called the pumping light) which excites atoms through the  $\Delta m_F = +1$  transition and resulting in the depletion of atoms from all the other  $m_F$  states as they will get excited to the  $|F = 2, m_F = 2\rangle$  state after several excitation de-excitation cycles. A weak repump light also helps in the optical pumping process to keep the atoms from leaving the cyclic transition. The cooling laser beam is shifted 24 MHz above the cooling transition  $F=2$  to  $F \simeq 3$  transition while the repump light is detuned by 36 MHz from the  $F=1$  to  $F \simeq 2$  transition.

## Excitation spectrum and coherent phenomena in $^{87}\text{Rb}$ Bose-Einstein condensates

Initially, the repump beam is turned ON and 0.5 ms later the cooling is turned ON for 1.1 ms and then the repump beam is turned OFF 0.1 ms after the cooling beam. This completes the optical pumping process and now the atoms are in the stretched state  $|F = 2, m_F = 2\rangle$ . There is a weak (2 Gauss) uniform magnetic field present along the vertical direction (provided by the earth coils) for providing quantization axis for the optical pumping process.

Now, the magnetic quadrupole trap is ramped up to 26.5 G/cm by increasing the current in the coils and it is held at this field strength for 10 ms after which it is again ramped up to 62 G/cm in 200 ms and held stable at this field for 50 ms. Finally, the magnetic trap is compressed to 74 G/cm in 300 ms. After this step, a 20 W blue detuned laser (working at 532 nm as an optical plug to avoid Majorana losses of the atoms<sup>[24, 25]</sup>) is turned ON at full power focused ( $30 \mu\text{m}$   $1/e^2$  radius) at the center of the magnetic quadrupole trap. The green laser works on the principle of repulsive dipole force as the 532 nm wavelength is blue detuned for the  $^{87}\text{Rb}$  atoms in the  $5S$  state. The magnetic trap potential is modified by the addition of this blue detuned laser as now the potential minimum is not equal to zero but is equal to the repulsive dipole potential. This magnetic trap is now called the optically plugged magnetic quadrupole trap and its behavior near the center is similar to that of a harmonic potential while away from the center it is linear. To achieve a stable magnetic field, the Delta Elektronika power supply for the MOT coils is programmed from both its voltage and its current programming pins (via the RS232 connector) as at high magnetic fields the large current in the coils heats the coils, thus increasing the resistance which reduces the current and thus the magnetic field. The constant current operation mode ensures that the voltage of the power supply varies automatically to maintain a stable current and hence a stable magnetic field. A stable field is also necessary for the optimal radio-frequency (RF) evaporation cooling process as the Zeeman shift introduced by the large magnetic field of the magnetic trap requires proper tuning of the RF frequency.

The RF frequency source is the Keysight 33250A function/arbitrary waveform generator which is programmed from the Control computer via a GPIB programming port. The RF frequency ramp is programmed from the Control PC and is sent via this GPIB port to the Keysight 33250A as shown in Fig. 2.6. The RF signal is amplified by the Mini Circuits

## Chapter 2: Experimental setup

amplifier (from 13 dBm input) and is sent to the loop antenna which is of the same size as the internal diameter of MOT/Feshbach coils and sits inside the coils just above the cell. To tune the impedance of the antenna to the desired frequency, a 50 ohm resistor is used for optimal power delivery to the cell. The Mini Circuits switch is also controlled from the digital channel box connected to the Control PC and it turns ON and OFF the RF radiation irradiated on the atoms.

The RF sweep starts from 26 MHz frequency and is swept to 10 MHz in 6.2 s and again to 2.5 MHz in 5 s and is then turned OFF after 1 ms. The hottest atoms in the magnetic trap stays in the higher magnetic field (B-field) region and thus their energy levels are shifted more by the Zeeman splitting. Also, we must first remove the atoms whose temperature is higher than the average temperature otherwise cooling will not occur (if cold atoms are removed first, the average temperature will increase). Therefore, the hottest atoms resonant with 26 MHz frequency are removed first by exciting them to non-trappable states (to  $|F = 2, m_F = -1, -2\rangle$  etc). As the atoms get cooled due to this RF evaporation, the frequency of the RF is lowered in a linear way and thus the least hot atoms gets removed in the end as they lie in the lower magnetic field regions and thus have smaller Zeeman energy shifts. The evaporation process is slower compared to the laser cooling during the MOT and the optical molasses processes as the atoms being cooled need to thermalize with each other and transfer heat/kinetic energy to the atoms being evaporated. The atoms transferred to  $|F = 2, m_F = 0\rangle$  state are not affected by the magnetic field (neither trapped nor repulsed) and the gravitational force of the earth will make them fall down and thus only the atoms in the  $|F = 2, m_F = 2\rangle$  state are cooled and left at the end of the RF evaporation cooling. These atoms in the  $|F = 2, m_F = 0\rangle$  state can stay together with the cold atoms in micro-gravity experiments and have been found to be the reason of the tri-modal distribution achieved at the end of the BEC preparation sequence at the international space station (ISS)<sup>[26]</sup>.

It is worth mentioning that the hotter  $^{87}\text{Rb}$  atoms can also be forcibly evaporated using

## Excitation spectrum and coherent phenomena in $^{87}\text{Rb}$ Bose-Einstein condensates

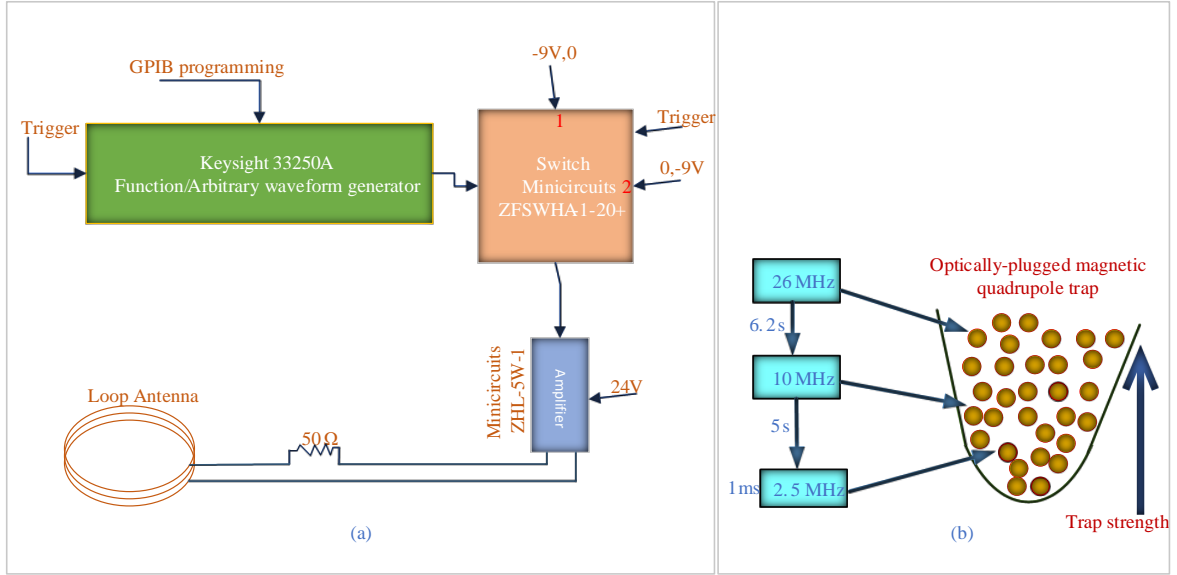


Figure 2.6. The RF evaporation setup and the frequency sweep sequence. (a) The GPIB programming port sends the RF frequency sweep and the trigger initiates the frequency ramp. The Mini Circuits switch turns ON and OFF the RF signal while the amplifier enhances the signal amplitude before sending it to the loop antenna. (b) The quadrupole magnetic trap holding the atoms according to their temperature. The hot atoms occupy the higher B-field region of the trap and thus their energy levels are more Zeeman shifted and thus requires higher frequency while the colder atoms are trapped in the lower field regions and thus have low Zeeman shift and needs lower RF frequency for evaporation.

microwave (MW) radiation resonant with the  $|F = 2\rangle$  to  $|F = 1\rangle$  transition (at around 6.8 GHz) by transferring the atoms to un-trappable sublevels in the  $|F = 1\rangle$  state. When we use our setup for the production of the dual species BECs of  $^{39}\text{K}$  and  $^{87}\text{Rb}$ , we do not want to lose the hard to cool and trap  $^{39}\text{K}$  atoms during the magnetic trap evaporation process and therefore, the  $^{87}\text{Rb}$  atoms are evaporated by MW radiation (which is resonant with the  $^{87}\text{Rb}$  only) and thus the  $^{39}\text{K}$  atoms are cooled sympathetically. In this thesis however, we will keep our focus on the  $^{87}\text{Rb}$  BEC only.

During the whole RF evaporation process, the magnetic gradient of the optically plugged quadrupole trap is held constant at 74 G/cm. At the end of the RF evaporative cooling stage, we have a cold sample of  $4.7 \times 10^7$   $^{87}\text{Rb}$  atoms at 45  $\mu\text{K}$  temperature in the  $|F = 2, m_F = 2\rangle$  state. The atoms can be cooled further in the magnetic quadrupole trap but it requires lowering the trap strength which will lead to extensive loss from the trap due to

## Chapter 2: Experimental setup

gravitational pull on the atoms and also due to the increased Majorana losses. The use of Ioffe-Pritchard quadrupole trap configuration can circumvent these issues but they also limit the optical access to the prepared BEC sample and also is a slower method compared to the optical dipole trap evaporation.

### 2.5 Evaporation in Dipole trap

The dipole force on atoms in an electromagnetic field calculated in chapter 1 shows that the larger the detuning of the laser, the larger will be the force. This force is utilized to hold cold atoms in what is called an optical dipole trap (ODT)<sup>[27]</sup>. Prior to the use of the dipole trap for the creation of BEC, the magnetic traps of different kinds were used but as stated above, their complex structures limited the optical access to the BEC and also have stability issues. The dipole trap overcome these issues effectively. The atoms already cooled in the magnetic trap are transferred to the ODT made by the intersection of two 1064 nm laser beams, derived from the same laser with an optical output power of 20 W. There is a small fraction of 532 nm light present in our 1064 nm laser which is removed by using a 45° high reflection mirror (M1 in Fig. 2.7) for the 532 nm light while allowing the 1064 nm light to pass on. The two laser beams have a frequency difference of 10 MHz to avoid static fringes at the position of the intersection. The moving fringes due to the beating frequency at 10 MHz are too fast to be noticed by the very cold atomic sample. The frequency difference of 10 MHz is introduced by passing both of the beams through AOMs (which also acts as fast switches and amplitude/power regulators). Although the atoms can be all optically cooled to the BEC stage using different schemes (avoiding the slow magnetic trap RF evaporation step) but the number of atoms cooled to BEC temperatures are limited to several to a few tens of thousands<sup>[28-32]</sup>. So far, large condensates (containing more than a million atoms in the condensed state) have been only realized using the magnetic trap RF/MW evaporation process for cooling, prior to the ODT evaporation.

To realize the BEC in the ODT, the atoms are first transferred/loaded into the ODT from the magnetic trap. The loading of the atoms into the ODT is done by increasing the power of the two beams linearly from 0 to 3 W (in each beam) in 500 ms while simultaneously reducing the strength of the optically plugged magnetic quadrupole trap

## Excitation spectrum and coherent phenomena in $^{87}\text{Rb}$ Bose-Einstein condensates

from 74 to 7 G/cm. During the transfer of atoms from one trap to the other, the background magnetic field value is effectively cancelled with the help of the three pairs of earth coils. The intersection point of the ODT beams is chosen such that maximum number of atoms can be loaded from the magnetic quadrupole trap. After this, the green laser is turned OFF and the magnetic trap depth is once again increased to 36 G/cm during 500 ms of time while holding the same power in the ODT laser beams. Then, the magnetic quadrupole trap depth is linearly (but very quickly) reduced to 0 (in just 10 ms) and the atoms are held tight in the dipole trap only thus completing the ODT loading sequence. The temperature of the atoms does not change during this loading process but the efficiency of transfer from the magnetic quadrupole trap to the ODT is just 17 % and thus around 8.2 million atoms are transferred to the dipole trap. Starting with a sample of large number of atoms is beneficial for further evaporative cooling in the ODT as a large sample does not require fine tuning of the evaporation procedure.

After the transfer, the ODT depth is reduced in linear ramps with the help of feedback of the ODT laser beam power through a feedback circuit and the two AOMs<sup>[33, 34]</sup>. The ODT beam paths and feedback schematic is shown in Fig. 2.7 while the feedback circuit is given in appendix A. The ODT depth is programmed and monitored by the Control PC via the feedback circuit which is actively programmed from the analog output channels box of the Control PC as shown by the Prog. 1 (for AOM1) and Prog. 2 (for AOM2) signals in Fig 2.7. The Prog. 1 and Prog. 2 are actually voltage values forming a variable ramp function in time. The Feedback circuit compares the detected light power at the two detectors FD1 and FD2 (and later amplified by amplifiers) with the two programming signals Prog. 1 and Prog. 2, and then accordingly adjusts the output signals amplitudes that are fed to the AOM1 and AOM2 RF drivers (shown as POS-PAS in Fig. 2.7) respectively. This way the RF driver's output amplitude is changed and thus the AOMs act as power/trap depth controllers. In the magnetic trap evaporation process, the feedback circuit is already present in the Delta Elektronika power supply and therefore we do not need add an extra feedback circuit for the magnetic field regulation (however, a magnetic hall sensor is used to monitor the current variation through the coils as a function of time).



## Chapter 2: Experimental setup

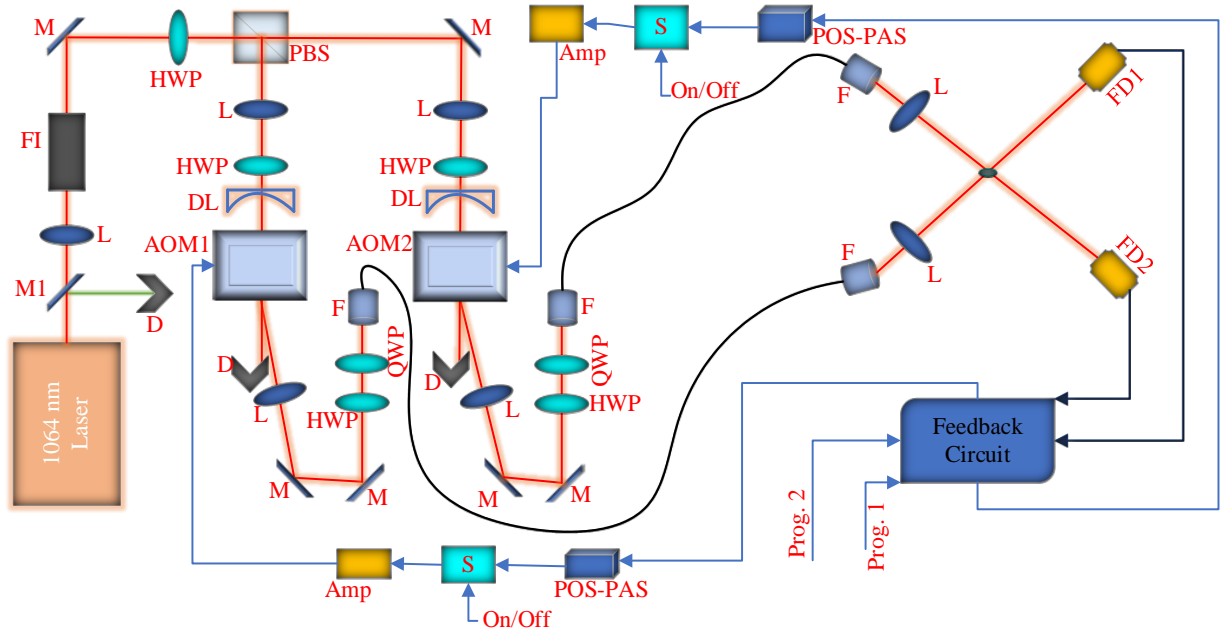


Figure 2.7. The ODT laser beams setup and feedback schematic. M1:  $45^\circ$  high reflection mirror for 532 nm and transmission mirror for 1064 nm used to filter the laser light. L: Focusing lens. FI: Faraday isolator. M:  $45^\circ$  high reflection mirror for 1064 nm laser. PBS: Polarizing beam splitter. HWP: Half wave-plate. DL: Diverging lens. AOM1&2: Acousto-optic modulators. D: Beam dump. QWP: Quarter wave-plate. F: Fiber input/output lens. FD1&2: Feedback detectors for beam 1 and 2. Prog. 1&2: programming ramp signals from the Control computer for the ODT beams. POS-PAS: AOM driver (only the amplitude is being controlled while the frequencies of AOM 1 and 2 are respectively fixed at 80 MHz and 90 MHz in the same -1 order diffraction). S: Mini Circuits switch. ON/OFF: Digital ON/OFF signal from the Control computer. Amp: Mini Circuits RF amplifier.

The ramp down begins by first reducing the power of the two beams to 2.6 W (each) during 30 ms of linear ramp. Then, another ramp of 100 ms brings the power in both beams down to 1.6 W. Then two linear ramps lasting for 200 ms and 50 ms brings down the dipole trapping beams strengths to 0.7 W and 0.35 W respectively. Now the ODT laser power is held at this depth for 200 ms and the evaporation of hot atoms during all these ramps leaves a pure BEC of  $^{87}\text{Rb}$  atoms with more than 500 thousand atoms. At slightly deeper depths of the trap, slightly hotter atoms can also stay inside the trap and a bimodal character can be seen as shown in Fig. 2.8. The atoms prepared in the  $|2,2\rangle$  state can now be exposed to any experimental lasers/fields inside the dipole trap or after the dipole trap is turned OFF.

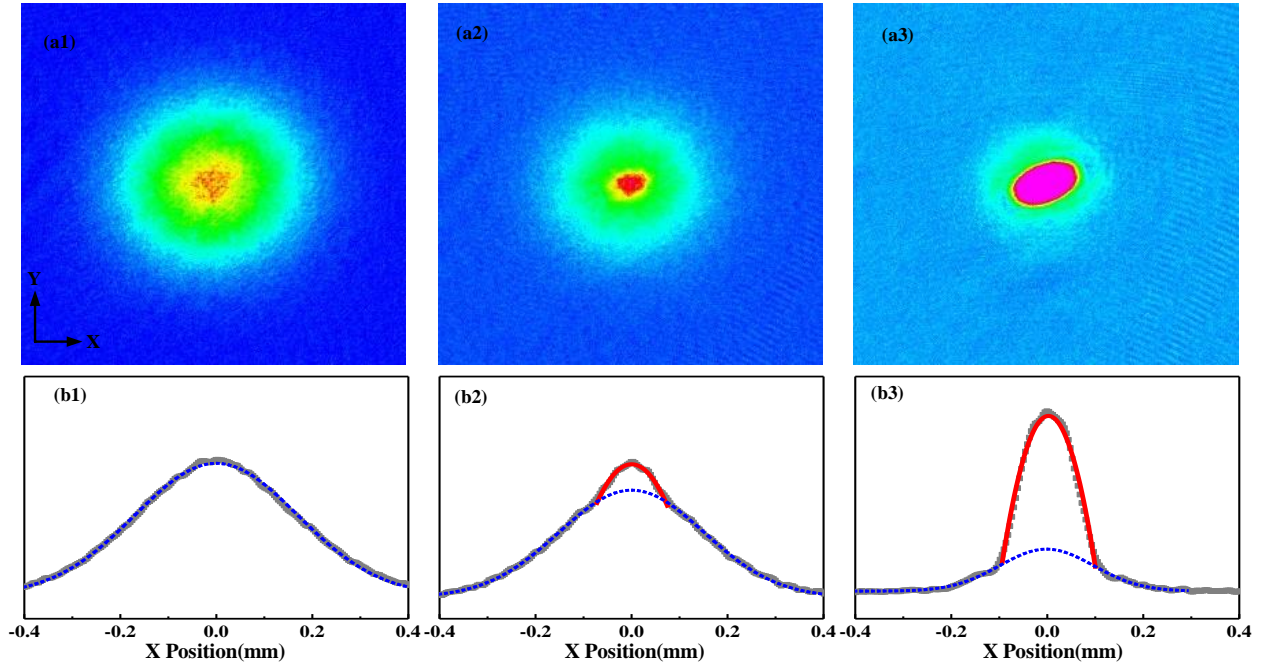


Figure 2.8. The absorption images and the fitting to the optical density of the  $^{87}\text{Rb}$  atoms. (a1) The absorption image of hotter atoms slightly above the critical temperature and the single fit (b1) to the measured optical density. (a2) The absorption image showing the onset of the BEC at the critical temperature and the (b2) bi-modal fit to the measured optical density. (a3) The absorption image of almost pure BEC and (b3) the theoretical bi-modal fit to the measured optical density.

## 2.6 Transfer to $|1, 1\rangle$ state

Sometimes we need the BEC in the lower hyperfine  $|1, 1\rangle$  state. The BEC prepared in the  $|2, 2\rangle$  state can be transferred using the MW radiation in the presence of a quantization field of 2 G. The duration of the MW radiation is 100 ms and is chosen so that no heating of the BEC occurs. The MW radiation frequency is near the hyperfine splitting of 6.834 GHz (slightly shifted due to the Zeeman shift from the quantization field) while the linewidth is kept at around 0.1 MHz. After the MW transfer of the atoms to the  $|1, 1\rangle$  state, any remaining atoms in the  $|2, 2\rangle$  state are removed by a 1 ms flash of the resonant absorption imaging probe light (resonant between the  $|F = 2\rangle$  state and  $|F' = 3\rangle$  state). This states transfer is performed inside the last ODT (most shallow depth) evaporation step (after the BEC has been realized) and after this the atoms are ready for experiment. It is

## Chapter 2: Experimental setup

worth mentioning that the transfer of atoms from the  $|2,2\rangle$  state to the  $|1,1\rangle$  state are electron dipole forbidden but magnetic dipole allowed (which has a low probability and thus needs more power)<sup>[35]</sup>.

The MW frequency is provided by the Keysight E8257D PSG Analog Signal Generator which is programmed from the Control PC using a GPIB port. A +13 dBm signal is amplified by a KUNHE electronic (KU PA 640720-10A) amplifier after passing via an ON/OFF switch (model F9114A by General Microwave). The amplified MW signal is passed through a coaxial isolator (H13-1FFF, Aerotek) for protection of the amplifier from any reflected signal, before being fed into the waveguide antenna (Hengda Microwave HD-70WCAS) which is put just a few cm away from the 3D MOT cell.

### 2.7 Imaging the BEC

Suppose we shine a resonant probe light beam of intensity  $I$  (with a Gaussian profile in the  $xy$ -plane) on an atomic sample of density  $n$  and thickness  $dq$ , the Beer-Lambert law suggests a change  $dI$  in the intensity of light detected by a charge coupled device (CCD) camera (or any other detector) after passing through the atomic sample, to be  $\frac{dI}{dq} = -\sigma nI$ , where  $\sigma$  is the scattering rate. This equation can be solved numerically by detecting the intensity of the probe light with ( $I$ ) and without ( $I_0$ ) the atoms with the CCD camera to get the optical density ( $OD$ ) of the sample as<sup>[1,2]</sup>  $OD = -\ln(I/I_0)$ . This optical density is then later used by an image processing software to calculate the number of atoms in the sample and also calculate the temperature of the atoms from the size of the sample by applying fitting of both thermal and Bose-Einstein statistics to the images<sup>[1,2]</sup>.

Experimentally, after the BEC is ready (in either of the two ground hyperfine states), it is then exposed to any desired experimental field whether optical or magnetic or both. But to know the number of atoms and the temperature of the sample of atoms, we probe the BEC by the absorption imaging technique by taking its pictures with a camera and a probe light. The BEC in the  $|F = 2, m_F = 2\rangle$  state is imaged using a probe light beam of parallel waist ( $\sim 2$  cm dia) that is incident from the vertical direction on the BEC and is resonant between the  $|F = 2\rangle$  state and  $|F' = 3\rangle$  state. The imaging system consists of two imaging

lenses and a CCD, all put under the MOT cell. The BEC is first released from the dipole trap and is left to expand ballistically for 30 ms so that most of its momentum components expand enough to be resolved. Then the probe light is turned ON using an AOM for a short time (several  $\mu\text{s}$ ) and at the same time the CCD camera is triggered to take the absorption picture. Part of the probe light is absorbed by the BEC and thus the BEC cast a shadow on the CCD screen. The atoms in the BEC become heated due to the resonant light absorption and thus evaporates after the absorption. Then the probe light is again flashed and the CCD camera records the intensity of the probe light only. Then, when all the lights are OFF, the CDD again takes a picture of the background and then sends all these pictures to a data acquisition computer (running as a slave computer of the Control PC) for processing. This data acquiring computer is connected with the Control PC by TCP/IP and in addition to saving the acquired images of the BEC, it also saves the experimental parameters inserted in the Control software of the Control PC for these images. The Vision software process these three pictures received from the CCD and the necessary data (time of flight TOF) received from the control PC and retrieve the optical density (OD) profile of the BEC (using Beer-Lambert law), which is then subjected to several polyline fits to extract the number of atoms and the temperature of the atoms along x- and y-directions. The absorption imaging is a destructive process and the BEC is evaporated after the strong absorption during the imaging. However, there are some techniques which uses highly detuned light (dispersive imaging) for probing a single sample of BEC several times without increasing its temperature or destroying its other wavelike properties<sup>[36]</sup>.

To perform absorption imaging on the atom transferred to the  $|F = 1, m_F = 1\rangle$  state, these atoms are first transferred back to the  $|F = 2, m_F = 2\rangle$  state using a repump light flash of 1 ms which optically pumps the atoms from the lower hyperfine state to the upper one and then the same imaging probe is used to take its picture just like in the above mentioned paragraph.

The absorption imaging uses resonance light and thus only samples of small optical densities (OD less than 4) can gives precise results as higher OD samples would need largely detuned probe light and the larger atomic density of such a sample would then result in a

## Chapter 2: Experimental setup

diffraction of the probe thus giving false density distribution profile and false results<sup>[37]</sup>. However, the 30 ms of free expansion allows the density of the BEC sample to reduce so that now the OD is less than the above mentioned limit and thus the results given by the vision software fitting routines are quite precise (prior to the expansion the OD is larger than a few 100s).

The absorption imaging can also be performed for measuring the number of atoms left in the BEC after it is exposed to any other experimental lasers after its preparation, as discussed in the next two chapters. In other experiments, the absorption imaging is not needed and the experimental data can be recorded using other techniques e.g. the scattering from the BEC in a lattice which is also discussed in the coming chapters.

## References

- [1] N. Tammuz. Thermodynamics of ultracold  $^{39}\text{K}$  atomic Bose gases with tuneable interactions, PhD Thesis, Cavendish Laboratory. 2011: University of Cambridge (UK).
- [2] C.J. Foot. Atomic Physics. Oxford, Oxford Master Series In Physics, 2004.
- [3] W. D. Phillips and H. Metcalf. Laser deceleration of an atomic beam, Phys. Rev. Lett., 1982, 48, 596.
- [4] D. J. Wineland, R. E. Drullinger and F. L. Walls. Radiation pressure cooling of bound resonant absorbers, Phys. Rev. Lett., 1978, 40, 1639.
- [5] A. Steane and C. J. Foot. Laser Cooling below the Doppler Limit in a Magneto-Optical Trap, Europhys. Lett., 1990, 14, 231.
- [6] D.J. Griffiths. Introduction to Electrodynamics. India, Pearson Education 4th ed, 2015.
- [7] A. L. Migdall, J. V. Prodan, W. D. Phillips, T. H. Bergeman, and H. J. Metcalf. First observation of magnetically trapped neutral atoms, Phys. Rev. Lett., 1985, 54, 2596.
- [8] D.A. Steck. "Rubidium 87 D Line Data". 21 November 2019; Available from: <http://steck.us/alkalidata>.
- [9] M. Haw, N. Evetts, W. Gunton, J. Van Dongen, J. L. Booth, and K. W. Madison. Magneto-optical trap loading rate dependence on trap depth and vapor density, J. Opt. Soc. Am. B, 2012, 29, 475.
- [10] A. Steane and C. J. Foot. Laser cooling below the Doppler limit in a magneto-optical trap, Europhys. Lett., 1991, 14, 231.
- [11] P. D. Lett, R. N. Watts, C. I. Westbrook, W. D. Phillips, P. L. Gould and H. J. Metcalf. Observation of atoms laser cooled below the Doppler limit, Phys. Rev. Lett., 1988, 61, 169.
- [12] S. Chu, L. Hollberg, J. E. Bjorkholm, A. Cable and A. Ashkin. Three-dimensional viscous confinement and cooling of atoms by resonance radiation pressure, Phys. Rev. Lett., 1985, 55, 48.
- [13] J. Dalibard and C. Cohen-Tannoudji. Laser cooling below the Doppler limit by polarization gradients: simple theoretical models, J. Opt. Soc. Am. B, 1989, 6, 2023.
- [14] J. Dalibard and C. Cohen-Tannoudji. Dressed-atom approach to atomic motion in laser light: the dipole force revisited, J. Opt. Soc. Am. B, 1985, 2, 1707.

## Chapter 2: Experimental setup

- [15] P. J. Ungar, D. S. Weiss, E. Riis, and Steven Chu. Optical molasses and multilevel atoms: Theory, *J. Opt. Soc. Am. B*, 1989, 6, 2058.
- [16] D. S. Weiss, E. Riis, Y. Shevy, P. J. Ungar, and S. Chu. Optical molasses and multilevel atoms: Experiment, *J. Opt. Soc. Am. B*, 1989, 6, 2072.
- [17] A. Bambini and A. Agresti. Radiative cooling force in atoms with multiplet structure, *Phys. Rev. A*, 1997, 56, 3040.
- [18] M. Weidemuller and C. Zimmermann. *Interactions in Ultracold Gases From Atoms to Molecules.*, Weinheim, WILEY-VCH Verlag GmbH & Co. KGaA, 2003.
- [19] N. Masuhara, J. M. Doyle, J.C. Sandberg, D. Kleppner, T.J. Greytak, H.F. Hess, and G.P. Kochanski. Evaporative Cooling of Spin-Polarized Atomic Hydrogen, *Phys. Rev. Lett.*, 1988, 61, 935.
- [20] K.B. Davis, M. O. Mewes, and W. Ketterle. An Analytical Model for Evaporative Cooling of Atoms, *App. Phys. B*, 1995, 60, 155.
- [21] W. Ketterle and N. J. Van Druten. Evaporative Cooling of Trapped Atoms, *Adv. Atom. Mol. Opt. Phys.*, 1996, 37, 181.
- [22] D. Yum, J. Park, W. Lee and W. Jhe. Systematic study of the rf-induced evaporation of  $^{87}\text{Rb}$  atoms in a spherical magnetic quadrupole trap, *Journal of the Korean Physical Society*, 2012, 60, 1.
- [23] W. D. Phillips and H. Metcalf. Electromagnetic Trapping of Neutral Atoms *Metrologia*, 1986, 22, 271.
- [24] E. Majorana. Atomi orientati in campo magnetico variabile, *Il Nuovo Cimento*, 1932, 9, 43.
- [25] H. J. Metcalf and P. Van der Straten. *Laser Cooling and Trapping. Illustrated Edition* ed.: Springer, 1999.
- [26] D. C. Aveline, J. R. Williams, E. R. Elliott, C. Dutenhoffer, J. R. Kellogg, J. M. Kohel, N. E. Lay, K. Oudrhiri, R. F. Shotwell, N. Yu and R. J. Thompson. Observation of Bose–Einstein condensates in an Earth-orbiting research lab, *Nature*, 2020, 582, 193.
- [27] R. Grimm, M. Weidemiiller, and Y. B. Ovchinnikov. Optical Dipole Traps for Neutral Atoms, *Adv. Atom. Mol Opt. Phys.*, 2000, 42, 95.

- [28] J. Hu, A. Urvoy, Z. Vendeiro, V. Crépel, W. Chen, and V. Vuletić. Creation of a Bose-condensed gas of  $^{87}\text{Rb}$  by laser cooling, *Science*, 2017, 358, 1078.
- [29] M. D. Barrett, J. A. Sauer, and M. S. Chapman. All-Optical Formation of an Atomic Bose-Einstein Condensate, *Phys. Rev. Lett.*, 2001, 87, 010404.
- [30] G. Condon, M. Rabault, B. Barrett, L. Chichet, R. Arguel, H. Eneriz-Imaz, D. Naik, A. Bertoldi, B. Battelier, P. Bouyer, and A. Landragin. All-Optical Bose-Einstein Condensates in Microgravity, *Phys. Rev. Lett.*, 2019, 123, 240402.
- [31] A. Urvoy, Z. Vendeiro, J. Ramette, A. Adiyatullin, and V. Vuletić. Direct Laser Cooling to Bose-Einstein Condensation in a Dipole Trap, *Phys. Rev. Lett.*, 2019, 122, 203202.
- [32] G. Salomon, L. Fouché S. Lepoutre, A. Aspect, and T. Bourdel. All-optical cooling of  $^{39}\text{K}$  to Bose-Einstein condensation, *Phys. Rev. A*, 2014, 90, 033405.
- [33] L. Chen, Z. Meng, and P. Wang. Fast production of  $^{87}\text{Rb}$  Bose-Einstein condensates, *Acta Phys. Sin.*, 2017, 66, 083701.
- [34] R. Fazal, J. Li, Z. Chen, Y. Qin, Y. Lin, Z. Zhang, S. Zhang, W. Huang, H. Yan, and S. Zhu. Production of  $^{87}\text{Rb}$  Bose-Einstein Condensate with a Simple Evaporative Cooling Method, *CHIN. PHYS. LETT.*, 2020, 37, 036701.
- [35] V. Natarajan. *Modern Atomic Physics*. Boca Raton, CRC Press, Taylor & Francis Group, 2015.
- [36] M. Gajdacz, P. L. Pedersen, T. Mørch, A. J. Hilliard, J. Arlt and J. F. Sherson. Non-destructive Faraday imaging of dynamically controlled ultracold atoms, *Rev. Sci. Instrum.*, 2013, 84, 083105.
- [37] W. Ketterle, D. Durfee, and D. Stamper-Kurn. Making, probing and understanding Bose-Einstein condensates. in *Proceedings of the International School of Physics Enrico Fermi*, Course CXL. 1999. IOS Press.



## **Chapter 3: Study of an N-Type atomic level system in a Bose-Einstein condensate**

### **3.1 Introduction**

The coherent manipulation of matter using light has attracted enormous interest from the scientific community in the previous several decades, especially after the invention of lasers. The goal of these efforts is to control the absorptive and dispersive properties of the matter using different theoretical and experimental schemes. The general approach of every scheme involves the application of one or more high power lasers to the matter to change its dielectric properties, and then using a weak probe laser to test the material absorption and dispersion properties. Just like the different manipulation methods used in such schemes, the detection or probing methods also vary depending on the frequency and time scale requirements of the property under study. We will be using the absorption imaging technique to recover the information of the system under study. Fig. 3.1 presents some of the mostly used schemes that are employed to modify and probe the material dispersive and absorptive properties on the atomic level. These are just a few schemes and even more complicated schemes have been realized using combinations of such schemes. These systems or schemes not only help in the understanding and testing of the fundamental concepts of quantum mechanics but are also used in many applications. The literature written on the coherent manipulation and control of atomic media is very huge but for self-consistency, some popular applications with references are provided here. The most popular use of such schemes was in the electromagnetically induced transparency (EIT)<sup>[1, 2]</sup> through which the atomic media was made transparent to a weak probe laser at the resonant absorption frequency of that medium by changing its absorptive properties. Soon after, this and several other schemes were employed to change the dispersive properties of the media<sup>[3]</sup> as well and phenomena like superluminal and subluminal light through the media<sup>[4, 5]</sup> were proposed. Other interesting work include coherent non-linear optics using low light intensities<sup>[6-8]</sup>, light storage in an atomic vapor under coherent dressing<sup>[9]</sup>, lasing without inversion<sup>[10, 11]</sup>, electromagnetically induced absorption (EIA)<sup>[12-16]</sup>, coherent population

## Excitation spectrum and coherent phenomena in $^{87}\text{Rb}$ Bose-Einstein condensates

trapping (CPT)<sup>[11]</sup>, amplification without inversion<sup>[17]</sup>, photonic band gaps<sup>[18]</sup> and many more<sup>[19-32]</sup>. Although most of the work of coherent control of atomic media is done in atomic vapors at room temperature or higher temperatures, we use a BEC to observe the coherent control of the absorptive properties of  $^{87}\text{Rb}$  atoms dressed by two strong fields and probed by a weak laser field. Most of the work presented in this chapter is also published in our 2019 paper<sup>[33]</sup> that is part of my PhD work.

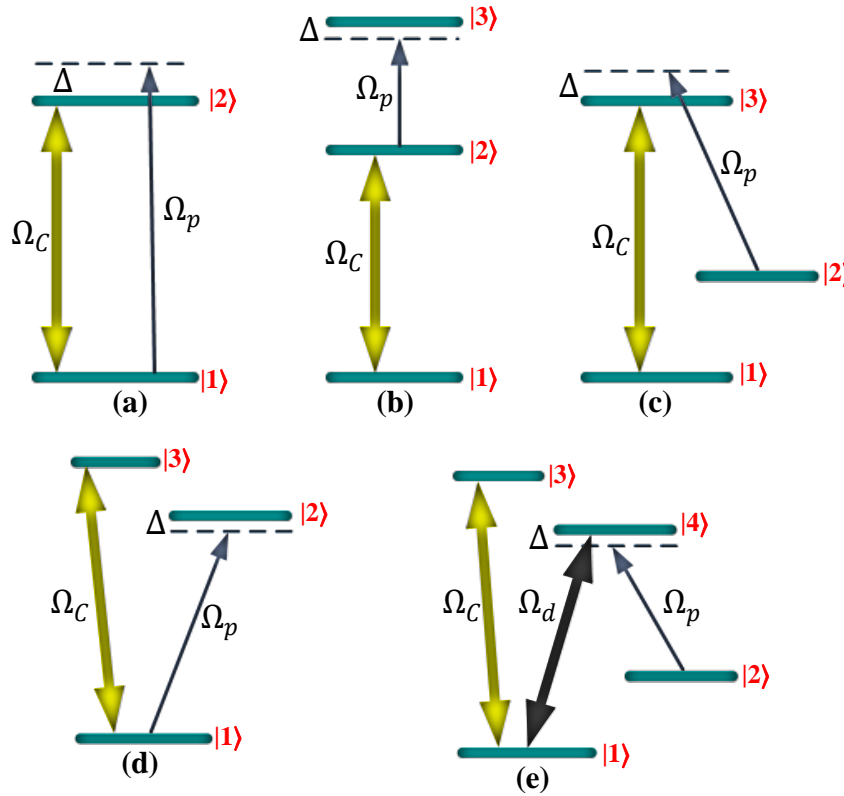


Figure 3.1. Various atomic energy schemes used for the coherent manipulation of the material properties. (a) A two-level system dressed by a powerful coupling laser and probed by a weak probe laser. (b) A three-level cascade-type energy scheme. (c) A three-level lambda-type energy scheme. (d) A three-level V-type energy scheme. (e) A four-level inverted N-type energy scheme. Even higher-level schemes have been realized from the combination of these schemes.  $\Omega_c$ ,  $\Omega_d$  and  $\Omega_p$  are the Rabi frequencies of the coupling, driving and probe lasers respectively.  $\Delta$  is the detuning (red or blue) of the probe laser from the respective level. The coupling and driving lasers are supposed to be resonant with their respective levels.

### 3.2 Realization of an N-Type System in $^{87}\text{Rb}$

We simulate a four level N-type system in the  $^{87}\text{Rb}$  atom in a BEC. The  $^{87}\text{Rb}$  BEC is first prepared in a crossed beams dipole trap as discussed in Chapter 2. All the atoms in the BEC are in the  $|F=2, m_F=2\rangle$  state. The BEC is then subjected to the coupling, driving and probe lasers simultaneously to realize the N-type system, as shown in Fig. 3.2. The probe and coupling lasers are the Toptica DL 100 lasers operating at the D1 line ( $\sim 795$  nm), while the driving and imaging lasers are the Toptica DL Pro lasers operating at the D2 line ( $\sim 780$  nm) of the  $^{87}\text{Rb}$ .

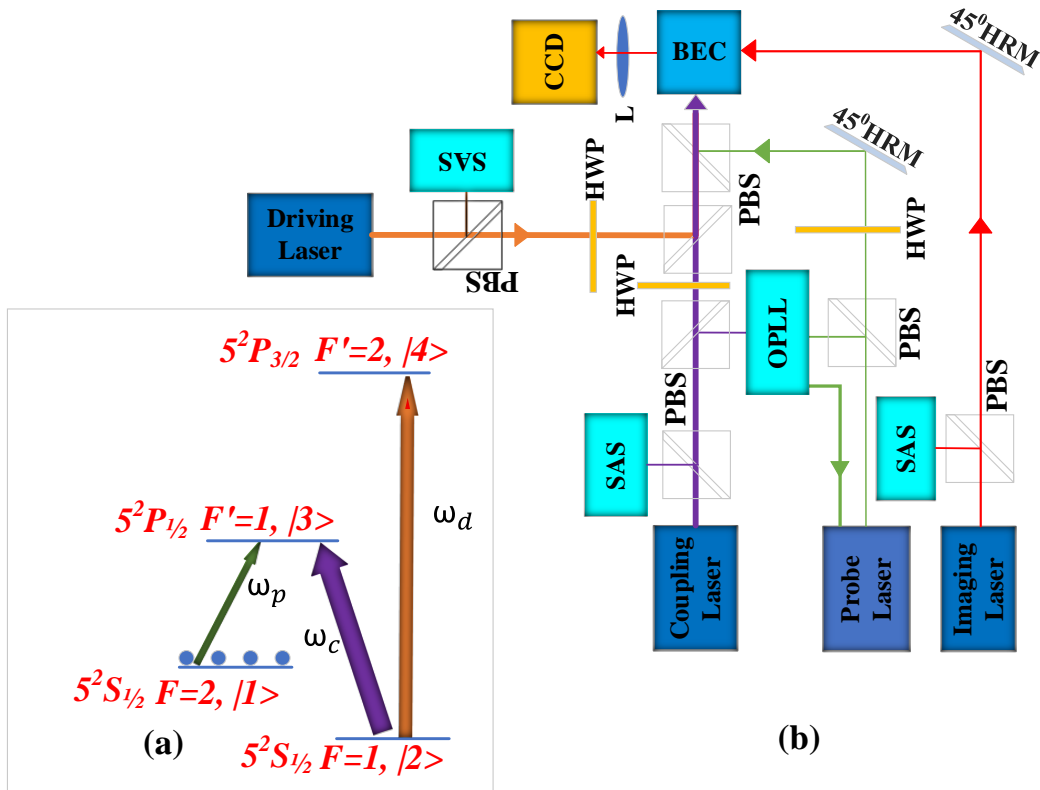


Figure 3.2. The Experimental setup for the N-type system. (a) The four-level energy scheme. The probe laser scans the  $|1\rangle(F=2)$  ( $5^2S_{1/2}$ ) to the  $|3\rangle(F'=1)$  ( $5^2P_{1/2}$ ) at  $\omega_p$ , coupling laser connects the  $|2\rangle(F=1)$  ( $5^2S_{1/2}$ ) to the  $|3\rangle(F'=1)$  ( $5^2P_{1/2}$ ) at  $\omega_c$  and the driving laser couples the  $|2\rangle(F=1)$  ( $5^2S_{1/2}$ ) to the  $|4\rangle(F'=2)$  ( $5^2P_{3/2}$ ) at  $\omega_d$ . The imaging laser is locked between the  $F=2$  ( $5^2S_{1/2}$ ) to the  $F'=3$  ( $5^2P_{3/2}$ ) transition. (b) The laser locking and optical setup. PBS-Polarization beam splitter, SAS-saturation absorption spectroscopy, HRM-high reflectivity mirror, HWP-half wave plate, L-lens, OPLL-optical phase loop lock, CCD-CCD camera.

The coupling laser, driving laser and the imaging laser (used to count atoms after the N-type system is simulated in the BEC), all are independently locked to the transitions shown in Fig. 3.2 using the saturation absorption spectroscopy (SAS) while the probe laser is phase locked to the coupling laser using the optical phase lock loop system (OPLL)<sup>[34, 35]</sup> and its frequency is controlled using a local oscillator.

### 3.3 Hamiltonian of the N-Type System

The extremely low temperature of the BEC makes it an ideal platform for the spectroscopy of the N-type system. Before the experimental results, the theoretical model for the N-type of system is developed in this section. As we can see from Fig. 2.2(b), the state  $|1\rangle$  is connected to state  $|3\rangle$  by the probe laser operating at the tunable frequency  $\omega_p$ . State  $|1\rangle$  has all the atomic population at time  $t=0$ . Similarly, the coupling laser couples states  $|2\rangle$  and  $|3\rangle$  operating at frequency  $\omega_c$  and the driving laser drives the transition between states  $|2\rangle$  and  $|4\rangle$  operating at frequency  $\omega_d$ . All of these lasers interact via the dipole interaction with the atom. The coupling and driving lasers are used at stronger intensity compared to the probe laser. The total Hamiltonian of the system is given by

$$H = H_0 + H_I \quad (3.1)$$

where  $H_0$  is the Hamiltonian of the bare atom in the absence of all the laser fields and  $H_I$  is the Hamiltonian term resulting from the interaction of the atom and the three laser fields of Fig. 3.2(a). This eq. (3.1) is the general form of the Hamiltonian. Many texts have discussed how to derive the explicit form of similar Hamiltonians<sup>[11, 36]</sup>.

We know from the completeness relation for this four-level system that

$$|1\rangle\langle 1| + |2\rangle\langle 2| + |3\rangle\langle 3| + |4\rangle\langle 4| = \sum_{a=1}^4 (|a\rangle\langle a|) = 1 \quad (3.2)$$

Using this Eq. (2.2), the first term in Eq. (2.1) can be written as

$$H_0 = \left( \sum_{a=1}^4 (|a\rangle\langle a|) \right) H_0 \left( \sum_{a=1}^4 (|a\rangle\langle a|) \right) = \sum_{a=1}^4 \hbar\omega_a (|a\rangle\langle a|) \quad (3.3)$$

### Chapter 3: Study of an N-Type atomic level system in a Bose-Einstein condensate

where  $\omega_a$  are the eigenfrequencies of the levels  $|a\rangle$ . Due to the orthogonality condition  $\langle a|H_0|b\rangle = \delta_{ab} = 0$  for  $a \neq b$ , the off-diagonal terms vanish and only the diagonal terms survive in Eq. (3.3).

For the interaction term in Eq. (3.1), we consider the interaction energy of the atom in the laser field as that of a dipole (the atomic dipole approximation) interacting with the electric component of the laser field. Considering first, for the coupling laser, the atom experiences an energy given by

$$H_c = p_{23} \cdot E_c(r, t) \quad (3.4)$$

here  $p_{23}$  is the atomic dipole of the atom interacting with the applied coupling laser field  $E_c(r, t)$ . The laser field is explicitly given by

$$E_c(x, t) = \varepsilon_c \cos(kx - \omega_c t) \quad (3.5)$$

here  $\varepsilon_c$  is the amplitude of the coupling laser field, while we have assumed that the atomic dipole and the applied laser field polarization vectors are aligned and that the coupling laser field is traveling in the x-direction. The atomic dipole  $p_{23}$  has a smaller spatial extent than the total atomic radii (which itself is of the order of atomic Angstrom units  $10^{-10}$  m), which is orders of magnitude smaller than the wavelength of the applied laser field (which is in the optical region of the electromagnetic spectrum). Thus, the  $kx \approx 0$  is a valid approximation and it is called the slowly varying field approximation (SVEA). After the SVEA, the electric component of the laser field given in Eq. (3.5) becomes

$$E_c(x, t) = \varepsilon_c \cos(\omega_c t) \quad (3.6)$$

It should be also noted that since the other laser frequencies (probe and driving) are far enough from this transition between the states  $|3\rangle$  and  $|2\rangle$  that their presence cannot be felt by this induced atomic dipole moment  $p_{23}$ <sup>[36]</sup>, hence their electric field amplitudes are ignored in Eq. (3.4) (mathematically,  $|\omega_{23} - \omega_c| \ll |\omega_{23} - \omega_d|$  and  $|\omega_{23} - \omega_c| \ll |\omega_{23} - \omega_p|$ ). The same rule holds for calculating the other induced atomic dipole moments.

Putting Eq. (3.6) into Eq. (3.4) then gives

$$H_c = p_{23}\varepsilon_c \cos(\omega_c t) \quad (3.7)$$

Now if we use the completeness relation of Eq. (3.2), we can re-write Eq. (3.6) in the atomic basis as

$$H_c = \left( \sum_{a=1}^4 (|a\rangle\langle a|) \right) H_c \left( \sum_{a=1}^4 (|a\rangle\langle a|) \right) \quad (3.8)$$

Expanding the product and putting Eq. (3.7) and (3.2) gives

$$H_c = (|1\rangle\langle 1| + |2\rangle\langle 2| + |3\rangle\langle 3| + |4\rangle\langle 4|) p_{23}\varepsilon_c \cos(\omega_c t) (|1\rangle\langle 1| + |2\rangle\langle 2| + |3\rangle\langle 3| + |4\rangle\langle 4|) \quad (3.9)$$

Since the atomic dipole  $p_{23} = -er_{23}$ , where  $e$  is the electronic charge and  $r_{23}$  is the extent of the dipole between the states  $|3\rangle$  and  $|2\rangle$ . Using this definition of the dipole, Eq. (3.9) takes the form

$$H_c = -e\varepsilon_c \cos(\omega_c t) (|1\rangle\langle 1| + |2\rangle\langle 2| + |3\rangle\langle 3| + |4\rangle\langle 4|) r_{23} (|1\rangle\langle 1| + |2\rangle\langle 2| + |3\rangle\langle 3| + |4\rangle\langle 4|) \quad (3.10)$$

In Eq. (3.10), only the product of the states involved in the transition connected by the coupling laser i.e.  $|3\rangle$  and  $|2\rangle$  will survive and the other terms will be neglected since the coupling laser is far detuned from the other transitions, and also parity conservation must not be violated<sup>[11]</sup>. Therefore, we get

$$H_c = -e\varepsilon_c \cos(\omega_c t) [|2\rangle\langle 2| r_{23} |3\rangle\langle 3| + |3\rangle\langle 3| r_{23} |2\rangle\langle 2|]$$

or

$$H_c = -e\varepsilon_c \cos(\omega_c t) (\langle 2| r_{23} |3\rangle |2\rangle\langle 3| + H.C.) \quad (3.11)$$

or

$$H_c = -e\varepsilon_c \cos(\omega_c t) \langle 2| r_{23} |3\rangle |2\rangle\langle 3| - e\varepsilon_c \cos(\omega_c t) \langle 3| r_{23} |2\rangle |3\rangle\langle 2| \quad (3.12)$$

### Chapter 3: Study of an N-Type atomic level system in a Bose-Einstein condensate

where  $H.C.$  is the Hermitian conjugate of the first term in Eq. (3.12). We can simplify the above equation by defining the Rabi frequency of the coupling laser as

$$\Omega_c = \frac{e\varepsilon_c \langle 2|r_{23}|3\rangle}{\hbar} \quad (3.13)$$

Therefore, Eq. (3.12) takes the form

$$H_c = -\hbar \cos(\omega_c t) (\Omega_c |2\rangle\langle 3| + H.C.) \quad (3.14)$$

It is also useful to write the cosine function in the form of exponentials as

$$\cos(\omega_c t) = \frac{1}{2} (e^{-i\omega_c t} + e^{i\omega_c t}) \quad (3.15)$$

Now we can write Eq. (3.14) as

$$H_c = -\frac{\hbar}{2} (e^{-i\omega_c t} + e^{i\omega_c t}) (\Omega_c |2\rangle\langle 3| + H.C.) \quad (3.16)$$

Similar procedure can be followed for the probe and the driving lasers respectively to get their respective interaction Hamiltonian parts e.g.

$$H_p = -\frac{\hbar}{2} (e^{-i\omega_p t} + e^{i\omega_p t}) (\Omega_p |1\rangle\langle 3| + H.C.) \quad (3.17)$$

$$H_d = -\frac{\hbar}{2} (e^{-i\omega_d t} + e^{i\omega_d t}) (\Omega_d |2\rangle\langle 4| + H.C.) \quad (3.18)$$

Combining Eq. (3.16), (3.17) and (3.18) to get the interaction part of the Hamiltonian as

$$H_I = H_c + H_p + H_d$$

or

$$\begin{aligned}
 H_I = & -\frac{\hbar}{2}(e^{-i\omega_c t} + e^{i\omega_c t})(\Omega_c|2\rangle\langle 3| + H.C.) \\
 & -\frac{\hbar}{2}(e^{-i\omega_p t} + e^{i\omega_p t})(\Omega_p|1\rangle\langle 3| + H.C.) \\
 & -\frac{\hbar}{2}(e^{-i\omega_d t} + e^{i\omega_d t})(\Omega_d|2\rangle\langle 4| + H.C.)
 \end{aligned} \tag{3.19}$$

We can now use a simple trick and neglect all the  $e^{+i\omega t}$  terms, which is called the rotating wave approximation (RWA) in the quantum optics literature. But to justify the usage of the RWA, we first transform our interaction Hamiltonian (Eq. (3.19)) to a rotating frame by the application of the unitary transformation operator as follows

$$H_I' = UH_IU^\dagger \tag{3.20}$$

where  $U = e^{iH_0 t}$  and  $H_0$  is the bare atom Hamiltonian. The Hamiltonian  $H_I'$  achieved from Eq. (3.20) is called the interaction picture Hamiltonian, is given below

$$\begin{aligned}
 H_I' = & -\frac{\hbar}{2}(e^{-i(\omega_c - \omega_{23})t} + e^{i(\omega_c + \omega_{23})t})(\Omega_c|2\rangle\langle 3|) \\
 & -\frac{\hbar}{2}(e^{-i(\omega_p - \omega_{13})t} + e^{i(\omega_p + \omega_{13})t})(\Omega_p|1\rangle\langle 3|) \\
 & -\frac{\hbar}{2}(e^{-i(\omega_d - \omega_{24})t} + e^{i(\omega_d + \omega_{24})t})(\Omega_d|2\rangle\langle 4|) + H.C.
 \end{aligned} \tag{3.21}$$

Now, the RWA advocates that the exponentials with positive arguments results in oscillations at time scales that are very fast compared to the slowly oscillating parts described by the negative arguments in the exponentials, so, these rapidly oscillating terms can be safely dropped out without even showing any violation of conservation laws when measured at time scales defined by the slowly oscillating terms. Therefore, Eq. (3.21) after the RWA takes the form

$$\begin{aligned}
 H_I' = & -\frac{\hbar}{2}(e^{-i(\omega_c - \omega_{23})t})(\Omega_c|2\rangle\langle 3|) - \frac{\hbar}{2}(e^{-i(\omega_p - \omega_{13})t})(\Omega_p|1\rangle\langle 3|) - \\
 & \frac{\hbar}{2}(e^{-i(\omega_d - \omega_{24})t})(\Omega_d|2\rangle\langle 4|) + H.C.
 \end{aligned}$$

or



$$H_I' = -\frac{\hbar\Omega_c}{2}e^{-i\Delta_c t}|2\rangle\langle 3| - \frac{\hbar\Omega_p}{2}e^{-i\Delta_p t}|1\rangle\langle 3| - \frac{\hbar\Omega_d}{2}e^{-i\Delta_d t}|2\rangle\langle 4| + H.C \quad (3.22)$$

where  $\Delta_c = \omega_c - \omega_{23}$ ,  $\Delta_p = \omega_p - \omega_{13}$  and  $\Delta_d = \omega_d - \omega_{24}$  are the detuning of the laser beams from their respective transitions. This Eq. (3.22) is called the *Interaction picture* Hamiltonian after RWA and SVEA for our N-type system. We can now transform back to the *Schrödinger picture* Hamiltonian by reversing the transformation of Eq. (3.20) to get

$$H_I = -\frac{\hbar\Omega_c}{2}e^{-i\omega_c t}|2\rangle\langle 3| - \frac{\hbar\Omega_p}{2}e^{-i\omega_p t}|1\rangle\langle 3| - \frac{\hbar\Omega_d}{2}e^{-i\omega_d t}|2\rangle\langle 4| + H.C \quad (3.23)$$

Now, Eq. (3.1) becomes (after substituting Eq. (3.3) and Eq. (3.23))

$$H = \sum_{a=1}^4 \hbar\omega_a(|a\rangle\langle a|) - \frac{\hbar\Omega_c}{2}e^{-i\omega_c t}|2\rangle\langle 3| - \frac{\hbar\Omega_p}{2}e^{-i\omega_p t}|1\rangle\langle 3| - \frac{\hbar\Omega_d}{2}e^{-i\omega_d t}|2\rangle\langle 4| + H.C \quad (3.24)$$

This is the total Hamiltonian for our N-type system under study. Here, the first term in Eq. (3.24) is the bare atom Hamiltonian (when no laser light is shining on the atoms) and the remaining terms correspond to the interaction of the three lasers with the  $^{87}\text{Rb}$  atom. This Hamiltonian can now be used to calculate the equations of motion for the population of various atomic states as a function of the probe frequency.

### 3.3.1 Equations of motion for the system density matrix

The density matrix method is used when we have an ensemble of systems. We can calculate the dynamics of the total system from the equations of motion of the various components of the density matrix. For our N-type system the density matrix is given by the following matrix

$$\rho = \begin{pmatrix} \rho_{11} & \rho_{12} & \rho_{13} \\ \rho_{21} & \rho_{22} & \rho_{23} \\ \rho_{31} & \rho_{32} & \rho_{33} \end{pmatrix} \quad (3.25)$$

The equivalent to the Schrödinger's equation of motion for the components of the density matrix elements is called the von Neumann equation (including the decay terms added phenomenologically), and is given by<sup>[11]</sup>

$$\dot{\rho}_{ij} = -\frac{i}{\hbar} \sum_{k=1}^4 (H_{ik} \rho_{kj} - \rho_{ik} H_{kj}) - \frac{1}{2} \sum_{k=1}^4 (\Gamma_{ik} \rho_{kj} + \rho_{ik} \Gamma_{kj}) \quad (3.26)$$

where  $\Gamma$  is the decay operator defined as  $\langle m|\Gamma|n\rangle = \gamma_{mn} \delta_{mn}$ ,  $\gamma_{mn}$  are the decay rate constants of the population from level  $|m\rangle$  to a lower level  $|n\rangle$ , and the Hamiltonian matrix elements  $H_{mn} = \langle m|H|n\rangle$  for our four-level N-type system are given below

$$\begin{bmatrix} H_{11} & H_{12} & H_{13} & H_{14} \\ H_{21} & H_{22} & H_{23} & H_{24} \\ H_{31} & H_{32} & H_{33} & H_{34} \\ H_{41} & H_{42} & H_{43} & H_{44} \end{bmatrix} = \frac{\hbar}{2} \begin{bmatrix} 2\omega_1 & 0 & -\Omega_p e^{-i\omega_p t} & 0 \\ 0 & 2\omega_2 & -\Omega_c e^{-i\omega_c t} & -\Omega_d e^{-i\omega_d t} \\ -\Omega_p e^{+i\omega_p t} & -\Omega_c e^{+i\omega_c t} & 2\omega_3 & 0 \\ 0 & -\Omega_d e^{+i\omega_d t} & 0 & 2\omega_4 \end{bmatrix} \quad (3.27)$$

Similarly, we can also calculate the matrix elements  $\Gamma_{ij}$  from  $\langle m|\Gamma|n\rangle = \gamma_{mn} \delta_{mn}$ . The time dependence in the components of the Hamiltonian (3.27) can be removed by transforming the Hamiltonian to a rotating frame to simplify the mathematical operations at this stage, or can be later transformed when solving for the steady state solutions of the density matrix components.

Now we can use Eq. (3.26) to calculate the 16 equations of motion for the density matrix components using Eq. (3.27). For the sake of demonstration (and due to our interest in this particular term), we calculate just one of the 16 equations of motion. e.g.

$$\begin{aligned} \dot{\rho}_{31} = & -\frac{i}{\hbar} (H_{31} \rho_{11} - \rho_{31} H_{11} + H_{32} \rho_{21} - \rho_{32} H_{21} + H_{33} \rho_{31} - \rho_{33} H_{31} \\ & + H_{34} \rho_{41} - \rho_{34} H_{41}) - \frac{1}{2} (\Gamma_{31} \rho_{11} + \rho_{31} \Gamma_{11} + \Gamma_{32} \rho_{21} \\ & + \rho_{32} \Gamma_{21} + \Gamma_{33} \rho_{31} + \rho_{33} \Gamma_{31} + \Gamma_{34} \rho_{41} + \rho_{34} \Gamma_{41}) \end{aligned} \quad (3.28)$$

using the  $H_{ij}$  component values from Eq. (3.27) and the fact that  $\Gamma_{ij} = 0 \forall i \neq j$ , we get

$$\begin{aligned}
 \rho_{31} \dot{=} & -\frac{i}{\hbar} \times \frac{\hbar}{2} \left( -\Omega_p e^{+i\omega_p t} \rho_{11} - \rho_{31} 2\omega_1 - \Omega_c e^{+i\omega_c t} \rho_{21} - 0 + 2\omega_3 \rho_{31} \right. \\
 & \left. + \rho_{33} \Omega_p e^{+i\omega_p t} + 0 - 0 \right) - \frac{1}{2} (0 + \rho_{31} \gamma_{11} + 0 + 0 \\
 & + \gamma_{33} \rho_{31} + 0 + 0 + 0)
 \end{aligned} \tag{3.29}$$

which simplifies to

$$\begin{aligned}
 \rho_{31} \dot{=} & -i \left( -\frac{\Omega_p}{2} e^{+i\omega_p t} \rho_{11} - \omega_1 \rho_{31} - \frac{\Omega_c}{2} e^{+i\omega_c t} \rho_{21} + \omega_3 \rho_{31} \right. \\
 & \left. + \rho_{33} \frac{\Omega_p}{2} e^{+i\omega_p t} \right) - \gamma_{31} \rho_{31}
 \end{aligned} \tag{3.30}$$

where we have defined the coherence decay rate  $\gamma_{31} = \frac{\gamma_{11} + \gamma_{33}}{2}$ . In a similar fashion, we can calculate all the  $\rho_{ij}$  and then we can simultaneously solve them for any one of them<sup>[37]</sup>. The probe absorption properties in the N-type system can be deduced from the steady state solution of the  $\rho_{31}$ .

### 3.3.2 Solution to the equations of motion

To get the steady state solution, we do the assumptions that the populations of all the  $\rho_{ij}$  in the beginning are zero except that of  $\rho_{11}$  i.e. all the atoms are initially in the  $F=2$  state. Also, we assume that the  $\gamma_{12}$  is very small compared to the other decay rates and all the Rabi frequencies (the condition that  $\gamma_{12}$  should be small is very well met by the dephasing/decoherence rate between the  $F=2$  state and  $F=1$  state of the  $^{87}\text{Rb}$  D1 line). Then, in the weak probe approximation, we get a solution for the coherence

$$\rho_{31} = \frac{\Omega_p (\gamma'_{21} \gamma'_{41} - \Omega_d^2)}{(\gamma'_{31} (\gamma'_{21} \gamma'_{41} - \Omega_d^2) - \gamma'_{41} \Omega_c^2)} \tag{3.31}$$

here  $\gamma'_{21} = -i\gamma_{21} + (\Delta_p - \Delta_c)$ ,  $\gamma'_{31} = \Delta_p - i\gamma_{31}$ ,  $\gamma'_{41} = \Delta_p - \Delta_c + \Delta_d - i\gamma_{41}$  are the effective decay rates of the respective coherences and  $\Delta_p = \omega_{21} - \omega_p$ ,  $\Delta_c = \omega_{23} - \omega_c$ , and  $\Delta_d = \omega_{42} - \omega_d$  are the detuning.

The absorption spectrum of the probe laser in our N-type system can be obtained by plotting the imaginary part of Eq. (3.31) while its real part gives us the dispersion properties (refractive index, group velocity etc.) of the medium as seen by the probe laser (the

electronic polarizability seen by the probe laser  $\chi$  depends linearly on  $\rho_{31}$  so the shape of the spectrum for both  $\chi$  and  $\rho_{31}$  is, to within a multiplicative constant, the same<sup>[11]</sup>). The characteristic EIA-like three absorption peaks and their positions can be predicted by the same equation. It is important to mention that if we put  $\Omega_d = 0$  (turn OFF the driving laser), the N-type system reduces to a lambda-type system and an EIT like shape is recovered.

### 3.4 Dressed state picture of the N-type System

To see the N-type system's behavior in the weak probe regime, we can assume that the probe laser strength  $\Omega_p \rightarrow 0$  which will effectively decouple the state  $|1\rangle$  from the rest of the system and the  $4 \times 4$  matrix given by Eq. (3.27) will reduce to a  $3 \times 3$  matrix (Eq. (3.24) will also change in the new frame, for example see<sup>[36]</sup>), and the new system will have three Eigen values resulting in three Eigen vectors, which are called the dressed states of the N-type system in the weak probe frame<sup>[37, 38]</sup>. These dressed states, after the solution of the matrix, are given by the following equations

$$|\beta_0\rangle = \frac{(-\Omega_d|3\rangle + \Omega_c|4\rangle)}{\sqrt{\Omega_c^2 + \Omega_d^2}} \quad (3.32a)$$

$$|\beta_1\rangle = \frac{1}{\sqrt{2}} \left( |2\rangle + \frac{\Omega_c}{\sqrt{(\Omega_c^2 + \Omega_d^2)}} |3\rangle + \frac{\Omega_d}{\sqrt{(\Omega_c^2 + \Omega_d^2)}} |4\rangle \right) \quad (3.32b)$$

and

$$|\beta_2\rangle = \frac{1}{\sqrt{2}} \left( -|2\rangle + \frac{1}{\sqrt{2}} \frac{\Omega_c}{\sqrt{(\Omega_c^2 + \Omega_d^2)}} |3\rangle + \frac{\Omega_d}{\sqrt{(\Omega_c^2 + \Omega_d^2)}} |4\rangle \right) \quad (3.32c)$$

Now if the probe field becomes non-zero ( $\Omega_p \neq 0$ ), the probe will connect the ground state  $|1\rangle$  with these three dressed states formed by the coupling and driving lasers and we will have absorption whenever the probe frequency matches the separation of these states from the ground state  $|1\rangle$ . Three absorption peaks (or transmission dips) are expected from our N-type system as dictated by Eq. (3.32) and (3.31). The energy difference between

### Chapter 3: Study of an N-Type atomic level system in a Bose-Einstein condensate

these three dressed states is of  $\sqrt{\Omega_c^2 + \Omega_d^2}$  provided both the coupling and driving lasers are tuned to the resonance frequencies of their respective transitions.

In Fig. (3.3) the theoretical and experimental spectra are shown for both the N-type and the lambda-type systems. It is clear that how the introduction of the driving laser into the system changes the transparency window of the EIT and the probe beam is absorbed now at this transparency position. The N-type system has a spectrum similar to the EIA at the center but the coherent phenomena responsible for EIA are not limited to our N-type system, as EIA can be also induced by the use of different polarization fields to drive transitions from degenerate magnetic sublevels of the same hyperfine state without the use of an extra hyperfine state<sup>[39, 40]</sup>. Particularly, in Ref.<sup>[40]</sup>, the sublevels of just three hyperfine

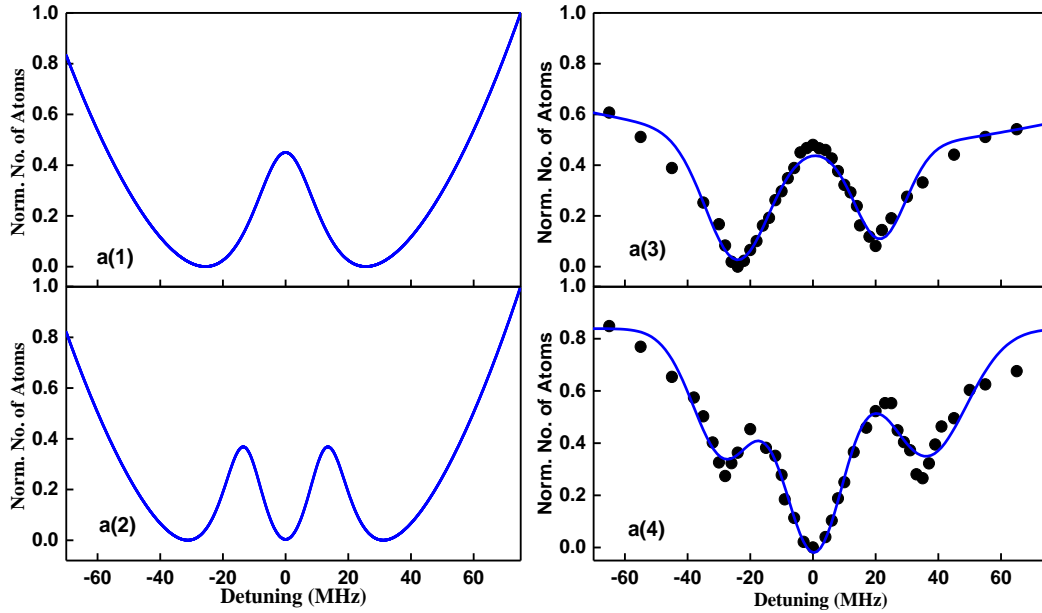


Figure 3.3. Theoretical and experimental spectra of the  $\Lambda$ -type and N-type. a(1) and a(3) represent the theoretical and experimental results of the  $\Lambda$ -type system. a(2) and a(4) respectively represent the theoretical and experimental results in the case of our N-type system. The introduction of the driving laser changes the EIT into an EIA-like spectrum. The powers are: coupling and driving lasers in both a(3) are  $P_c = 400 \mu W, P_d = 0 \mu W$  and a(4) are  $P_c = 400 \mu W, P_d = 200 \mu W$  while in both cases  $P_p = 25 \mu W$ . Both a(1) and a(2) are plotted from the imaginary part of Eq. (2.31) with  $\Omega_d = 0$  in a(1).

states are used to construct many N-type systems which result in EIA which is quite different from our N-type system involving four hyperfine states. EIA is observed in four level

systems inside two degenerate states that are open, or even more than two states but the basic physics behind the EIA in such systems is the transfer of population or transfer of coherence<sup>[19, 41-44]</sup>. Our N-type system however, is a closed system. Apart from the controversy about the nomenclature, the experimental features agree fairly well with the theoretical results of Eq. (3.31) and that is what really is important. The suppression of the transparency windows by the driving laser can be used for all optical switching of the resonance frequency or three frequencies simultaneously. The dips are broadened due to the use of high laser powers in all of the three lasers although the probe laser is 8 times weaker than the coupling and driving lasers. The positions of these three dips can be changed easily by tuning the power and the detuning of the coupling and driving lasers, as discussed in the following sections. This tunability makes this system a potential candidate for a variable frequency optical switch.

### 3.5 Experimental procedure

The experimental setup is displayed in Fig. 3.2. The BEC is prepared in a crossed beam optical dipole trap with a Thomas-Fermi radius of  $20 \mu\text{m}$  and all the  $1 \times 10^6$  atoms are in the  $|1\rangle = |F = 2, m_F = 2\rangle$  state. Right after when the BEC is ready, the three experimental lasers (coupling, driving and probe) are turned for  $10 \mu\text{s}$  simultaneously. Both the coupling and driving beams have a  $1/e^2$  radius of around  $280 \mu\text{m}$  while the probe beam has a  $600 \mu\text{m}$  radius at the position of the BEC. The larger size of the probe beam further makes it weaker so that the weak probe regime is satisfied. The spectrum of the N-type system (Fig. 3.3(a(4))) is recorded by preparing a new BEC sample each time and exposing it to the three experimental lasers simultaneously, while every time changing the frequency of the probe laser. After exposure to the three lasers, the atomic cloud is imaged after waiting for 30 ms to get a better resolvable atomic cloud. The imaging laser is locked between the  $|F = 2, m_F = 2\rangle$  and  $|F' = 3\rangle$  of the D2 line and the images are taken by a CCD camera and then processed by a software to measure the number of atoms remaining in the cloud. The probe laser will be strongly absorbed at the three dressed states frequency positions while it will be less absorbed at other frequencies. The strong absorption leads to the heating of the BEC and the more atoms will escape the atomic cloud during the 30 ms ballistic

expansion interval. Therefore, lesser atoms will be left for the imaging system to detect and thus we get the three dips in Fig. 3.3 (a(4)). A weak absorption will not affect the BEC temperature too much and hence the remaining number of atoms will be almost the same as that of the BEC when it was before exposure to the three experimental beams. Each spectral point in Fig. 3.3(a(4)) is recorded one time only as the experiment is for the demonstration of the proof of concept of the observation of an N-type system using absorption imaging technique and not for sensitive metrological point of view. The laser powers are controlled using AOMs which are driven by stable function generators (not by the homemade RF driver circuits) and the power are very stable during the  $10 \mu\text{S}$  exposure time. Therefore,

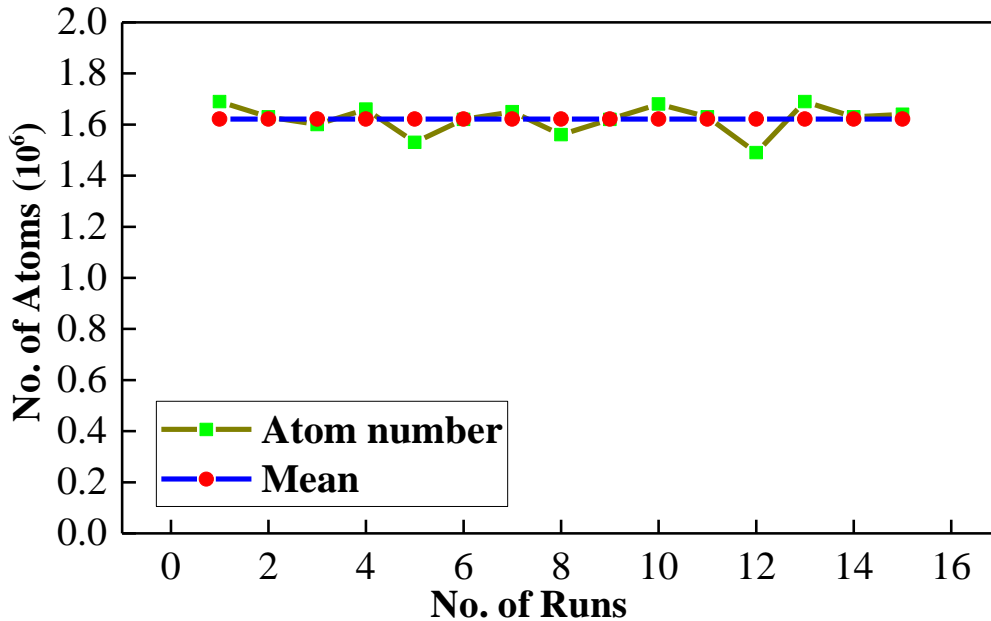


Figure 3.4. The number of atoms during consecutive experimental runs plotted together with the mean of all the data shows the amount of fluctuations in each freshly prepared sample of BEC during the recording of our data. This is the number of atoms in the BEC in the  $|F = 2, m_F = 2\rangle$  state after a 30 ms of ballistic expansion and is not exposed to any experimental beams.

the biggest noise source in the experiment is the fluctuation of the number of atoms in each fresh sample of BEC prepared for the recording of a new spectral point<sup>[45]</sup>. However, the atoms number fluctuation is not big enough to hide any important features of the N-type system using absorption imaging. The atom number fluctuation during 15 consecutive runs is shown in Fig. 3.4 together with the mean of the total points.

### 3.6 Further properties of the N-type system

As discussed earlier, the shape of the experimental absorption spectrum resembles fairly well with the theoretical model of Eq. (3.31). The laser power, detuning and polarizations are some parameters that give us freedom to test the system further by tuning them. Here we present the spectra of the system when some of these parameters are tuned individually while keeping the other parameters constant, and give the theoretical explanation of the observed spectra. Some of the shortcomings of our theoretical model are also pointed out and possible solutions to the unexplained behaviors are mentioned. Fig. 3.5 shows the spectra when the detuning of the coupling and driving lasers are changed. The detuning of both the driving and coupling lasers were changed using the AOMs and the frequency of the probe laser was controlled by the local oscillator of the OPLL system. Both the coupling and driving laser beams pass through different AOMS but are combined in a single mode fiber (SMF) before the BEC cell to get a high degree of collinearity (although it is not very important in the case of BEC as there is practically no Doppler broadening and the magnetic field is minimal so no big Zeeman splitting is possible).

All the three dips shift in the same direction for increasing detuning of the coupling laser. The same happens for the case of driving laser but in opposite direction to that of the coupling laser. This behavior is also predicted by the theoretical model of Eq. (3.31) and can also be explained from the dressed state picture of the N-type system (of Eq. (3.32)) as the mixing strengths of the atomic energy levels are controlled by the Rabi frequencies of these lasers which are affected by the amount of detuning.

Similar shifting is observed when we changed the powers of the two lasers one by one as shown in Fig. 3.6. But now, the shifting is in the same direction in the frequency domain for both the lasers. Again, the theoretical model presented above can reproduce the experimentally observed results due to the increase of power (AC stark shift).

However, the dip towards the blue side shifts more when we increase the detuning (Fig. 3.5a(3)) or power (Fig. 3.6a(4), b(4)) and this asymmetric shifting cannot be explained from our theoretical models of Eq. (3.31 and 3.32).



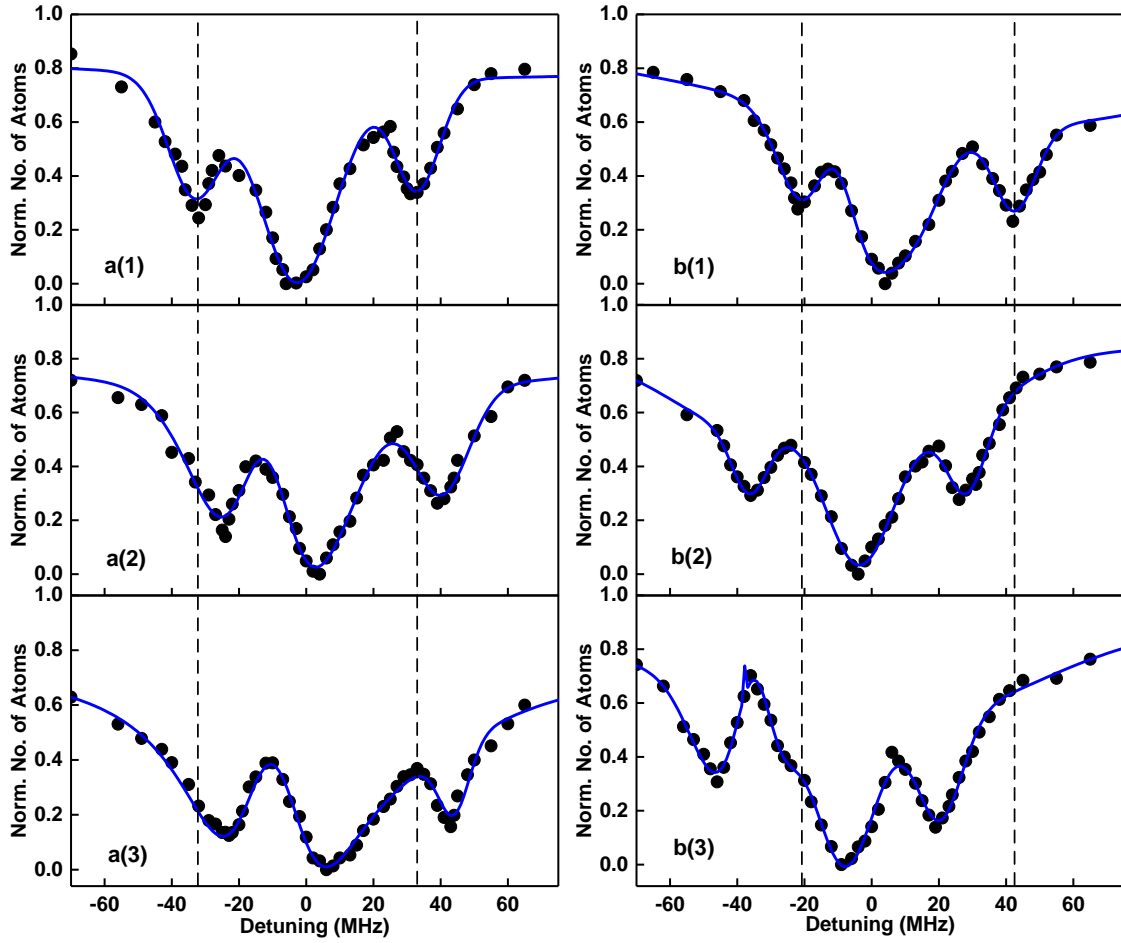


Figure 3.5. The remaining atom number in the  $|F = 2, m_F = 2\rangle$  state in the BEC against the probe detuning at fixed but different detuning of the coupling and driving fields. From a(1)-a(3) the figures show the effect of driving laser detuning on the three dips while from figures b(1)- b(3) the effect of the coupling laser detuning on the dips is shown. a(1)  $\Delta_c = 0, \Delta_d = +10 \text{ MHz}$ . a(2)  $\Delta_c = 0, \Delta_d = -10 \text{ MHz}$ . a(3)  $\Delta_c = 0, \Delta_d = -20 \text{ MHz}$ . b(1)  $\Delta_c = +10 \text{ MHz}, \Delta_d = 0$ . b(2)  $\Delta_c = -10 \text{ MHz}, \Delta_d = 0$ . b(3)  $\Delta_c = -20 \text{ MHz}, \Delta_d = 0$ . Probe laser power is  $P_p = 25 \mu\text{W}$  and the coupling and driving laser powers are  $P_c = 400 \mu\text{W}, P_d = 200 \mu\text{W}$  respectively. The solid curves in the plots serve as guides to the eye.

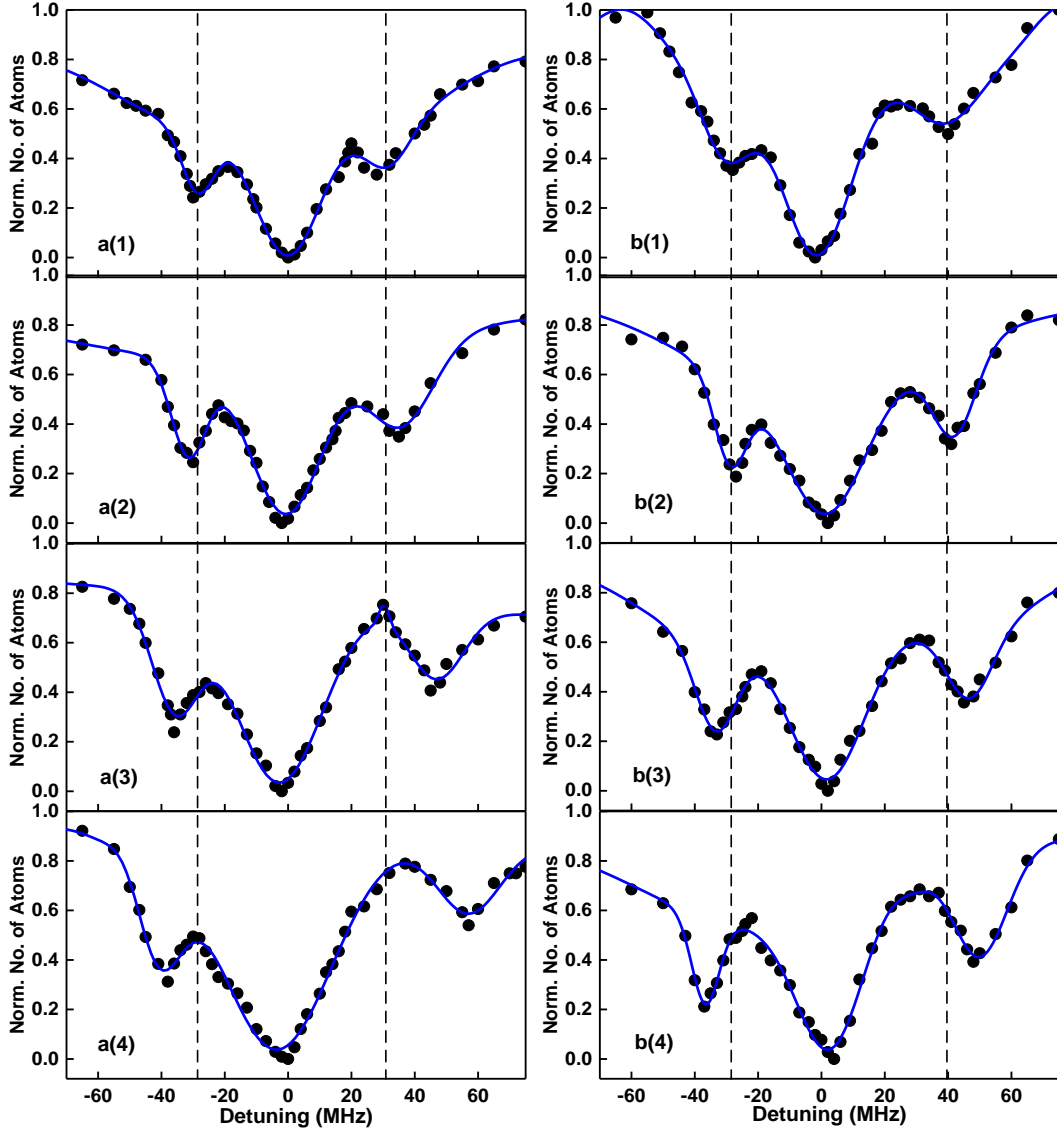


Figure 3.6. The remaining atom number in the  $|F = 2, m_F = 2\rangle$  state in the BEC against the probe detuning at various powers of the coupling and driving fields. Figures a(1)-a(4) show the effect of changing the driving laser power when the coupling laser was at constant power. Similarly, figures b(1)-b(4) show the effect of changing coupling laser power when the driving laser was at constant power. a(1)  $P_c = 400 \mu\text{W}, P_d = 100 \mu\text{W}$ . a(2)  $P_c = 400 \mu\text{W}, P_d = 200 \mu\text{W}$ . a(3)  $P_c = 400 \mu\text{W}, P_d = 400 \mu\text{W}$ . a(4)  $P_c = 400 \mu\text{W}, P_d = 800 \mu\text{W}$ . b(1)  $P_c = 100 \mu\text{W}, P_d = 400 \mu\text{W}$ . b(2)  $P_c = 200 \mu\text{W}, P_d = 400 \mu\text{W}$ . b(3)  $P_c = 600 \mu\text{W}, P_d = 400 \mu\text{W}$ . b(4)  $P_c = 800 \mu\text{W}, P_d = 400 \mu\text{W}, P_p = 25 \mu\text{W}$ , and  $\Delta_c = 0, \Delta_d = 0$ . The solid curves in the plots serve as guides to the eye.

### Chapter 3: Study of an N-Type atomic level system in a Bose-Einstein condensate

The reason for this is that as we increase the power or detuning and when the blue side dip is shifting away from the central dip, the uncoupled excited hyperfine level ( $F'=2$  of the D1 line) is also mixed with the N-type system and it is this extra level which put its weight in and causes asymmetric shifting<sup>[37]</sup>. The existence of some photo-association dips on both the red and blue sides of the atomic resonance can also affect the observed shapes, as will be discussed in the next chapter.

Some other interesting phenomena are presented in Fig. 3.7. The EIA-like absorption effect can even survive for driving powers of as low as  $10 \mu W$  when the coupling laser power is  $400 \mu W$ . This means that a small power of  $10 \mu W$  (distributed over a beam size of  $\approx 200 \mu m$ ) of resonant driving laser is enough to suppress the transparency window of a  $\Lambda$ -type system as shown in Fig. 2.7a(1). However, when a largely detuned ( $+220$  MHz of detuning from the respective transition) driving laser is used, using even a high power ( $200 \mu W$ ) of the same laser cannot suppress the transparency window and the N-type system behaves as a  $\Lambda$ -type system as can be seen in Fig. 3.7a(2). This behavior of the N-type system acting as a  $\Lambda$ -type system for larger driving laser detuning can also be simulated from the theoretical model of Eq. (3.31). This behavior of the conversion of N-type system to a  $\Lambda$ -type system is also reported in a previous study in Ref.<sup>[18]</sup>. As discussed earlier, there is a small magnetic field present (along the vertical direction) during the exposure of the BEC to the experimental beams. This magnetic field provides a quantization direction for the transitions involved. The probe laser polarization makes a small angle of around  $10^\circ$  with the vertical thus  $\pi$ -transition is the most favored transition and a small number of  $\sigma^+$  and  $\sigma^-$ -transitions are also allowed. But as the BEC is prepared in the stretched state of  $|F = 2, m_F = 2\rangle$ , the major part of the probe laser power is useless as only  $\sigma^-$ -transitions are allowed in our N-type system. By rotating the polarization of the probe laser by  $50^\circ$  in the lab frame, more power is now available for the  $\sigma^-$ -transitions and the effective probe power increases. The coupling and driving lasers are vertically polarized and only allow  $\pi$ -transitions. So, a rotated polarization of the probe beam would cause increased effective probe laser power and there will be strong absorptions and power broadening in the system. Fig. 3.8a(1) represents such a case and very prominent power broadening is observed at the central dip.

## Excitation spectrum and coherent phenomena in $^{87}\text{Rb}$ Bose-Einstein condensates

When the coupling and driving laser polarizations were also rotated by  $20^\circ$ , transitions other than the  $\pi$ -transitions can also now take part, and the N-type system becomes a complex of subsystems. The total effect, as is clear from Fig. 3.8a(2), is the reduction of the effective coupling and driving laser power. The theoretical model for this situation however,

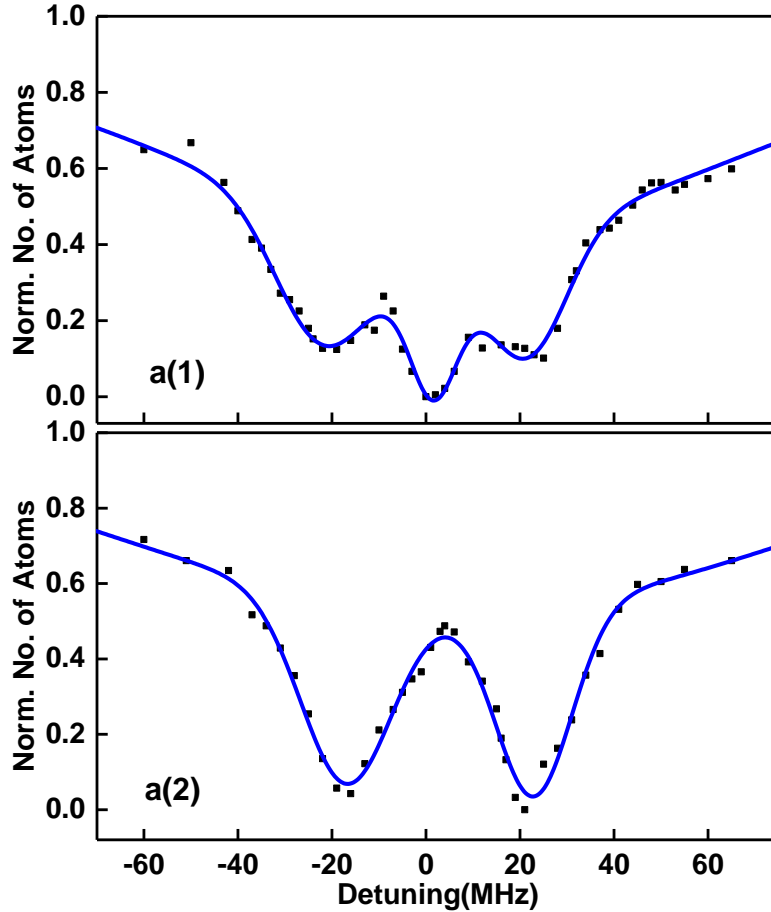


Figure 3.7. The behavior of the spectrum of our N-type system against a(1) very small driving power while at resonance and a(2) large detuning and large power. The coupling laser power in a(1) is  $P_c = 400 \mu W$  while the driving laser power is  $P_d = 10 \mu W$ . Both the coupling and driving lasers are tuned to the resonance of their respective driving transitions. In a(2),  $P_c = 400 \mu W$  and is at resonance to its respective transition while  $P_d = 200 \mu W$  and  $\Delta_d = +220 \text{ MHz}$ . Probe laser power in both of these figures is the same as in all of the above.

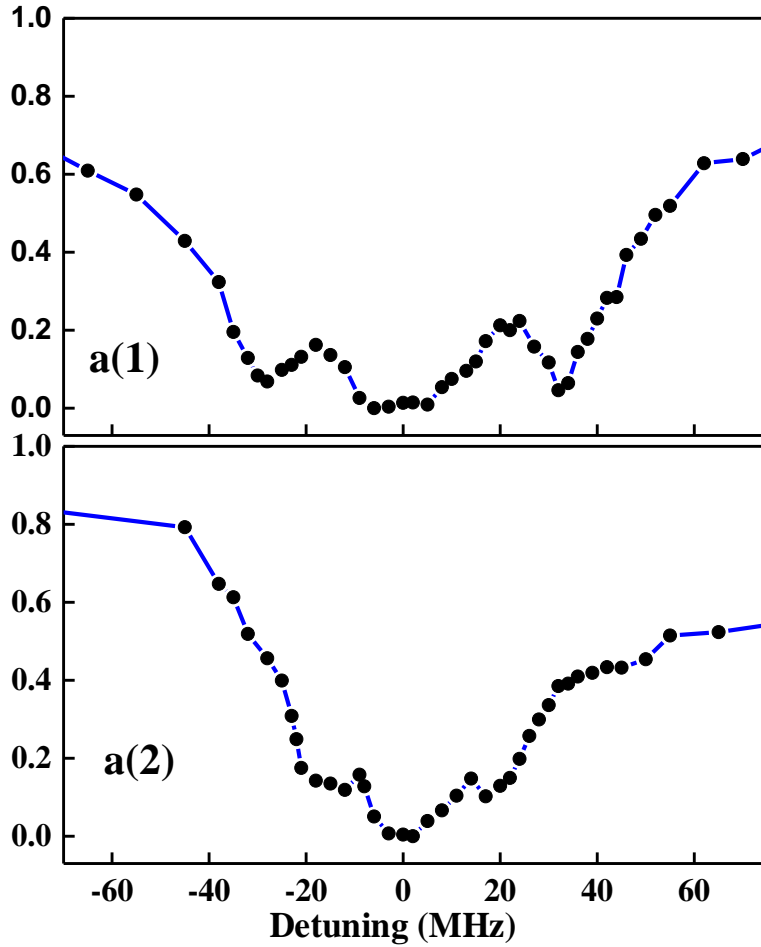


Figure 3.8. Effect of the probe, coupling and driving laser polarizations on the N-type system. a(1) The spectrum when the probe laser beam polarization makes an angle of  $50^\circ$  with the vertical (with the magnetic field direction) while coupling and driving lasers are polarized along the vertical direction. a(2) when the probe polarization is same as a(1) but the coupling and driving laser polarizations are also now making an angle of  $20^\circ$  with the vertical.

is not presented here but one can see from the figure that the two dips comes closer to the central dip and such a behavior is equivalent to the reduction of the coupling and/or driving laser power.

### 3.7 Summary and conclusions

Our study is very important in the theoretical and experimental realization of coherent as well as spectroscopic schemes involving  $^{87}\text{Rb}$  condensates. Although slower in data acquisition to the ones using a free running probe laser and using hot atomic vapors, the use of BEC for the studies of such coherent systems have the merits of a thermally ideal

## Excitation spectrum and coherent phenomena in $^{87}\text{Rb}$ Bose-Einstein condensates

environment and a more controllable platform. The observed findings can be used in any future experimental schemes of optical switching and tuning of the dispersion properties of the medium involving such N-type or EIT schemes. Examples of such schemes may include optical lattices, phase control of optical signals, optical gating for quantum communication and quantum computing and so on. Our experiments also suggest that the use of absorption imaging technique can be employed when studying the coherent properties inside the Bose-condensed state of matter as such systems are optically dense and transmission spectroscopy in such systems will need high power probe beams for further detection which are against the requirements set on the probe laser power. Furthermore, the complete description of the polarization effects on the N-type system spectra also calls for more inclusive theoretical formulations in these types of coherent systems.

## References

- [1] S.E. Harris. Electromagnetically Induced Transparency. *Physics Today*, 1997, 50, 36.
- [2] K. J. Boller, A. Imamoglu, and S. E. Harris. Observation of electromagnetically induced transparency. *Phys. Rev. Lett.*, 1991, 66, 2593.
- [3] H. Kang, L. Wen, and Y. Zhu. Normal or anomalous dispersion and gain in a resonant coherent medium. *Phys. Rev. A*, 2003, 68, 063806.
- [4] A. M. Akulshin, S. Barreiro and A. Lezama. Steep Anomalous Dispersion in Coherently Prepared Rb Vapor. *Phys. Rev. Lett.*, 1999, 83, 4277.
- [5] D. Budker, D. F. Kimball, S. M. Rochester and V. V. Yashchuk. Nonlinear Magneto-optics and Reduced Group Velocity of Light in Atomic Vapor with Slow Ground State Relaxation. *Phys. Rev. Lett.*, 1999, 83, 1767.
- [6] S. E. Harris, J. E. Field, and A. Imamoglu. Nonlinear optical processes using electromagnetically induced transparency. *Phys. Rev. Lett.*, 1990, 64, 1107.
- [7] D. A. Braje, V. Balić, S. Goda, G. Y. Yin, and S. E. Harris. Frequency Mixing Using Electromagnetically Induced Transparency in Cold Atoms. *Phys. Rev. Lett.*, 2004, 93, 183601.
- [8] S. A. Babin, E. V. Podivilov, D. A. Shapiro, U. Hinze, E. Tiemann, and B. Wellegehausen. Effects of strong driving fields in resonant four-wave mixing schemes with down-conversion. *Phys. Rev. A*, 1999, 59, 1355.
- [9] D. F. Phillips, A. Fleischhauer, A. Mair, R. L. Walsworth, and M. D. Lukin. Storage of Light in Atomic Vapor. *Phys. Rev. Lett.*, 2001, 86, 783.
- [10] M. O. Scully, S. Y. Zhu, and Athanasios Gavrielides. Degenerate quantum-beat laser: Lasing without inversion and inversion without lasing. *Phys. Rev. Lett.*, 1989, 62, 2813.
- [11] M. O. Scully and M. S. Zubairy. *Quantum Optics*. Cambridge, Cambridge University Press, 1997.
- [12] H. R. Xia, C. Y. Ye, and S. Y. Zhu. Experimental Observation of Spontaneous Emission Cancellation. *Phys. Rev. Lett.*, 1996, 77, 1032.
- [13] A. V. Taichenachev, A. M. Tumaikin, and V. I. Yudin. Electromagnetically induced absorption in a four-state system. *Phys. Rev. A* 1999, 61, 011802.

- [14] P. Valente, H. Failache, and A. Lezama. Temporal buildup of electromagnetically induced transparency and absorption resonances in degenerate two-level transitions. *Phys. Rev. A*, 2003, 67, 013806.
- [15] C. P. Liu, S. Q. Gong, X. J. Fan, and Z. Z. Xu. Electromagnetically induced absorption via spontaneously generated coherence of a  $\Lambda$  system. *Optics Communications*, 2004, 231, 289.
- [16] A. Lezama, S. Barreiro, and A. M. Akulshin. Electromagnetically induced absorption. *Phys. Rev. A*, 1999, 59, 4732.
- [17] O. Kocharovskaya. Amplification and lasing without inversion. *Physics Reports*, 1992, 219, 175 .
- [18] R. G. Wan, J. Kou, L. Jiang, S. Q. Kuang, Y. Jiang, and J. Y. Gao. Coherently induced double photonic band gaps in a driven N-type atomic system. *Optics Communications*, 2011, 284, 1569.
- [19] L. B. Kong, X. H. Tu, J. Wang, Y. Zhu, and M. S. Zhan. Sub-Doppler spectral resolution in a resonantly driven four-level coherent medium. *Optics Communications*, 2007, 269, 362.
- [20] M. Fleischhauer, A. Imamoglu, and J. P. Marangos, Electromagnetically induced transparency: optics in coherent media. *Rev. Mod. Phys.*, 2005, 77, 633.
- [21] T. Naseri and M. Hatami-Mehr. Investigating tunable bandwidth cavity via three-level atomic systems. *The European Physical Journal Plus*, 2019, 134, 529.
- [22] M. Mücke, E. Figueroa, J. Bochmann, C. Hahn, K. Murr, S. Ritter, C. J. Villas-Boas and Gerhard Rempe. Electromagnetically induced transparency with single atoms in a cavity. *Nature*, 2010, 465, 755.
- [23] S. Weis, R. Rivière, S. Deléglise, E. Gavartin, O. Arcizet, A. Schliesser, and T. J. Kippenberg. Optomechanically Induced Transparency. *Science*, 2010, 330, 1520.
- [24] A. H. Safavi-Naeini, T. P. Mayer Alegre, J. Chan, M. Eichenfield, M. Winger, Q. Lin, J. T. Hill, D. E. Chang, and O. Painter. Electromagnetically induced transparency and slow light with optomechanics. *Nature*, 2011, 472, 69.



### Chapter 3: Study of an N-Type atomic level system in a Bose-Einstein condensate

- [25] A. A. Abdumalikov, J., O. Astafiev, A. M. Zagoskin, Yu. A. Pashkin, Y. Nakamura, and J. S. Tsai. Electromagnetically Induced Transparency on a Single Artificial Atom. *Phys. Rev. Lett.*, 2010, 104, 193601.
- [26] M. L. Wan, J. N. He, Y. L. Song, and F. Q. Zhou. Electromagnetically induced transparency and absorption in plasmonic metasurfaces based on near-field coupling. *Physics Letters A*, 2015, 379, 1791.
- [27] M. Yan, E. G. Rickey, and Y. Zhu. Observation of doubly dressed states in cold atoms. *Phys. Rev. A*, 2001, 64, 013412.
- [28] L. G. Wang, M. Ikram, and M. S. Zubairy. Control of the Goos-Hänchen shift of a light beam via a coherent driving field. *Phys. Rev. A*, 2008, 77, 023811.
- [29] D. X. Khoa, P. V. Trong, L. V. Doai, and N. H. Bang. Electromagnetically induced transparency in a five-level cascade system under Doppler broadening: an analytical approach. *Phys. Scr.*, 2016, 91, 035401.
- [30] Y. Qi, F. Zhou, T. Huang, Y. Niu, and S. Gong. Three-dimensional atom localization in a five-level M-type atomic system. *Journal of Modern Optics*, 2012, 59, 1092.
- [31] Z. Nie, H. Zheng, P. Li, Y. Yang, Y. Zhang, and M. Xiao. Interacting multiwave mixing in a five-level atomic system. *Phys. Rev. A*, 2008, 77, 063829.
- [32] I. H. Subba and A. Tripathi. Observation of electromagnetically induced absorption in  $^{87}\text{Rb}$   $D_2$  line in strong transverse magnetic field. *J. Phys. B: At. Mol. Opt. Phys.*, 2018, 51, 155001.
- [33] K. S. Nawaz, C. Mi, L. Chen, P. Wang, and J. Zhang. Experimental Investigation of the Electromagnetically Induced-Absorption-Like Effect for an N-Type Energy Level in a Rubidium BEC. *CHIN. PHYS. LETT.*, 2019, 36, 043201.
- [34] L. Chen, P. Wang, M. Meng, L. Huang, H. Cai, D. Wang, S. Zhu and J. Zhang. Experimental observation of one-dimensional superradiance lattices in ultracold atoms. *Phys. Rev. Lett.*, 2018, 120, 193601.
- [35] M. Meng and J. Zhang. Phase-Locked Laser System Used for Electromagnetically Induced Transparency Spectral Experiments. *ACTA OPTICA SINICA*, 2013, 33, 0714001.

- [36] J. O. Weatherall. Quantum control of linear susceptibility in five level atoms via dressed interacting ground states, with a focus on group velocity control. 2009, PhD Thesis, Stevens Institute of Technology.
- [37] J. Sheng, X.Y., H. Wu, and M. Xiao. Modified self-Kerr-nonlinearity in a four-level N-type atomic system. *Phys. Rev. A*, 2011, 84, 053820.
- [38] X. Yang, K. Yang, Y. Niu, and S. Gong. Reversible self-Kerr nonlinearity in an N-type atomic system through a switching field. *J. Opt.*, 2015, 17, 045505.
- [39] S. Dey, N. Aich, C. Chaudhuri, and B. Ray. Investigation of quantum coherence effects in a multilevel atom induced by three laser fields. *Eur. Phys. J. D*, 2015, 69, 43.
- [40] G. Yang, L. Chen, C. Mi, P. Wang, and J. Zhang. Study on electromagnetic induction transparency and electromagnetic induction absorption in boson Einstein condensate. *J. Quantum Opt.*, 2018, 24, 156.
- [41] C. Goren, A. D. Wilson-Gordon, M. Rosenbluh, and H. Friedmann. Electromagnetically induced absorption due to transfer of coherence and to transfer of population. *Phys. Rev. A*, 2003, 67, 033807.
- [42] A. V. Taichenachev, A. M. Tumaikin, and V. I. Yudin. Electromagnetically induced absorption in a four-state system. *Phys. Rev. A*, 1999, 61, 011802(R).
- [43] C. Goren, A. D. Wilson-Gordon, M. Rosenbluh, and H. Friedmann. Atomic four-level N systems. *Phys. Rev. A*, 2004, 69, 053818.
- [44] C. Goren, A. D. Wilson-Gordon, M. Rosenbluh, and H. Friedmann. Electromagnetically induced absorption due to transfer of population in degenerate two-level systems. *Phys. Rev. A*, 2004, 70, 043814.
- [45] M. A. Kristensen, M. B. Christensen, M. Gajdacz, M. Iglicki, K. Pawłowski, C. Klempt, J. F. Sherson, K. Rzążewski, A. J. Hilliard, and J. J. Arlt. Observation of Atom Number Fluctuations in a Bose-Einstein Condensate. *phys. Rev. Lett.*, 2019, 122, 163601.

## **Chapter 4: Photoassociation of the $^{87}\text{Rb}$ BEC near the D1 line threshold**

This chapter of the thesis is based on my work, part of which is published in Phys. Rev. A (Photoassociation spectroscopy of weakly bound  $^{87}\text{Rb}_2$  molecules near the  $5P_{1/2} + 5S_{1/2}$  threshold by optical Bragg scattering in Bose-Einstein condensates, Phys. Rev. A **102**, 053326 (2020)).

### **4.1 Single photon photoprocesses between two atoms**

Light interacts in many interesting ways with atoms depending on its wavelength. As we saw in the previous chapter, a combination of resonant and near resonant light wavelengths can produce coherent effects in the atomic states of the atoms on the individual scale (the effects are limited to each atom no matter how large is the atomic sample, unless we include the effects of other atoms in the form of a mean field potential). Similarly, the light at certain wavelengths may attract or repel atoms from the high intensity regions of the laser beam as in the case of optical dipole trap and the optically plugged magnetic trap. This attraction or repulsion is also limited to atoms on the individual level and does not require more than one atom to be implemented. In other cases, light tuned to special wavelengths far below the resonant atomic transition, can interact with atoms in such a way that an excited and a ground state atom pair is formed which locks together in an attractive potential. Such a process is often referred to as the photoassociation (PA) of atoms and can result in excited molecular states that are difficult to reach using the ground state molecules by direct excitation. This is true because the selection rules for excitation do not allow to excite a ground state molecule to all the available excited states. These excited state molecules formed from two free atoms as a result of PA, can then be converted to ground state molecules by the use of stimulated emission by a second photon or they can decay quickly to free atoms with increased kinetic energy. Such increased kinetic energies of the atoms can easily overcome the trapping potential holding the atoms and result in the atomic loss from traps<sup>[1]</sup>. The table I below summarizes the single-photon+two-atom processes that often occur when one of the atoms in a pair absorbs a single photon without ionization<sup>[2]</sup>.

## Excitation spectrum and coherent phenomena in 87Rb Bose-Einstein condensates

Table 1. Summary of single-photon+two-atoms (A) processes and their reaction representation. The “\*” represents excited state and the subscript 2 represent the molecular pair of the same atomic species also called Dimer.

No.	Process	Reaction
(i)	bound state to bound state (excitation)	$A_2 + \hbar\omega \rightarrow A_2^*$
(ii)	bound state to free state (dissociation)	$A_2 + \hbar\omega \rightarrow A^* + A$
(iii)	free state to bound state (PA)	$A + A + \hbar\omega \rightarrow A_2^*$
(iv)	free state to free state (inelastic scattering)	$A + A + \hbar\omega \rightarrow A^* + A$

The photoassociation (PA) process is mathematically/symbolically represented by the reaction no. (iii) in Table I<sup>[3]</sup>. The PA process usually locks two free atoms into very loosely bound molecular states having a large inter-nuclear distance and hence this loosely bound pair breaks down into free atoms again very easily. Therefore, the molecular excited states are very short lived. During the time spent in this excited state, the atoms are attracted to each other by the attractive potential (mainly of  $1/R^3$  nature in the  $ns+np$  interactions,  $R$  being the inter-nuclear distance between the two atoms, and  $n$  is the principal quantum number while  $s$  and  $p$  are the angular momentum quantum numbers) and thus they accelerate and starts moving faster towards each other. The acceleration produced in the  $1/R^3$  type potential is the greatest for both of the atoms and it has been experimentally studied in view of the atomic loss from the MOT<sup>[4]</sup>. This detectable loss plotted against the wavelength/frequency of the PA laser gives us the PA spectrum. These attractive potentials are dependent on the inter-nuclear distance  $R$  and therefore the potential vs  $R$  curves are called the potential energy curves (PE curves). The study of these potential energy curves is very important for the understanding of the various constants called the  $C_3$ ,  $C_6$  and higher order term constants, topics which falls under molecular physics and physical chemistry. Also, the permanent electron dipole moment can be measured from the study of dimer molecules<sup>[5]</sup> which is of fundamental interest in the study of fundamental laws of nature (like the standard model). Homo-nuclear and hetero-nuclear diatomic<sup>[6]</sup> or hetero-nuclear triatomic<sup>[7]</sup> molecule formation using Feshbach resonances is also a tool used in ultra-cold atoms but the use of optical tuning offers a much faster switching solution in the form of

PA<sup>[8]</sup> compared to the slower and complex magnetic switching of Feshbach resonance method. Other applications that are directly relevant to the PA spectroscopy are the study of the isotopic effect on the PA rates<sup>[9]</sup>, quantum computing using the ultra-cold molecules inside traps<sup>[10]</sup>, the excitation of free atoms to bound excited molecular states that are not possible to excite easily from ground state molecules due to the selection rules for excitation<sup>[11]</sup>, the tuning of the scattering length of neutral atoms with light<sup>[12, 13]</sup> (often called optical Feshbach resonances), to measure the s-wave scattering length of atoms in the ground state<sup>[14]</sup> and the realization of heteronuclear ultra-cold molecules<sup>[15-19]</sup> and many more.

## 4.2 Photoassociation of atoms in a BEC

The BEC offers an easy way to obtain ultra-cold molecules for studies involving their ground states<sup>[20]</sup>. Phenomena like splitting of the mixed potential energy curves near dissociation limit into their respective hyperfine asymptotes can only be studied at such ultra-cold temperatures<sup>[21-24]</sup> and therefore, we need ultra-cold molecules. But unlike laser cooling of atoms, laser cooling of molecules is not that straight forward as molecules lack the closed cyclic transitions which are necessary for driving the trapping and cooling excitation de-excitation cycles<sup>[25]</sup>. A photon absorbed by the molecule will result in an excitation de-excitation process that will heat the molecule due to the availability of a large number of vibrational and rotational energy levels. The use of a cooling laser for each of the vibrational and rotational level is practically unviable due to the large number of these levels (each vibrational level will need a separate laser frequency to optically pump the electron back to the main transition from this level). Other methods used for cooling molecules directly to lower temperatures could not go below several hundred microKelvins<sup>[26]</sup> or in other cases even millikelvins<sup>[27]</sup>. Therefore, the PA of atoms into molecules from a BEC forms the ideal starting point of achieving the ultra-cold samples of molecules and even of the molecular condensates.

Several PA schemes are being used to create and characterize the ultra-cold molecules in BEC or at non-degenerate temperatures<sup>[26, 28]</sup>. For example, the Production of  $^{87}\text{Rb}$  molecules using PA in a MOT and then detection of the molecules using the selective

mass spectroscopy after two photon ionization is reported in<sup>[29]</sup>. In Ref.<sup>[30]</sup>, the resonance enhanced multiphoton ionization (REMPI) method is used to create and detect the molecular states after ionizing the newly formed molecules via a multiphoton process. Similarly, two-color PA spectroscopy is used to detect dimers in the lower energy molecular states<sup>[31]</sup>. Stark deceleration method has been used to slow down polar molecules only<sup>[32]</sup>. Cold molecules have been observed to form as a result of three-body recombination<sup>[33]</sup> but these do not require any laser light and only need a dense sample of atoms. All of these methods (using light as inducer) use light frequencies that are resonant with vibrational levels of the excited state molecules lying several GHz below their respective fine/hyperfine dissociation thresholds<sup>[34, 35]</sup>. This is because hotter samples of atoms require higher laser powers and the power broadening of these levels caused by the high power PA lasers limits us from going any further near to the dissociation limit due to the probability of exciting atomic transitions. The use of large detuning wavelengths also makes it difficult to control the wavelength of the laser precisely and uncertainty in the actual resonance position of the molecular excited state is large<sup>[21, 36]</sup>. In this thesis, I present the PA very near to the photoassociation threshold of the D1 line (within  $\pm 1$  GHz of the D1 hyperfine asymptotes) with very fine control over the frequency scanning of the PA laser and exploit the sub-KHz thermal broadening environment of the BEC to study the weakly bound narrowly spaced excited states of  $^{87}\text{Rb}$  dimers. The high density offered by the BEC also helps in the high PA rate with the use of even weaker PA laser light<sup>[37, 38]</sup>, thus avoiding the light induced shifts in the actual positions of the PA resonances.

### 4.3 Photoassociation threshold and asymptotic potentials

As discussed above, the pair of atoms in which one of the atoms is in the excited state  $5P$  and one in the ground state  $5S$  will attract each other. This potential is highly dependent on the distance  $R$  between the nuclei of the two atoms. It can be represented as a multipole expansion of the potential in terms of  $R$

$$V(R) = D_e + \sum_n \frac{C_n}{R^n} \quad (4.1)$$

## Chapter 4: Photoassociation of the $^{87}\text{Rb}$ BEC near the D1 line threshold

where  $D_e$  is the dissociation energy of the potential (atoms having a combined kinetic energy of  $D_e$  will not experience the potential of 4.1 no matter how near they are to each other),  $n$  is the order of the potential term and  $C$  is the constant of the corresponding order. Odd values of  $n$  comes from first order perturbation theory and even values from second order perturbation. A pair of atom in which one atom is in the S ground state ( $5s$ ) and the other is excited near the P excited state ( $5p$ ) will experience a  $n=3$  type of potential (dipole-dipole interaction between such a pair of atoms) while a pair with  $n=5$  type of potential will arise from the quadrupole-quadrupole coupling between them. Odd  $n$  value potentials exists between permanent multipoles while even  $n$  value potentials arise due to induced multipoles. For example, the  $n=6$  represents the Van Der Waals potential between the induced dipoles and the  $n=8$  represents the coupling between the induced quadrupoles and so on.

The behavior of this kind of potential (Eq. 4.1) is asymptotic in nature and holds only for large values of  $R$ . It fails for small  $R$  values of less than  $20 \text{ \AA}^{0 [39]}$  or when the Coulomb interaction energy and the hyperfine interaction energy becomes comparable (this occurs at around  $0.2 \text{ cm}^{-1}$  (or  $149.9 \text{ GHz}$ ) from the dissociation limit at a very large  $R$  value of  $> 148 \text{ \AA}^0$  for  $^{87}\text{Rb}$ ). At very large  $R$ , the hyperfine interaction outweighs the  $R$  dependent form of the potential and Eq. 4.1 needs modification. The PA spectra presented in this work belongs to the  $5S+5P$  potentials (mainly to the  $n=3$  potential, which is the most long range of all these potentials, but strongly affected by the hyperfine interactions) and it is very important for the exact knowledge of the constants  $C_n$  near the hyperfine asymptotes of  $5S+5P$ . Some of these potentials (PE curves) are shown schematically (not to scale) in Fig. 4.4 with the observed PA spectrum (horizontal lines connected to the PE curves). This thesis does not present any theoretical calculations of the spectra presented in this thesis and all these lines connecting to the PE curves in the Fig. 4.4 are for explanation purpose only. Only exact and careful numerical calculations can suggest the actual PE curve for a particular PA line. However, a brief commentary is presented based on the behavior of the observed lines near the dissociation asymptotes.

#### 4.4 Photoassociation of $^{87}\text{Rb}$ near the D1 line threshold

Previous studies on the PA of  $^{87}\text{Rb}$  were either done with extremely far detuned PA wavelengths or were unable to find any quantized resonances in the  $\pm 1$  GHz range of the D1 line of  $^{87}\text{Rb}$ <sup>[35, 36]</sup>. The reasons, as described above are the use of hot atomic vapors and the use of high power and free running mode (not locked) lasers with very coarse frequency tuning, which washed out any PA resonances hiding in the continuous loss spectrum detected in the previous works. The use of the  $^{87}\text{Rb}$  BEC and a finely tunable laser at low power remove these obstacles in the detection of these resonances. The photoassociation spectra is recorded within  $\pm 1$  GHz of the  $5^2\text{P}_{1/2}$  dissociation limit. This dissociation limit corresponds to the frequency position in the PA spectra when one atom is in one of the 5S states and the other atom is excited to near (above or below) an atomic resonant hyperfine state of the  $5^2\text{P}_{1/2}$  state. The general nomenclature for this region of PA is the 5S+5P near threshold spectra. Two sets of PA spectra are presented, one for atoms prepared in the  $|F=1, m_f=1\rangle$  hyperfine state of the  $^{87}\text{Rb}$  atomic ground state and the other for the atoms prepared in the  $|F=2, m_f=2\rangle$  hyperfine state of the  $^{87}\text{Rb}$  atomic ground state.

##### 4.4.1 Experimental Setup and experimental procedure

The experimental sketch of the PA part is shown schematically in Fig. 3.1. The experimental sequence starts from the production of  $^{87}\text{Rb}$  BEC in a crossed optical dipole trap whose trapping frequencies are  $\bar{\omega} \approx 2\pi \times 80$  Hz. Initially the atoms are prepared in the  $|F=2, m_f=2\rangle$  hyperfine ground state but these can be transferred to the  $|F=1, m_f=1\rangle$  hyperfine state using a microwave (MW) pulse (adiabatically turned ON and scanned) at around 6835 MHz in the presence of a vertical magnetic field of 2 G. If we need atoms in the lower hyperfine state, the MW transfer of atoms to the  $|F=1, m_f=1\rangle$  hyperfine state takes place immediately after the preparation of the BEC in the  $|F=2, m_f=2\rangle$  hyperfine state, as described in Chapter 2. After preparation of the atoms in either of the hyperfine states, the experimental laser beams illuminate the atoms for 20  $\mu\text{s}$  inside the dipole trap. The number of the experimental laser beams depends on which technique is being used for the collection of the spectral data. The coupling and probe (PA) laser beams are from the same setup that we used in Fig. 3.2 for the realization of the N-type scheme (same setup without the driving laser).



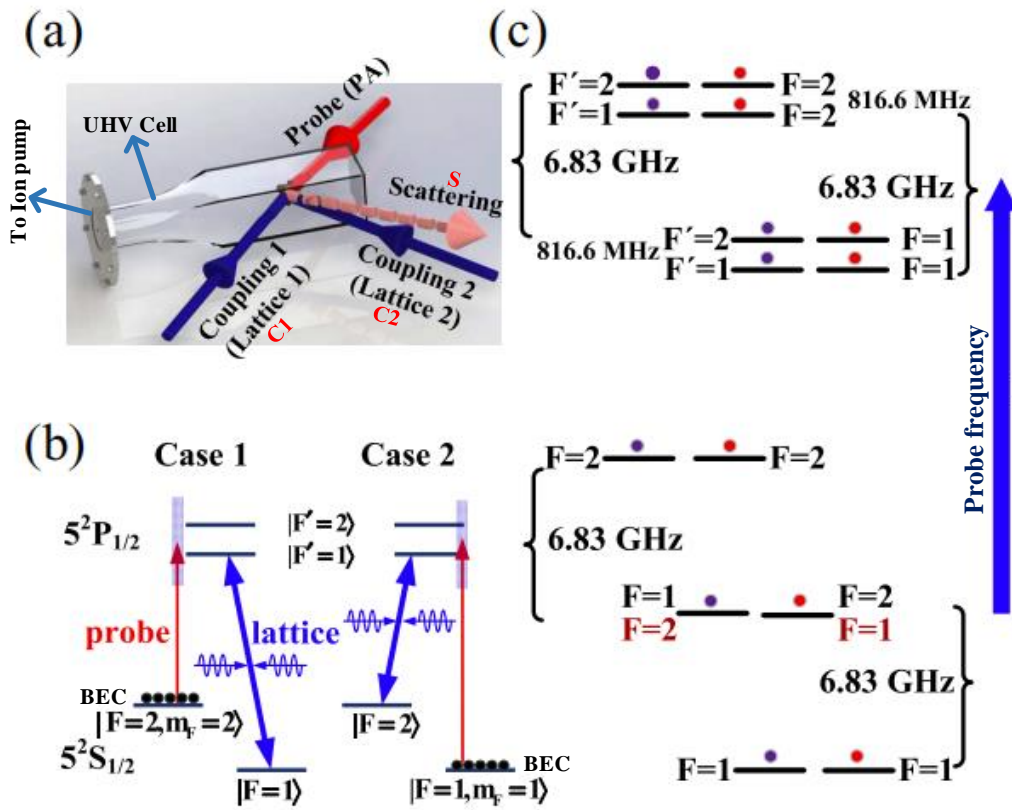


Figure 4.1. This Fig. shows the experimental schematic, the two cases of spectra and the energy level diagram of the different combinations of the hyperfine energy levels of two  $^{87}\text{Rb}$  atoms. (a) The experimental laser beams in the plane of the paper illuminating the BEC inside the ultra-high vacuum (UHV) cell from different angles. The probe (PA) beam and the Bragg scattered light (call it S) make an angle of  $132^\circ$  with each other. The two coupling beams coupling 1 and coupling 2 (call them C1 and C2) makes an angle of  $48^\circ$  in the plane of the paper. The PA and Bragg scattered beams make an angle of  $11^\circ$  with the plane of the paper in the normal direction. The imaging laser is along the normal to the plane of paper and is not shown. (b) The potential/internal energy of a two atom system in different configurations of the hyperfine energy levels. The spacing is not to scale. The atomic pairs in each shelf represent the dissociation limit/threshold point for many potential energy curves. (c) The locking schemes of the coupling and probe lasers for the two cases of the PA spectra.

Two techniques are used in this work to record the PA spectra. One is the conventional trap loss or absorption imaging technique in which just a single probe (PA) laser is used to illuminate the BEC/atoms after its preparation. The atoms will interact with the PA laser

## Excitation spectrum and coherent phenomena in $^{87}\text{Rb}$ Bose-Einstein condensates

light for 20  $\mu\text{s}$  inside the dipole trap and then the dipole trap and the PA lasers are turned OFF. The atoms in the BEC will respond differently to the probe (PA) laser depending on its frequency during each exposure. At the PA resonance points, the atoms will attract each other and accelerate and then break away from the momentary attractive bond (the bound state will decay) and leave the weak dipole trap due to increased kinetic energy. Thus there will be detectable loss at the resonance PA frequencies only. After each exposure, the atoms are then left to ballistically expand under the action of gravity (outside the dipole trap) and after 30 ms of free fall another laser (absorption imaging laser) takes a picture of the remaining atoms in the now expanded cloud of atoms and a software processes the absorption images to extract the number of remaining atoms. This process is repeated for each probe (PA) laser frequency and each point starts with a fresh sample of the BEC. A single spectrum covering both sides of each of the D1 line hyperfine level consists of several hundred points of probe (PA) laser frequency and thus needs more than a thousand times of experimental runs when each point is recorded three times (each run takes around 50 seconds including MOT loading). This is how the trap loss/absorption imaging technique spectra are obtained. The data acquisition time is very long because the number of spectral points is too large and thus temperature variations may alter the laser power levels in the whole setup, and therefore, it is important to check the powers of all the lasers and the number of atoms in the BEC after every couple of hours to keep the data consistent.

The second technique is the Bragg scattering technique in which the experimental laser beams consist of three beams. One of the beams is the probe (PA) laser that does the PA. The other two beams C1 and C2 are the lattice beams (that we call the coupling beams due to conventional terminology used in electromagnetically induced transparency and other atomic coherence experiments as discussed in Chapter 3). These two beams C1 and C2 are derived from the same laser. The coupling laser and the probe (PA) laser are locked to each other in the master-slave relationship by the OPLL (as shown in Fig. 3.2 in Chapter 3) and the master laser is further locked by the SAS for its frequency stabilization. The two coupling beams C1 and C2 intersect each other at the BEC position making an angle of  $48^\circ$ . Both of the coupling beams are polarized in the same direction (along the normal of the paper) and thus interfere at the BEC position. The BEC will be out-coupled by these

coupling beams into a ground state modulated lattice. This lattice, holding  $^{87}\text{Rb}$  atoms in the ground state, will absorb the probe laser and then re-emit or scatter it in the special direction, shown in Fig. 4.1(a). The probe (PA) laser makes an angle of  $132^\circ$  with the Bragg scattered light S. The Bragg scattered light is highly directional due to the four wave mixing phenomenon and the conservation of linear momentum of all the participating beams<sup>[40-42]</sup>. The scattered light is then collected by a lens and is directed into the EMCCD camera by a mirror. This total process of BEC illumination by the experimental beams and the collection of the scattered light by the EMCCD is completed in the  $20 \mu\text{s}$  time. Both the illumination of the BEC by the coupling and probe (PA) lasers and the light collection by the EMCCD is simultaneous and does not need the 30 ms of expansion. This process is repeated for each probe (PA) laser frequency in the same manner as for the trap loss method.

#### 4.4.2 The PA spectra

The BEC is prepared in two different spin states of the  $5^2\text{S}_{1/2}$  ground state. When the  $^{87}\text{Rb}$  BEC is prepared in the  $|F=2, m_f=2\rangle$  hyperfine state then we call the PA spectrum as the Case 1 spectrum. Fig. 4.2 shows the Case 1 spectrum recorded via the Bragg scattering technique.

When the  $^{87}\text{Rb}$  BEC is prepared in the  $|F=1, m_f=1\rangle$  hyperfine state then we call the PA spectrum as the Case 2 spectrum. This spectrum needs the BEC to be first transferred to the  $|F=1, m_f=1\rangle$  hyperfine state and then should be exposed to the experimental laser beams. Fig. 4.3 shows the Case 2 spectrum recorded via the Bragg scattering technique. The PA spectra of the two cases are different as both arise from different potential energy curves.

Another worth-mentioning point about the absorption imaging vs Bragg scattering technique is that the absorption imaging/trap loss technique does not need the coupling lasers and only the locking scheme for probe laser need to change, but the Bragg scattering technique requires different locking schemes for the coupling and probe lasers for Case 1 and Case 2, as discussed below.

#### 4.4.3 Laser locking schemes for the Case 1 and Case 2 spectra

For the Case 1 spectrum using the Bragg scattering technique, atoms are prepared in the  $|F=2, m_f=2\rangle$  hyperfine state and the probe (PA) laser photoassociate the atoms from this state to the excited molecular states below or above the two D1 line excited hyperfine

## Excitation spectrum and coherent phenomena in $^{87}\text{Rb}$ Bose-Einstein condensates

states ( $|F'=1\rangle$  and  $|F'=2\rangle$ ). The coupling laser is locked between the  $|F=1\rangle$  hyperfine state and any of the excited hyperfine states  $|F'=1\rangle$  or  $|F'=2\rangle$  so that the atoms are not heated by the coupling laser and are only loaded into the optical lattice formed by the two coupling laser beams.

Similarly, for Case 2 spectrum using the Bragg scattering technique, the atoms are prepared in the  $|F=1, mf=1\rangle$  hyperfine state and the probe (PA) laser photoassociate the atoms from this state to the excited molecular states below or above the two D1 line excited hyperfine states. The coupling laser is locked between the  $|F=2\rangle$  hyperfine state and any of the excited hyperfine states  $|F'=1\rangle$  or  $|F'=2\rangle$  again only loading the atoms into the optical lattice formed by the interference of the two coupling beams. The atoms in the lattice then Bragg diffract the light in the special direction which is modulated by the presence of the PA resonances. The light diffracted is directly proportional to the number of atoms present in the lattice and when there is a PA resonance, the PA process will lead to the escape of atoms from the trap and the lattice and thus the Bragg diffraction will be reduced. This reduction of the diffracted light intensity is significant enough (high resolution) and thus all the PA resonances are easily revealed by the Bragg diffraction method.

### 4.4.4 Discussion on the spectra

The different regions of each spectrum are discussed in the following. The frequency scanning step of the probe (PA) laser was kept at 0.2 MHz in the vicinity of the resonance and thus the uncertainty in the positions of the resonances is not larger than 0.2 MHz as the OPLL system keeps the frequency oscillations in the probe (PA) laser to within a few Hz. Fig. 4.2 shows the Case 1 spectrum and Fig. 4.3 shows the Case 2 spectrum using the Bragg scattering technique. Fig. 4.4 combines both the Case 1 and Case 2 spectra in one place and the possible association of the PA lines to the potential energy curves (PE curves) is also shown in the right panel of the same figure. The exact association of these lines however, requires the complete theoretical fitting of each PE curve to the data presented here and I only discuss the possible association of the PA resonances from the general properties of the data lines e.g. the behavior of the density of the line with detuning with respect to a specific threshold point.

**Case 1:** Fig. 4.2(a) shows the Case 1 spectrum recorded using the Bragg scattering technique. The coupling laser is locked from the lower ground hyperfine level  $|F=1\rangle$  to the excited hyperfine level  $|F'=2\rangle$ . The Bragg scattering intensity coming from the atoms in the  $|F=2, mf=2\rangle$  hyperfine state is modulated by the PA resonances. The PA resonance results in loss of atoms from the BEC and hence in the scattering intensity of the Bragg scattering thus each PA resonance corresponds to the reduced scattering in the Fig. 4.2. Figures 4.2(b-d) shows the zoomed-in portions of the same Fig. 4.2(a), also marked by the numeric labels. These regions exclude the atomic resonance transition peaks which are discussed separately in the dissociation limits/threshold points section later. The numerically labeled regions are discussed below.

**Region 1:** This region lies above the upper hyperfine threshold point (in the energy diagram of Fig. 4.1, this threshold point is the highest shelf) where one atom is in the  $|F=2\rangle$  hyperfine state and the other atom is excited to the blue detuned side of the  $|F'=2\rangle$  hyperfine state. Since this region lies above the classical threshold point of the potential energy curve, there are no PA resonances in this region<sup>[43]</sup> as the energy of the atoms is higher than these PE curves can trap.

**Region 2:** This region lies between the  $|F'=1\rangle$  and the  $|F'=2\rangle$  hyperfine state. All of the PA resonances belong to the potential energy curve belonging to the  $|F'=2\rangle$  hyperfine state threshold and that is why this region shows a  $1/R^3$  character (also called the  $n=3$  character of the potential energy curve). The  $1/R^3$  character is characterized by the decreasing spacing (increasing line density) as the threshold point is approached, in an orderly manner<sup>[44]</sup>. However, as stated in the above sections, there is also a strong coupling resulting from the hyperfine levels of the D1 line and thus the PA lines are not strictly following the  $1/R^3$  character alone. Again, a detailed theoretical investigation is needed to fit all the lines in this region to accurately assign a particular PA line to its actual PE curve.

**Region 3:** This region lies below both of the two excited hyperfine states of the D1 line and thus it is possible that the PA resonances belonging to both the potential energy curves terminating on the  $|F'=1\rangle$  and the  $|F'=2\rangle$  hyperfine states might be present in this region. That is why the PA resonances in this region do not show the regular pattern that we see in the region 2. The various potential energy curves mix (i.e. the PA resonances detected in

## Excitation spectrum and coherent phenomena in $^{87}\text{Rb}$ Bose-Einstein condensates

this region are found mixed with each other) and splits just before their respective hyperfine thresholds are reached. So the irregular shape of these PA resonances in this region might be due to the mixing of the potential energy curves terminating on the  $|F'=1\rangle$  and the  $|F'=2\rangle$  but the exact detail can be only found by the accurate theoretical modeling of the potential energy curves (which can be done in the future work). The scanning range of the OPLL system below the resonance and the low amount of scattered intensity put a limit on the number of PA lines that we could detect in this region of the PA spectrum.

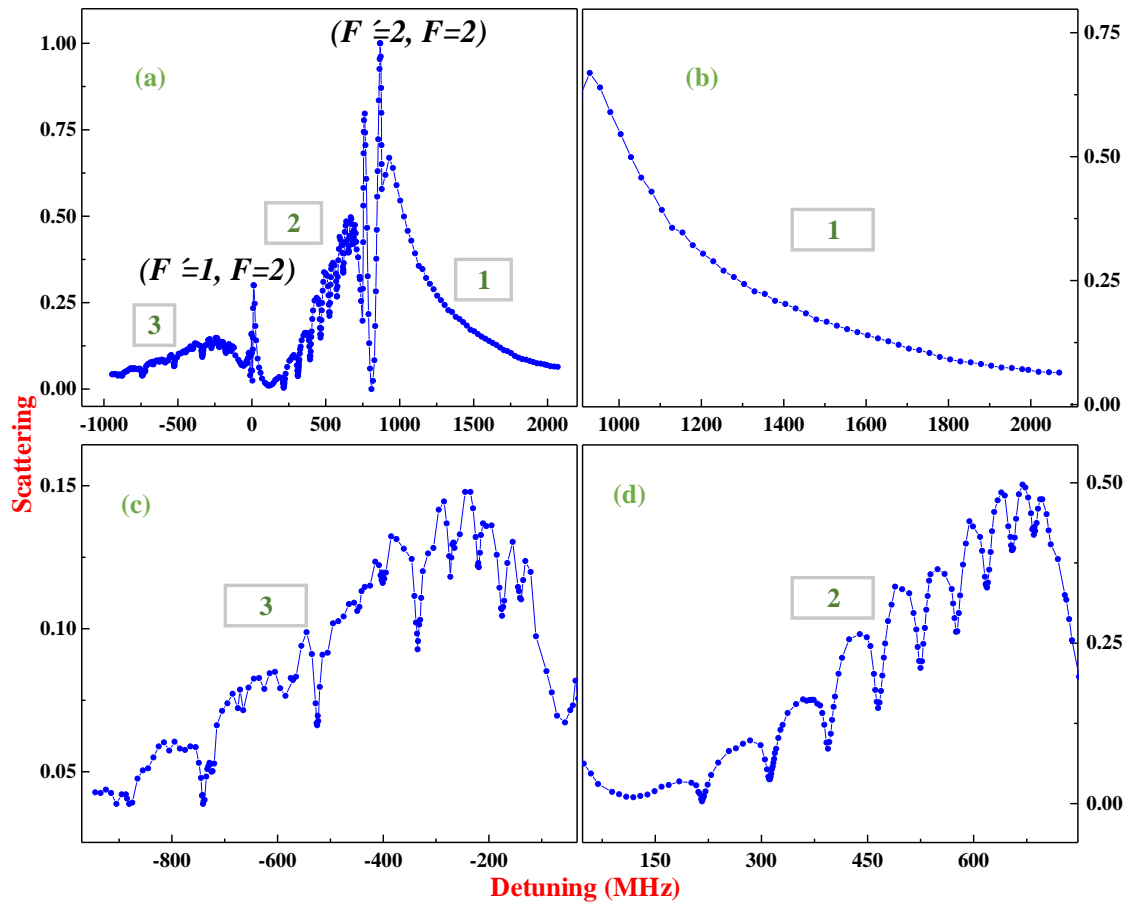


Figure 4.2. This Fig. shows the Case 1 spectrum recorded using the Bragg scattering technique. The numerical labels 1-3 show the regions above and below the threshold points marked by the respective hyperfine states of the two atom pair. The zero detuning is the frequency corresponding to one atom in the pair in the excited state  $F'=1$  state and the other atom in the  $F=2$  ground state. This is the first threshold point in the Case 1 spectrum. All the other detuning are measured with respect to this point.

**Threshold points/Dissociation limits:** Fig. 4.2(a) shows the two  $|F'=1\rangle$  and the  $|F'=2\rangle$  threshold points or the dissociation limits situated at 0 MHz and 814 MHz respectively. These are the atomic resonance points of the D1 line and do not have any PA resonances at these frequencies. Two small (only one clearly visible in Fig. 4.2(a)) peaks at 0 MHz correspond to the atomic resonance Bragg scattering. At this atomic resonance, the Bragg scattering increases due to the modulation of the atomic medium for the probe frequencies in this region. The peaks are due to the increased reflection of the probe (PA) light from the ground state modulated BEC in the optical lattice<sup>[45]</sup>. The two bigger peaks (with sharp dips

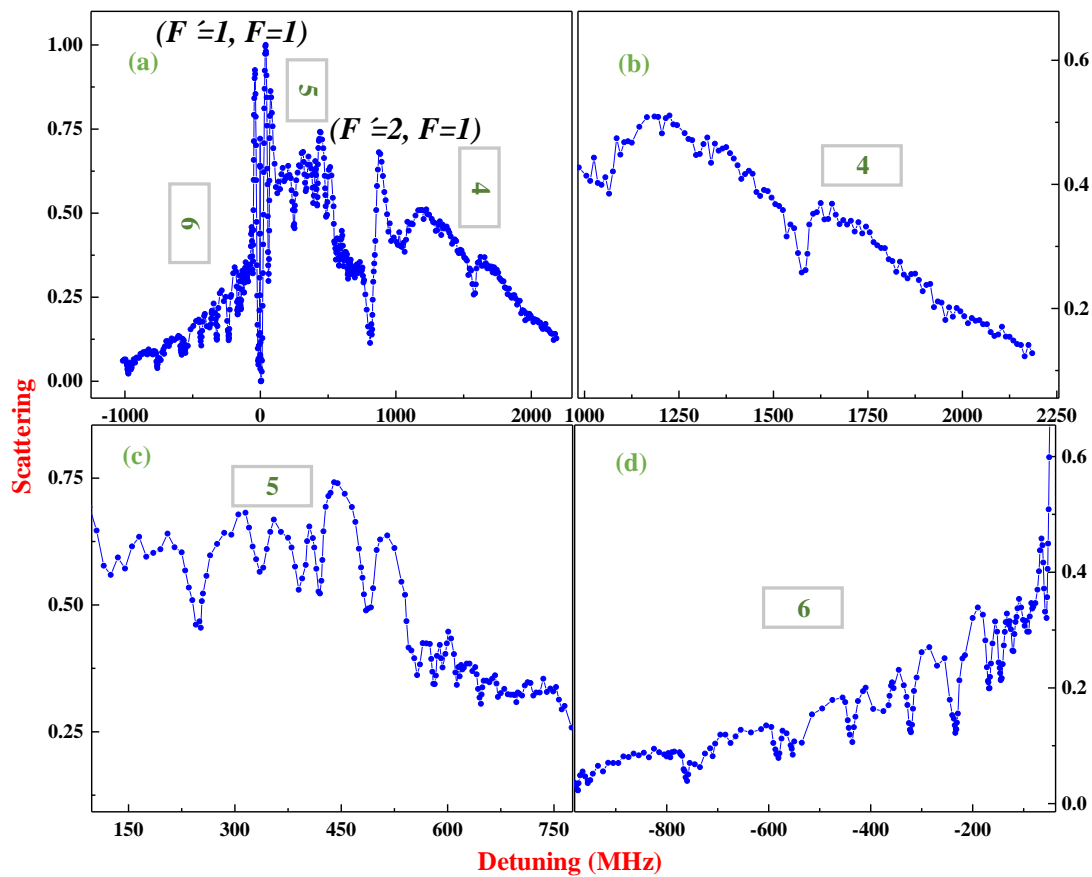


Figure 4.3. This Fig. shows the Case 2 spectrum recorded via the Bragg scattering technique. The numeric labels 4-6 show the regions above and below the threshold points marked by the respective hyperfine states of the two atom pair. The zero detuning is the frequency corresponding to one atom in the pair in the excited state  $F'=1$  state and the other atom in the  $F=1$  ground state. This is the first threshold point in the Case 2 spectrum. All the other detuning are measured with respect to this point.

on both sides and between) at 814 MHz correspond to the superradiance scattering peaks that result from the superradiance lattice which is composed of alternate excited and ground state lattices. The excited state lattice component of the superradiance lattice resembles the electromagnetically induced transparency spectrum in a lambda-type system. This lattice is formed when the coupling laser and probe (PA) laser are connected to the same excited state but to different ground states (lambda-type system)<sup>[40, 42]</sup>. These peaks are the most dominant features in all the other spectrum but they do not have any effect on the position of the PA resonances as the PA resonances modulate only the non-resonant Bragg scattering region of the Bragg scattered light. More about superradiance lattice in the next chapter.

**Case 2:** The atoms are in the  $|F=1, mf=1\rangle$  state and the probe (PA) laser couples them to the PA resonances above and below the two D1 line excited hyperfine states. The coupling laser is locked from the upper ground hyperfine state  $|F=2\rangle$  and the excited hyperfine state  $|F'=1\rangle$  (however it can also be locked between the  $|F=2\rangle$  and the excited hyperfine state  $|F'=2\rangle$  without any noticeable effect on the position of the PA lines). The PA spectrum for Case 2 is shown in Fig. 4.3(a). Figures 4.3(b-d) show the zoomed in regions of Fig. 4.3(a) marked by the numeric labels 4-6. The PA resonances are present in the spectrum in the form of reduced Bragg scattered intensity due to loss of atoms from the  $|F=1, mf=1\rangle$  state due to PA. The different regions are discussed below.

**Region 4:** This region lies above the  $|F'=2\rangle$  state dissociation limit and there should be no PA bond states at this range of blue detuning<sup>[43]</sup>. Although there are some predictions for the possibility of PA resonance above the D2 line highest threshold<sup>[25]</sup> but no theoretical work (so far in our knowledge) has predicted the existence of a PA resonance in this region. But in our data, there is one PA resonance (which we will also see in the trap loss spectrum below) located at around 1580 MHz above the  $|F'=1\rangle$  state (around 766 MHz above the  $|F'=2\rangle$  state). This state may belong to the higher lying potential energy curves terminating at higher lying dissociation limits (may belong to one of the dissociation limits lying above the dissociation limit of  $(|F=1\rangle, |F'=2\rangle)$  in Fig. 4.1(b)). The schematic representation of the PA lines and their possible association with each potential energy (PE) curve is shown in Fig. 4.4.



**Region 5:** This region lies between the lower hyperfine excited state  $|F'=1\rangle$  and the upper hyperfine excited state  $|F'=2\rangle$ . This region should be similar to the region 2 of Case 1 spectrum in the behavior of variation of PA lines density as all the PA resonances in this region belong to the single potential energy curve terminating at the  $|F'=2\rangle$  state ( $|F=1\rangle, |F'=2\rangle$ ) dissociation limit in the shelf diagram of Fig. 4.1(b)). This  $1/R^3$  potential kind of behavior is visible in the right most corner of Fig. 4.3(c) but the left side does not show similar behavior as it has irregular PA line density. This could be due to the presence of another potential energy curve mixing with the one terminating at the  $|F'=2\rangle$  state (may be the resonance in region 4 also belong to that potential energy curve which mixes with the curve terminating on  $|F'=2\rangle$  state thus bringing irregularity to the PA resonance lines in region 5). Another important aspect of this region is the right corner of this region (Fig. 4.3(c)) which shows phenomenally reduced scattering. This is due to the strong mixing of the PA resonances with the atomic resonance. The atomic resonance in this region is broadened so much that its Lorentzian shape is destroyed (more discussion in the following sections).

**Region 6:** This region lies below the lower excited state  $|F'=1\rangle$  state. This region also does not show a very regular ordering of the PA lines although near the dissociation limit of  $|F'=1\rangle$  state the lines density increases similarly to how a  $1/R^3$  (or any converging) potential might suggest. The slight irregularity in the PA lines density suggests the mixing of the potential energy curve terminating at  $|F'=2\rangle$  state (or any higher lying potential energy curves).

**Threshold points/Dissociation limits:** The two threshold points are situated at 0 MHz corresponding to the  $|F'=1\rangle$  state atomic resonance and at 814 MHz corresponding to the  $|F'=2\rangle$  state atomic resonance. In this spectrum, the coupling laser is locked from the  $|F=2\rangle$  state to the  $|F'=1\rangle$  state so when the probe (PA) laser is in resonance with the  $|F'=1\rangle$  state then we get a lambda type electromagnetically induce transparency system and thus the lattice formed by the coupling and probe (PA) lasers acts as superradiance lattice and the two intensity peaks at the atomic resonance are bigger compared to the peak at the  $|F'=2\rangle$  state atomic resonance which now behaves as a resonant Bragg resonant peak. If we lock the coupling laser from  $|F=2\rangle$  state to  $|F'=2\rangle$  state then the peak at  $|F'=2\rangle$  will become

## Excitation spectrum and coherent phenomena in $^{87}\text{Rb}$ Bose-Einstein condensates

superradiance peak and the  $|F'=1\rangle$  state peak would become resonant Bragg scattering. But the locking scheme for the coupling laser does not affect the locations of the PA resonances as they are situated in the non-resonant Bragg scattering regions (away from the atomic resonance). Fig. 4.5 shows the effect of the locking scheme of the coupling laser on the resonant atomic scattering peaks (one at  $|F'=1\rangle$  one at  $|F'=2\rangle$ ).

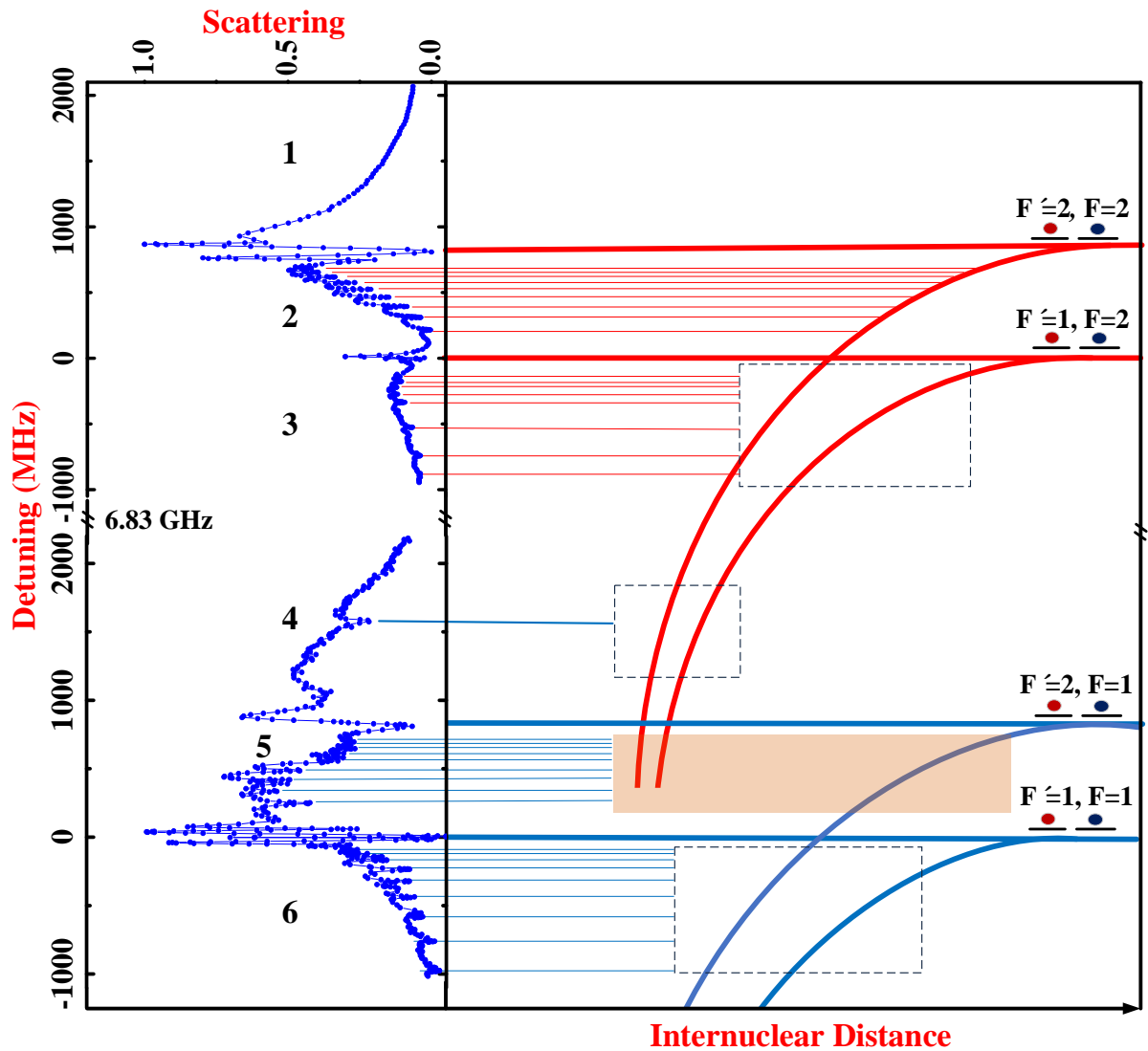


Figure 4.4. The schematic representation of the PA resonances (left panel) and their possible association with the PE curves (in the right panel). The dashed boxes shows the possibility of the belonging of each resonance line with any of the PE curves in the box.

#### 4.4.5 Trap loss spectra and its comparison to the Bragg scattering spectra

The trap loss/absorption spectra is shown in Fig. 4.6 for both Case 1 and Case 2. The PA resonances shown in Figures 4. 2 and 4.3 are all present in the trap loss spectra as well. The trap loss spectra are the direct measure of the atoms remaining in the atomic cloud after the exposure to the single experimental laser beam (the PA laser). But it is noisier compared to the Bragg scattering spectra (also see the RMSD and RMSDA values in Table I for noise comparison).

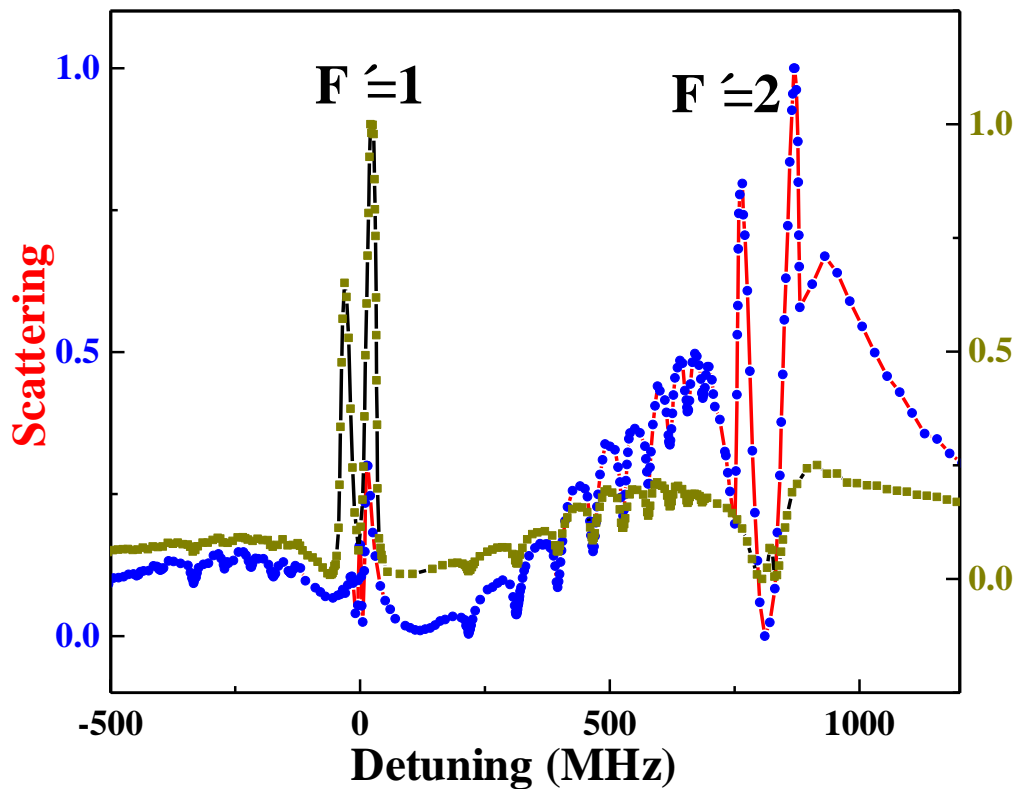


Figure 4.5. The effect of the locking scheme for the coupling laser on the height of the atomic resonance peaks. Both of the spectra are the Case 1 spectra. In the blue (open boxes) spectrum, the coupling laser is locked from the  $|F=1\rangle$  to the  $|F \simeq 2\rangle$  state, so the atomic resonance peaks at  $|F \simeq 2\rangle$  are the superradiance peaks and the ones at the  $|F \simeq 1\rangle$  are the (smaller) resonant Bragg scattering peaks. In the dark yellow (circles) spectrum, the same laser is locked from the  $|F=1\rangle$  to the  $|F \simeq 1\rangle$  state, so the atomic resonance peaks at  $|F \simeq 1\rangle$  are the superradiance peaks and the ones at the  $|F \simeq 2\rangle$  smaller resonant Bragg scattering peaks. All of the remaining regions of the spectrum represent the non-resonant Bragg scattering in both locking schemes.

# Excitation spectrum and coherent phenomena in $^{87}\text{Rb}$ Bose-Einstein condensates

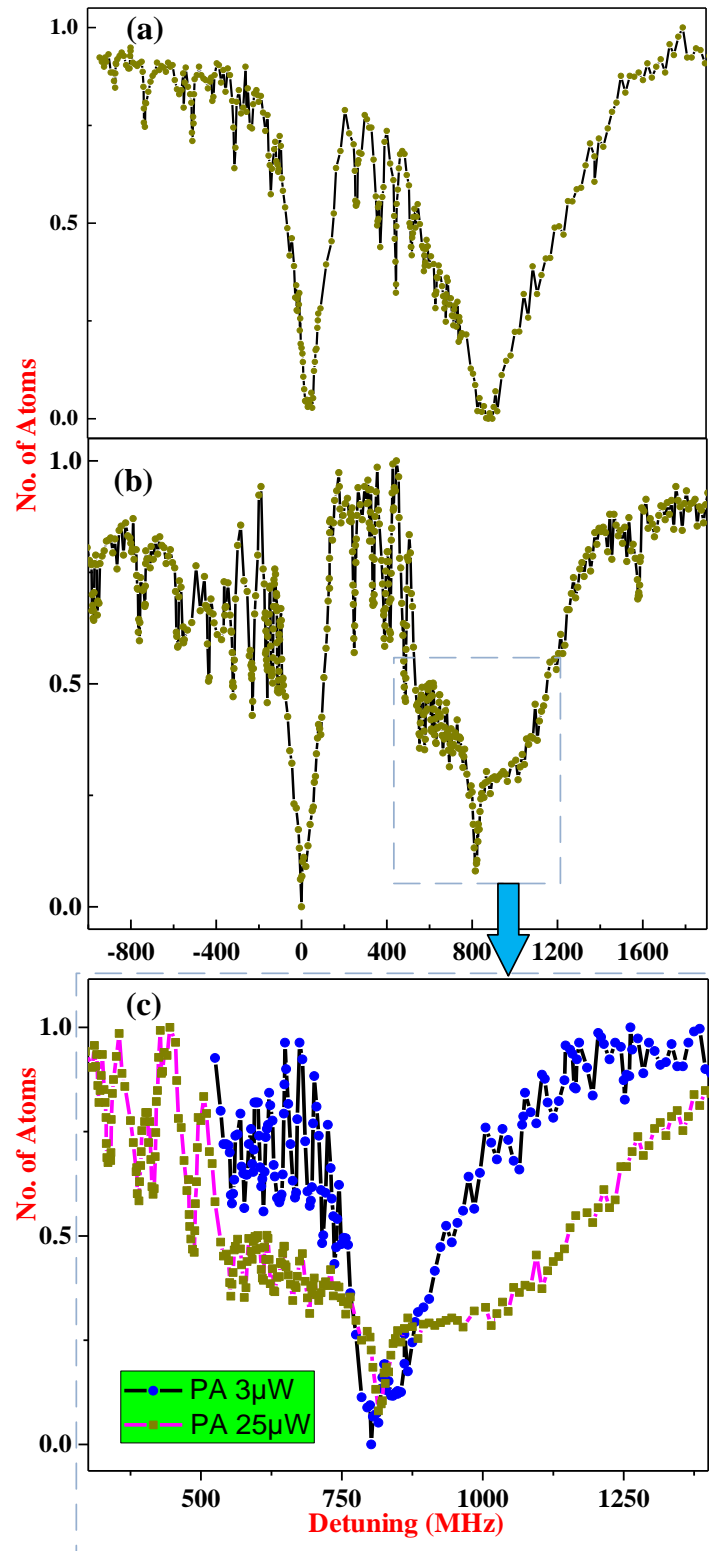


Figure 4.6. (a) Case 1 trap loss spectrum. (b) Case 2 trap loss spectrum. (c) The zoomed in part of the Case 2 spectrum at two different PA laser powers. The Lorentzian shape is restored when the PA laser power is reduced.

The noisiness of the absorption imaging/trap loss spectra can be due to several reasons. For example, the absorption imaging technique uses the three absorption images (one of the atoms, one of the imaging probe laser and one of the dark background) and then subtract these images from each other to extract the number of remaining atoms. During these three images, fluctuations in the imaging laser power and also the low frequency vibration of the imaging optics will introduce interference fringes which the data extraction algorithms cannot recognize, and thus adds to the noise in each experimental run<sup>[46]</sup>. Other reasons include the interaction of the atoms with the environment (background) between the exposure to the experimental beam and the imaging step. The Bragg scattering spectrum is collected live during the exposure (in-situ) and that is why these noise adding steps are avoided. Also, the absorption imaging technique involves the extra statistical noise step of absorption imaging light interacting with the atoms for taking the image while the Bragg scattering technique does not have any such step. Although this noise could be small but it is always present. Another reason is that the Bragg scattering signal scatters more light when the absorption is strong (absorption at other than PA resonances scatters more light as there is less atomic loss at the non-resonant frequencies. Atoms would still be heated and lost but not like when the PA resonance has arrived). On the other hand in the absorption imaging technique, the number of remaining atoms is reduced too much due to strong absorption of light near the atomic resonance. The small number of atoms remaining will result in reduced signal while the noise levels are still the same and thus the signal to noise ratio will be severely reduced. That is why the Bragg scattering technique shows less noise or higher signal to noise ratio. The comparison of the PA resonance positions from the two techniques shows that both of these techniques can detect these excited state molecular resonances but that the Bragg scattering scheme has a better signal-to-noise ratio. For comparison, the values of the PA resonance positions recorded by both techniques are given in Table I.

### 4.4.6 Anomalous broadening of the upper excited hyperfine transition

Another interesting finding from the data is the anomalous broadening of the  $|F'=2\rangle$  atomic resonance line. Fig. 4.6(c) shows the strong and anomalous broadening of the  $|F'=2\rangle$  atomic resonance that is extended to several hundreds of MHz in width. The PA lines here

strongly couple to the atomic resonance and distorts the Lorentzian shape, which is expected from any typical atomic resonance curve. For comparison, the  $|F'=1\rangle$  resonance is not distorted at the same probe (PA) laser power to such a degree. By reducing the PA laser power the typical Lorentzian line-shape is restored back suggesting the involvement of the PA lines broadening in the distortion of the atomic resonance shape. This is because the availability of more PA laser power couples more states from the continuum into the bound molecular states. The anomalously strong Franck-Condon factors of the PA states in this region couples more continuum states into the bound states compared to the PA states in the other regions and thus causes larger PA line broadening and thus distorting the  $|F'=2\rangle$  state atomic resonance. Reduction of the PA laser power removes some of the continuum states from the coupling to the PA lines and hence not only the PA lines broadening is reduced but the atomic resonance Lorentzian shape is restored. This finding is very important for the use of this atomic state in atomic coherence experiments like the EIT, EIA etc. as the atomic coherence effects in this region can be affected by the strong coupling of the PA lines when using high power coupling/driving lasers.

### 4.4.7 Red shift of the PA lines due to increase in power

In Fig. 4.7 the effect of the PA laser power is shown on the positions of some of the PA lines. Most of the PA lines reported in the literature shift towards the red side of PA laser frequency with increasing PA laser power<sup>[47-49]</sup>. The amount of shift for every line is not the same as each line's Franck-Condon factors are different. The exposure time was kept the same 20  $\mu$ s while the PA laser power was increased to record the Fig.4.7 data. The total fluence (defined as intensity  $\times$  pulse width of the PA laser) was thus not the same and this resulted in the broadening of the high power data as well as in shift of the lines. Extra broadening can be avoided by reducing the exposure time so that the product of time and laser intensity remains the same for different power and exposure time. But this was not our goal as we also wanted to see the broadening of the lines. The PA bound state line at 576 MHz (not shown in Fig. 4.7) observed at 25  $\mu$ W of PA laser power, shifts to 571 MHz at 100  $\mu$ W, and then to 557 MHz at 300  $\mu$ W. Similarly, the line at 525 MHz at 25  $\mu$ W of PA laser power, moves to 521 MHz at 100  $\mu$ W, and to 510 MHz at 300  $\mu$ W. This means that

the 576 MHz line shifts by about 19 MHz for a PA laser power change of 275  $\mu\text{W}$  compared to the 15 MHz shift in the position of the line at 525 MHz.

The total Case 1 and Case 2 spectra is tabulated in Table II below for a probe (PA) laser power of 25  $\mu\text{W}$ . Only those PA lines which are present in both the Bragg scattering technique and the trap loss technique are listed along with the root-mean-squared-deviation (RMSD) values. The RMSD value for the Bragg scattering technique is represented by the RMSDS label while that of the trap loss technique is represented by the RMSDA label. Delta is the difference (in MHz) between the position of the trap loss technique position of the PA line and the Bragg scattering technique position of the PA line. All the detuning of the probe(PA) laser reported in the table are measured from the lower excited hyperfine level of the D1 line.

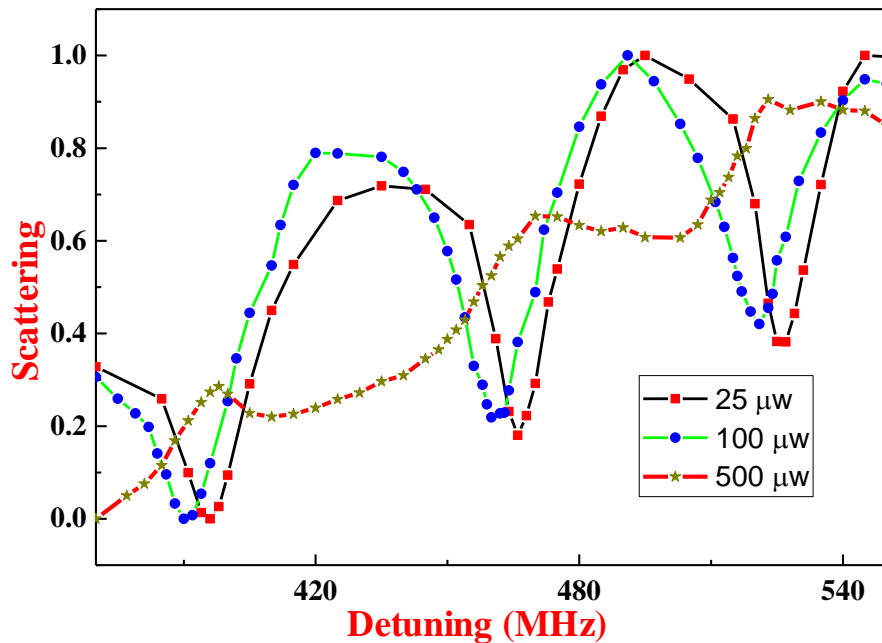


Figure 4.7. The redshift in the PA lines due to increase in PA power. The PA lines shift to the red side of the spectrum which is a common feature of the PA lines. The broadening of the lines with the laser power is also visible.

## Excitation spectrum and coherent phenomena in $^{87}\text{Rb}$ Bose-Einstein condensates

Table II: The table shows the positions of the PA lines. Different detuning regions are specified by different numeric labels and colors for both Case 1 and Case 2. Delta is the PA resonance position using Bragg scattering minus the PA resonance position using the absorption imaging (in MHz). All the data shown here is recorded with a probe (PA) laser power of  $25 \mu\text{W}$  and an uncertainty of not bigger than 0.2 MHz. All the regions 2-5 are explained in the text. All detuning are with respect to  $|F'=1\rangle$  state.

S.No.	Case 1				Case 2				
	Position (MHz)	RMSDS	RMSDA	Delta	Position (MHz)	RMSD	RMSDA	Delta	
1.	+686.0	0.000325	0.01603	+1	+1580.0	0.00838	0.00489	-1	4
2.	+655.5	0.00185	0.03512	+1	+706.0	0.01301	0.01548	-1	
3.	+618.0	0.00277	0.02673	-3	+671.9	0.00378	0.01352	-8.9	
4.	+576.0	0.00179	0.01292	-1	+647.6	0.00378	0.00737	-4	
5.	+525.5	0.0029	0.02514	-2	+614.0	0.00775	0.01019	-2	
6.	+465.5	0.00164	0.01525	+3	+594.3	0.00324	0.01104	-3.3	
7.	+394.5	0.000678	0.02702	+2	+582.7	0.00423	0.01756	-3	
8.	+312.0	0.000325	0.02041	-1	+558.0	0.0058	0.01598	-5	
9.	+216.5	0.00182	0.01596	-1	+488.5	0.00151	0.01305	-0.5	
10.	-140.0	0.00142	0.01939	-3	+420.7	0.00476	0.02996	-5	Region 5
11.	-174.0	0.000325	0.04394	-4	+391.7	0.008	0.05269	-1	
12.	-219.0	0.000497	0.01661	+6	+338.8	0.0089	0.00847	-3	
13.	-272.5	0.000862	0.02283	+8	+249.9	0.01835	0.02466	-2	
14.	-335.0	0.000940	0.01765	0	-90.4	0.00457	0.02768	-0.6	
15.	-525.0	0.00105	0.00905	0	-119.8	0.00076	0.02299	-0.2	
16.	-585.0	0.000325	0.00921	0	-143.1	0.00105	0.01088	-2	
17.	-740.0	0.000376	0.02223	0	-166.4	0.00238	0.01715	+5	
18.	-880.0	0.000995	0.00759	-5	-232.4	0.00524	0.00432	-0.6	
19.					-320.0	0.00127	0.01568	-1	Region 6
20.					-374.0	0.0022	0.01449	-1	
21.					-434.5	0.00204	0.00404	-1.5	
22.					-551.0	0.00116	0.01725	-2	
23.					-580.5	0.00177	0.00489	-1	
24.					-733.0	0.00291	0.01273	0	
25.					-759.3	0.00124	0.02036	0	
26.					-954.5	0.00515	0.04897	-3.5	
27.					-973.0	0.0032	0.01304	-1	



## 4.5 Summary of the chapter

I have presented the measured PA data using the two techniques in the Rubidium-87 Bose-Einstein condensate. This data is never reported before in a BEC or in hot gasses and is of extreme importance for the calculation of the hyperfine mixing in the otherwise asymptotic potential (for the precise measurement of the long range potential constants). The use of the Bragg scattering technique as a probe to detect the PA lines gives a superior signal to noise ratio in comparison to the conventional trap loss/absorption imaging technique. We also find that the higher atomic resonance line of the D1 line is anomalously broadened by the mixing of the strong PA lines in its vicinity as compared to the PA lines in other regions of the spectra. This anomalous broadening results in severe atom loss from the trap at moderately high powers of the probe laser and even distorts the shape of the atomic resonance. The use of a very weak probe power however, restores the Lorentzian shape of the atomic resonance line. We also report the unusual line lying above the total D1 line asymptote which is not predicted by any theoretical literature before. The importance of these spectral lines demands a complete theoretical modelling and fitting of the various PE curves to the data presented in this work and it can be the future direction for the theoretical molecular physics community.

## References

- [1] M. G. Peters, D. Hoffmann, J. D. Tobiason, and T. Walker. Laser-induced ultracold  $\text{Rb}(^5\text{S}_{1/2}) + \text{Rb}(^5\text{P}_{1/2})$  collisions, *Phys. Rev. A.*, 1994, 50, R906.
- [2] W. C. Stwalley and H. Wang. Photoassociation of Ultracold Atoms: A New Spectroscopic Technique, *Journal of Molecular Spectroscopy*, 1999, 195, 194.
- [3] H.R. Thorsheim, J. Weiner, and P.S. Julienne. Laser-Induced Photoassociation of Ultracold Sodium Atoms, *phys. Rev. Lett.*, 1987, 58, 2420.
- [4] P. S. Julienne and J. Vigué. Cold collisions of ground- and excited-state alkali-metal atoms, *Phys. Rev. A.*, 1991, 44, 4464.
- [5] J. Baron, W. C. Campbell, D. DeMille, J. M. Doyle, G. Gabrielse, Y. V. Gurevich, P. W. Hess, N. R. Hutzler, E. Kirilov, I. Kozyryev, B. R. O'Leary, C. D. Panda, M. F. Parsons, E. S. Petrik, B. Spaun, A. C. Vutha, and A. D. West. Order of Magnitude Smaller Limit on the Electric Dipole Moment of the Electron, *Science*, 2014, 343, 269.
- [6] C. Chin, R. Grimm, P. Julienne, and E. Tiesinga. Feshbach resonances in ultracold gases, *Rev. Mod. Phys.*, 2010, 82, 1225.
- [7] H. Yang, D. Zhang, L. Liu, Y. Liu, J. Nan, B. Zhao, and J. Pan. Observation of magnetically tunable Feshbach resonances in ultracold  $^{23}\text{Na}^{40}\text{K} + ^{40}\text{K}$  collisions, *Science*, 2019, 263, 261.
- [8] M. Theis. Optical Feshbach Resonances in a Bose-Einstein Condensate, in Faculty of Mathematics, Informatics and Physics. 2005, Leopold-Franzens-Universität Innsbruck.
- [9] A. Fioretti, O. Dulieu and C. Gabbanini. Experimental evidence for an isotopic effect in the formation of ultracold ground-state rubidium dimers, *J. Phys. B: At. Mol. Opt. Phys.*, 2007, 40, 3283.
- [10] D. DeMille. Quantum Computation with Trapped Polar Molecules, *Phys. Rev. Lett.*, 2002, 88, 067901.
- [11] C. J. Williams and P. S. Julienne. Molecular hyperfine structure in the photoassociation spectroscopy of laser cooled atoms, *J. Chem. Phys.*, 1994, 101, 2634.
- [12] J. L. Bohn and P. S. Julienne. Prospects for influencing scattering lengths with far-off-resonant light, *Phys. Rev. A.*, 1997, 56, 1486.

#### Chapter 4: Photoassociation of the $87\text{Rb}$ BEC near the D1 line threshold

- [13] P. O. Fedichev, Y. Kagan, G. V. Shlyapnikov, and J. T. M. Walraven. Influence of Nearly Resonant Light on the Scattering Length in Low-Temperature Atomic Gases, *Phys. Rev. Lett.*, 1996, 77, 2913.
- [14] E. R. I. Abraham, W.I. McAlexander, J. M. Gerton, R. G. Hulet, R. Côté and A. Dalgarno. Singlet s-wave scattering lengths of  $6\text{Li}$  and  $7\text{Li}$ , *Phys. Rev. A.*, 1996, 53, R3713.
- [15] M. W. Mancini, G. D. Telles, A. R. L. Caires, V. S. Bagnato, and L. G. Marcassa. Observation of Ultracold Ground-State Heteronuclear Molecules, *Phys. Rev. Lett.*, 2004, 92, 133203.
- [16] D. Wang, J. Qi, M. F. Stone, O. Nikolayeva, H. Wang, B. Hattaway, S. D. Gensemer, P. L. Gould, E. E. Eyler, and W. C. Stwalley. Photoassociative Production and Trapping of Ultracold  $\text{KRb}$  Molecules, *Phys. Rev. Lett.*, 2004, 93, 243005.
- [17] A. J. Kerman, J. M. Sage, S. Sainis, T. Bergeman, and D. DeMille. Production of Ultracold, Polar  $\text{RbCs}^*$  Molecules via Photoassociation, *Phys. Rev. Lett.*, 2004, 92, 033004.
- [18] C. Haimberger, J. Kleinert., M. Bhattacharya, and N. P. Bigelow. Formation and detection of ultracold ground-state polar molecules, *Phys. Rev. A.*, 2004, 70, 021402(R).
- [19] S. D. Kraft, P. Staunum, J. Lange, L. Vogel, R. Wester and M. Weidemüller. Formation of ultracold  $\text{LiCs}$  molecules, *J. Phys. B: At. Mol. Opt. Phys.*, 2006, 39, S993.
- [20] R. Wynar, R. S. Freeland., D. J. Han, C. Ryu, D. J. Heinzen. Molecules in a Bose-Einstein Condensate, *Science*, 2000, 287, 1016.
- [21] J. D. Miller, R. A. Cline, and D. J. Heinzen. Photoassociation spectrum of ultracold Rb atoms, *Phys. Rev. Lett.*, 1993, 71, 2204.
- [22] A. Gallagher and D. E. Pritchard. Exoergic collisions of cold  $\text{Na-Na}$ , *Phys. Rev. Lett.*, 1989, 63, 957.
- [23] M. E. Wagshul, K. Helmerson, P. D. Lett, S. L. Rolston, W. D. Phillips, R. Heather, and P. S. Julienne. Hyperfine effects on associative ionization of ultracold sodium, *Phys. Rev. Lett.*, 1993, 70, 2074.
- [24] E. R. I. Abraham, W. I. McAlexander., H. T. C. Stoof, and R. G. Hulet. Hyperfine structure in photoassociative spectra of  $^6\text{Li}_2$  and  $^7\text{Li}_2$ , *Phys. Rev. A.*, 1969, 53, 3092.

- [25] M. L. Almazor, O. Dulieu, F. Masnou-Seeuws, R. Beuc, and G. Pichler. Formation of ultracold molecules via photoassociation with blue detuned laser light, *Eur. Phys. J. D*, 2001, 15, 355.
- [26] A. Fioretti, D. Comparat, A. Crubellier, O. Dulieu, F. Masnou-Seeuws, and P. Pillet. Formation of Cold  $\text{Cs}_2$  Molecules through Photoassociation, *Phys. Rev. Lett.*, 1998, 80, 4402.
- [27] J. D. Weinstein, R. deCarvalho, T. Guillet, B. Friedrich, and J. M. Doyle. Magnetic trapping of calcium monohydride molecules at millikelvin temperatures, *Nature*, 1998, 395, 148.
- [28] H.R. Thorsheim, J. Weiner, and P.S. Julienne. Laser-induced photoassociation of ultracold sodium atoms, *phys. Rev. Lett.*, 1987, 58, 2420.
- [29] C. Gabbanini, A. Fioretti, A. Lucchesini, S. Gozzini, and M. Mazzoni. Cold Rubidium Molecules Formed in a Magneto-Optical Trap, *phys. Rev. Lett.*, 2000, 84, 2814.
- [30] M. Viteau, A. Chotia, M. Allegrini, N. Bouloufa, O. Dulieu, D. Comparat, and P. Pillet. Optical Pumping and Vibrational Cooling of Molecules, *Science*, 2008, 321, 232.
- [31] C. C. Tsai, R. S. Freeland, J. M. Vogels, H. M. J. M. Boesten, B. J. Verhaar, and D. J. Heinzen. Two-Color Photoassociation Spectroscopy of Ground State  $\text{Rb}_2$ , *phys. Rev. Lett.*, 1997, 79, 1245.
- [32] H. L. Bethlem, G. Berden, and G. Meijer. Decelerating Neutral Dipolar Molecules, *Phys. Rev. Lett.*, 1999, 83, 1558.
- [33] T. Takekoshi, B. M. Patterson, and R. J. Knize. Observation of Optically Trapped Cold Cesium Molecules, *Phys. Rev. Lett.*, 1998, 81, 5105.
- [34] Y. Huang, J. Qi, H. K. Pechkis, D. Wang, E. E. Eyler, P. L. Gould and W. C. Stwalley. Formation, detection and spectroscopy of ultracold  $\text{Rb}_2$  in the ground  $X^1\Sigma_g^+$  state, *J. Phys. B: At. Mol. Opt. Phys.*, 2006, 39, S857.
- [35] M. Kemmann, I. Mistrik, S. Nussmann, H. Helm, C. J. Williams, and P. S. Julienne. Near-threshold photoassociation of  $^{87}\text{Rb}_2$ , *Phys. Rev. A.*, 2004, 69, 022715.
- [36] D. Hoffmann, P. Feng, R. S. Williamson, III, and T. Walker. Excited-state collisions of trapped  $^{85}\text{Rb}$  atoms, *phys. Rev. Lett.*, 1992, 69, 753.

#### Chapter 4: Photoassociation of the $87\text{Rb}$ BEC near the D1 line threshold

- [37] A. Ciamei, A. Bayerle, B. Pasquiou and F. Schreck. Observation of Bose-enhanced photoassociation products, *EPL*, 2017, 119, 46001.
- [38] J. Javanainen and M. Mackie. Probability of photoassociation from a quasicontinuum approach, *Phys. Rev. A.*, 1998, 58, R789(R).
- [39] B. Ji, C. C. Tsi, and W.C. Stwalley. Proposed modification of the criterion for the region of validity of the inverse-power expansion in diatomic long-range potentials, *Phys. Rev. Lett.*, 1995, 236, 242.
- [40] L. Chen, P. Wang, M. Meng, L. Huang, H. Cai, D. Wang, S. Zhu, and J. Zhang. Experimental Observation of One-Dimensional Superradiance Lattices in Ultracold Atoms, *Phys. Rev. Lett.*, 2018, 120, 193601.
- [41] G. Birkl, M. Gatzke, I. H. Duetsch, S. L. Rolston, and W. D. Phillips. Bragg Scattering from Atoms in Optical Lattices, *Phys. Rev. Lett.*, 1995, 75, 2823.
- [42] P. Wang, L. Chen, C. Mi, M. Meng, L. Huang, K. S. Nawaz, H. Cai, D. Wang, S. Zhu, and J. Zhang. Synthesized magnetic field of a sawtooth superradiance lattice in Bose-Einstein condensates, *npj Quantum Information*, 2020, 6, 18.
- [43] O. Dulieu, R. Kosloff, F. Masnou-Seeuws and G. Pichler. Quasibound states in long-range alkali dimers: Grid method calculations, *J. Chem. Phys.*, 1997, 107, 10633.
- [44] P. D. Lett, K. Helmerson, W. D. Phillips, L. P. Ratliff, S. L. Rolston, and M. E. Wagshul. Spectroscopy of  $\text{Na}_2$  by photoassociation of laser-cooled Na, *Phys. Rev. Lett.*, 1993, 71, 2200.
- [45] A. Schilke, C. Zimmermann, P. W. Courteille, and W. Guerin. Photonic Band Gaps in One-Dimensionally Ordered Cold Atomic Vapors, *Phys. Rev. Lett.*, 2011, 106, 223903.
- [46] M. A. Kristensen, M. B. Christensen, M. Gajdacz, M., K.P. Iglicki, C. Klempt, J. F. Sherson, K., and A.J.H. Rzazewski, and J. J. Arlt. Observation of Atom Number Fluctuations in a Bose-Einstein Condensate, *Phys. Rev. Lett.*, 2019, 122, 163601.
- [47] C. McKenzie, J. H. Denschlag, H. Häfner, A. Browaeys, L. E. E. de Araujo, F. K. Fatemi, K. M. Jones, J. E. Simsarian, D. Cho, A. Simoni, E. Tiesinga, P. S. Julienne, K. Helmerson, P. D. Lett, S. L. Rolston, and W. D. Phillips. Photoassociation of sodium in a bose-einstein condensate, *Phys. Rev. Lett.*, 2002, 88, 120403.

Excitation spectrum and coherent phenomena in  $^{87}\text{Rb}$  Bose-Einstein condensates

[48] J. M. Gerton, B. J. Frew, and R. G. Hulet. Photoassociative frequency shift in a quantum degenerate gas, *Phys. Rev. A.*, 2001, 64, 053410.

[49] Y. Zhang, J. Ma, Y. Li, J. Wu, L. Zhang, G. Chen, L. Wang, Y. Zhao, L. Xiao, and S. Jia. Direct measurement of laser-induced frequency shift rate of ultracold cesium molecules by analyzing losses of trapped atoms, *Appl. Phys. Lett.*, 2012, 110, 131114.

## Chapter 5: Temporal dynamics of BEC in a 1D Optical Lattice

This chapter is based on my work that is not published but is in the manuscript preparation stage. Some background topics of the main experiment are discussed in the chapter including the main data. Here I discuss the series of experiments and also provide a plausible explanation of the features that we have observed in the experimental results. The discussion is more focused on the superradiance lattice (SL) but other two lattices are also used and discussed in context of their relevance to some experimental results of the SL.

### 5.1 Kapitza-Dirac diffraction of the BEC

Just like the diffraction of light from solid state gratings or diffraction of X-rays from crystal lattice planes, atoms can also diffract from the optical potentials formed by the interference pattern of two or more laser beams<sup>[1-3]</sup>. These diffracted atoms inside the optical interference pattern forms an ordered arrangement that mimics the properties of the ordered solid state crystals in many ways. For example, light can be diffracted from these atoms in the optical lattice in the same way as the diffraction of light from a solid state grating<sup>[4-7]</sup>. Several interesting properties of the atoms or the atoms+confining potentials and even molecules can be studied using these lattices, especially the use of ultra-cold atoms in optical lattices has emerged as a gigantic sub-field of the ultra-cold physics regime<sup>[2, 8-18]</sup>. Not only fundamental physics is studied using the ultra-cold atoms in optical lattices but also the commercial and technological applications of these systems are now starting to take shape<sup>[19-21]</sup>. In the following, a brief discussion is given about the two types of interpretations/pictures that are employed while studying the atom+optical lattice interactions.

#### 5.1.1 The grating picture of lattice diffraction

Two main pictures try to explain the diffraction of atoms by the optical lattices. In the grating picture of the atomic diffraction, the atoms acts as a wave via their deBroglie wavelengths and the optical lattice acts as grating through its light potential. The optical lattice through its variable AC stark shift regions (formed by the intensity maxima and minima) interacts with the atomic deBroglie wavelength and diffracts the matter waves. The classical optics rules can be used for the diffraction orders of the matter waves and any diffraction order  $m$  can be calculated by the matter waves diffraction equation  $m\lambda_{dB} =$

$d \sin \theta$ , with  $\lambda_{dB}$  being the deBroglie wavelength of the BEC (or non-degenerate but cold atoms) and  $d$  is the lattice constant dependent on the wavelength of the lattice beams. Since the deBroglie wavelength of the BEC is very large, the matter wave diffraction phenomenon of a BEC in an optical lattice system is often used by researchers to observe different fundamental phenomena of nature at the quantum level.

### 5.1.2 The Raman picture of lattice diffraction

An alternate picture of the atomic diffraction is the Raman picture in which the lattice changes the momentum states of the atoms after interaction with them (atoms considered as particles). This momentum change occurs through stimulated absorption and emission of photons from the interfering beams by the atoms. These absorbed and emitted photons transfers momentum kicks each of magnitude  $p = \hbar k$ ,  $k$  being the wave-vector of the beam from (to) which the photon is absorbed (emitted). Suppose the atoms are initially in the atomic ground state with zero momentum, then we can represent this system by the ket vector  $|g, 0\rangle$ . Similarly, an atom having absorbed a single photon from beam 1 is in the excited state having one quantum of momentum is represented by  $|e, 1\rangle$ . If this atom emits this photon into beam 2 of the lattice and goes to ground state then it has two quanta of momentum (kicks from photons during absorption and emission) and thus its ket vector is  $|g, 2\rangle$ . Then we can write the Hamiltonian for this system of atoms and lattice beams as a sum of the atomic Hamiltonian  $H_0$  and interaction Hamiltonian  $H_I$

$$H = H_0 + H_I \quad (5.1)$$

where the atomic Hamiltonian in the momentum basis is (in the rotating wave approximation)

$$H_0 = \hbar\omega_0 |e, 1\rangle\langle e, 1| + \hbar\omega_{rec} (|g, 0\rangle\langle g, 0| + |g, 2\rangle\langle g, 2|) \quad (5.2)$$

here  $\omega_0$  is the resonance frequency between the state  $g$  and  $e$  and  $\omega_{rec}$  is the recoil frequency of the atom defined by  $\omega_{rec} = \frac{\hbar k^2}{2m}$ . Similarly, the interaction part of the Hamiltonian is given by



## Chapter 5: Temporal dynamics of BEC in a 1D Optical Lattice

$$H_I = -\mu \cdot E = -ie^{-i\omega t} \frac{\hbar\omega_R}{2} (|e, 1\rangle\langle g, 0| - |e, 1\rangle\langle g, 2|) + h.c \quad (5.3)$$

where  $\mu = \langle e|e\vec{r}|g\rangle \cdot \hat{e}$  is the transition dipole moment between the internal excited and ground states of the atom and  $\omega_R = \frac{\mu E_0}{\hbar}$  is the Rabi frequency of the atomic transition amplitude for the given laser intensity and  $E_0$  is the resultant amplitude of the electric field of the two laser beams travelling in the  $z$ -direction. Since the lattice field is applied in a pulse form (of pulse shape  $f(t)$ ), the electric field of the lattice beams at any instant  $t$  can be written as (supposing we have two counter propagating beams having the same polarization  $\hat{e}$  and moving with wave vector  $k = \frac{2\pi}{\lambda}$  and wavelength  $\lambda$ )

$$E(z, t) = f(t)(E_0 \sin(kz - \omega t) \hat{e} + E_0 \sin(kz + \omega t) \hat{e}) \quad (5.4)$$

where the envelope function  $f(t)$  carries information about how fast are the lattice beams turned ON and OFF and for how long it is kept ON. This envelope function is very important for the type of diffraction that the atoms will undergo. The Fourier transform of the envelope function must not have frequency components that can diffract the atoms to higher momentum states than desired. In the time domain, this statement can be stated as the pulse width of the envelope function  $\tau$  must obey the following condition

$$\tau \gg \frac{\pi}{\omega_{rec}} \quad (5.5)$$

to make sure the atoms are only diffracted into the desired momentum states (having momentum space separation of integer recoil momentum). If this condition holds, then we call it the Bragg regime of diffraction. If this condition does not hold, the atoms can be even diffracted to the momentum states that are not integer multiples (fractional multiples as well) of the photon recoil momentum.

In the Bragg regime, the fraction of atoms that are scattered into the  $|g, 2\rangle$  state and lower momentum states can be found from the wave function

$$|\phi(t)\rangle = c_0 e^{-i\omega_{rec}t} |g, 0\rangle + c_1 e^{-i\omega_0 t} |e, 1\rangle + c_2 e^{-i\omega_{rec}t} |g, 2\rangle \quad (5.6)$$

Solving this to find the probability of atoms diffracted into the  $|g, 2\rangle$  state gives

$$P_2(\tau) = |c_2|^2 = \sin^2\left(\frac{\omega_R^{(2)}}{2}\tau\right) \quad (5.7)$$

where  $\omega_R^{(2)}$  is the two photon Rabi frequency given by  $\omega_R^{(2)} = \omega_R^2/2\delta$ , and  $\delta$  is the detuning of the laser beam from the atomic transition. This Eq. (5.7) gives the first order scattering/diffraction probability of atoms from the two counter-propagating laser beams. To get the atom to absorb photon from one beam and emit in the other beam, a detuning and a small angle between the two interfering beams is introduced which then makes sure that the atoms only absorb from one beam and emit into the other beam. This detuning is given by (for  $N$ th order scattering)

$$\delta_L = \frac{2N\hbar k^2}{m} \sin^2\left(\frac{\theta}{2}\right) \quad (5.8)$$

where  $\theta$  is the intersection angle between the two beams. This detuning will lead the scattering of atoms in only one direction<sup>[1]</sup> in the Bragg regime. However, if momentum transfer to the atoms in the BEC is to be only because of the lattice beams and not because of the spontaneous emission, the atom can still absorb a photon from one beam and emit it into the other so the momentum transfer in static lattice (no detuning between the beams) is every time  $\pm 2n\hbar k$  (scattering in both directions) as discussed below.

If the condition of Eq. (5.5) does not hold (the beams are turned ON for shorter times than required by Eq. (5.5) i.e. when  $\tau \ll \frac{\pi}{\omega_{rec}}$ ), then the scattering regime is called the Kapitza-Dirac scattering regime (also referred to as the Raman-Nath regime). This means that the Fourier transform of the lattice beams now have extra frequency components (introduced by the very fast temporal window during which the lattice is ON) that will scatter the atoms to higher momentum components that are not integer multiples of the

## Chapter 5: Temporal dynamics of BEC in a 1D Optical Lattice

original recoil momentum. Because this kind of interaction is momentary (for very short interval of time), the atoms in the BEC cannot move enough during the application of this pulse and thus we can neglect the atomic motion (second term) in Eq. (5.2). The atoms just feel a momentary potential (AC stark potential) given by

$$U(z, t) = \frac{\hbar\omega_R^2}{\delta} \sin^2(kz) f(t)^2 \quad (5.9)$$

This equation for the potential only holds for  $\delta^2 \gg \frac{\Gamma^2}{4}$ , where  $\Gamma$  is the excited state linewidth. This means that the detuning of the laser beams used for the lattice should be very large compared to the line-width of the excited state so that the imaginary part of the atomic dielectric coefficient does not take part in the interaction and only the real part of the dielectric coefficient is involved (in our experiment, this condition is satisfied very well). We suppose the total BEC wave function before the lattice application is  $|\psi(0)\rangle$  and after the application of the lattice potential, the wave function evolves due to the momentary interaction with the lattice beams to become (for  $f(t) \rightarrow 1$ , or ignoring the shape of the envelope function)

$$|\psi(\tau)\rangle = |\psi(0)\rangle e^{-i\frac{\omega_R^2\tau}{2\delta}\cos(2kz)} e^{-i\frac{\omega_R^2\tau}{2\delta}} \quad (5.10)$$

Similarly, in the momentum picture of the BEC, the BEC can be represented in the momentum basis in the lattice potential for the Kapitza-Dirac regime as well (like in Eq. 5.3). The probability of number of scattered atoms into the  $N$ th momentum state in the Kapitza-Dirac regime is thus given by the Bessel function of first kind  $J_N$

$$P_N = J_N^2(\omega_R^{(2)}\tau) \quad (5.10a)$$

A similar equation can be achieved while not ignoring the envelope function where the argument of the Eq. (5.10a) absorbs the envelope function. Changing the lattice illumination time and the power of the lattice beams will cause the probability of atoms in each momentum state to oscillate, a phenomenon called Pendellösung<sup>[22-25]</sup>, the oscillation cycle<sup>[3]</sup>

given by  $t = \pi\sqrt{|\Delta|/\omega_{rec}(\omega_R)^2}$ . The highest order momentum state is given by  $\bar{n} = \sqrt{\beta/\alpha}$ , where  $\beta$  depends on the two-photon lattice recoil energy and lattice pulse time and  $\alpha$  depends on the lattice depth and the lattice pulse time<sup>[24,25]</sup>. This oscillation for the zero and first order momentum states is shown in Fig. 5.1 (by plotting Eq. (5.10a)) for two different coupling beams powers. As we can see, the oscillation frequency increases with the increase in the coupling laser power.

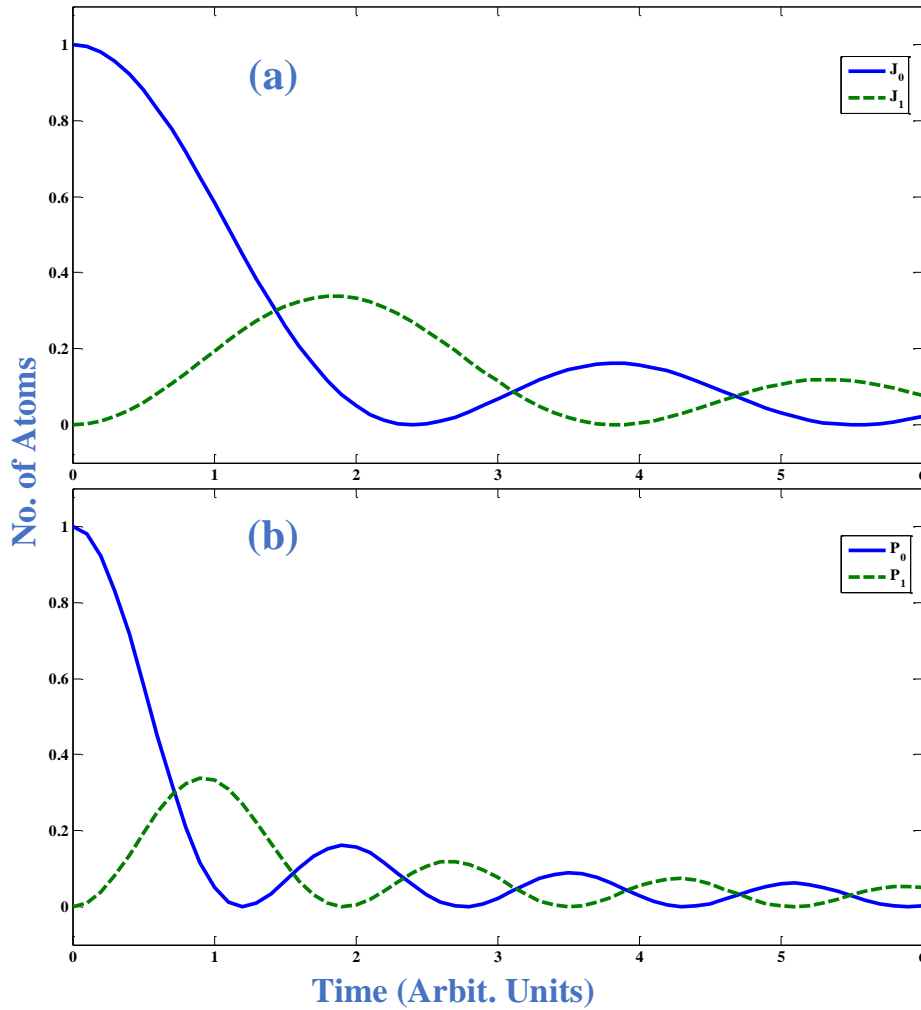


Figure 5.1. The dependence of the zero order ( $J_0$ ,  $P_0$ ) and first order ( $J_1$ ,  $P_1$ ) momentum states population on the illumination time of the coupling beams at two different power levels. Fig. (a) shows the population oscillation in the zero and first order momentum state at an arbitrary power “ $P$ ”. Fig. (b) shows the oscillations with illumination time for coupling beams power of “ $2P$ ”.

For longer pulse duration times, the individual lattice momentum states can also split due to atomic motion (a regime called the beyond Raman-Nath regime) but the time scales we use and the BEC temperatures, the initial few oscillations presented in our data falls in the Raman-Nath regime of the Kapitza-Dirac scattering<sup>[25]</sup> but may enter the beyond Raman-Nath regime and later the Bragg regime after several tens of  $\mu\text{s}$  of pulse duration (thick grating)<sup>[3]</sup>. Even in beyond the Raman-Nath regime and into the Bragg regime, the above theoretical models (or their modified forms<sup>[3]</sup>) predict the oscillation of the different momentum states population and this oscillation is what we are detecting here. So if there is any transition from one regime to the other during the experiment, it will only lead to the change of the oscillation frequency and the amplitude.

### 5.2 Superradiance

R. H. Dicke in his historical paper in 1954 proposed the possibility of coherence in the spontaneous emission from a molecular gas in a region of space with volume smaller than the wavelength of the emitted/exciting radiation<sup>[26]</sup>. He proposed that the smaller volume and higher density of the gas can compel the molecules to entangle in an excitation and emission process resulting in a coherent spontaneous emission process called superradiance. Later observation of the superradiance phenomenon in the optically pumped HF gas confirmed the validity of Dicke's theory of coherent spontaneous emission<sup>[27]</sup>. Superradiance and subradiance (opposite of superradiance) were also observed in trapped two ion system in 1996<sup>[28]</sup>. Since the superradiance phenomenon is universal, reports of its occurrence kept coming from other areas of physics like the observation of superradiance in photonic crystals<sup>[29]</sup>, in the matter waves due to Rayleigh scattering of BEC<sup>[30]</sup> by using a far detuned single laser beam or in a Bose-Einstein condensate which was coupled to an optical cavity<sup>[31]</sup>. This idea of the coherent spontaneous emission from excited state emitters was later extended to larger samples of atoms (of extent larger than the light wavelength used, for example the BEC of size  $20\ \mu\text{m}$  interacting with a  $795\ \text{nm}$  laser photon) by Scully<sup>[32]</sup>. He considered an ensemble of  $N$  atoms in a tight volume (dense medium) inside a crystal. A single photon incident on such an ensemble of atoms will be absorbed by it, and the interaction Hamiltonian for this system can be written as

$$H(t) = \sum_j \hbar g_0 \hat{\sigma}_j^\dagger \hat{a}_{\vec{k}_0} e^{i\vec{k}_0 \cdot \vec{r}_j} e^{-i(v_0 - \omega)t} + adj. \quad (5.11)$$

with  $\hat{\sigma}_j^\dagger = |a_j\rangle\langle b_j|$  being the transition operator from atomic ground state “ $b$ ” to atomic excited state “ $a$ ” where the atom is located at position  $\vec{r}_j$ . The photon absorption is represented by the annihilation operator  $\hat{a}_{\vec{k}_0}$  and  $g_0$  is the Rabi frequency of the single photon and N-atoms interaction.  $v_0 - \omega$  is the detuning of the laser (photon) frequency from the atomic transition frequency. The atoms and photon interacts via this time dependent potential and the system will change after the interaction according to the unitary time operator

$$U(\tau) = \zeta e^{-\frac{i}{\hbar} \int_0^\tau dt' H(t')}$$

After putting the values from Eq. (5.11), we get

$$U(\tau) \approx 1 - ig_0 \left( \int_0^\tau dt' e^{i(v_0 - \omega)t'} \sum_j \hat{\sigma}_j^\dagger \hat{a}_{\vec{k}_0} e^{i\vec{k}_0 \cdot \vec{r}_j} + adj. \right) \quad (5.12)$$

here  $\zeta$  is called the time ordering operator. We suppose the atomic+single photon wave function to be  $|b_1, b_2, b_3, \dots, b_N\rangle \otimes |1_{\vec{k}_0}\rangle$  initially which means that all the  $N$  atoms are in the ground state  $b$  and there is one photon travelling in the direction  $\vec{k}_0$ . After the absorption of the photon, the atoms+photon system evolves according to the unitary operator (Eq. 5.12) as

$$\begin{aligned} & U(\tau) |b_1, b_2, b_3, \dots, b_N\rangle \otimes |1_{\vec{k}_0}\rangle \\ & \approx |b_1, b_2, b_3, \dots, b_N\rangle \otimes |1_{\vec{k}_0}\rangle \\ & \quad - ig_0 \tau \sum_j e^{i\vec{k}_0 \cdot \vec{r}_j} |b_1, b_2, b_3, \dots, a_j, \dots, b_N\rangle \otimes |0\rangle \end{aligned} \quad (5.13)$$

Eq. (5.13) says that after the interaction, depending on the Rabi frequency  $g_0$  and interaction time  $\tau$ , the probability of the system in the initial state decreases and the system is excited to the new state  $|b_1, b_2, b_3, \dots, a_j, \dots, b_N\rangle \otimes |0\rangle$ . In this new state, there is no free photon and

one of the  $N$  atoms is now excited to the “ $a$ ” state. The normalized form of this new state of the system can be written as

$$|\Psi(N|1_{\vec{k}_0})\rangle = \frac{1}{\sqrt{N}} \sum_j e^{i\vec{k}_0 \cdot \vec{r}_j} |b_1, b_2, b_3, \dots, a_j, \dots, b_N\rangle \otimes |0\rangle \quad (5.14)$$

Now this system will decay and to represent the decay in mathematical equations, we construct the interaction Hamiltonian for emission (just like we constructed the absorption interaction Hamiltonian in Eq. 5.11 and the unitary evolution operator in Eq. 5.12). These equations are given below respectively

$$W(t) = \sum_j \sum_k \hbar g_k \hat{a}_k^\dagger \hat{\sigma}_j e^{-i\vec{k} \cdot \vec{r}_j} e^{it(v_{\vec{k}} - \omega)} + adj. \quad (5.15)$$

and

$$U_W(t) = \zeta e^{\frac{-i}{\hbar} \int_0^t dt' W(t')} = \prod U_W^j \quad (5.16)$$

where the matrix element for the  $j$ th atom is  $U_W^j = \hat{\gamma}_j^\dagger \hat{\sigma}_j$ , and the radiation operator

$$\hat{\gamma}_j^\dagger = \sum_{\vec{k}} \frac{g_{\vec{k}} e^{-i\vec{k} \cdot \vec{r}_j}}{\frac{i}{2}\gamma + (v_{\vec{k}} - \omega)} \hat{a}_{\vec{k}}^\dagger \quad (5.17)$$

The constant  $\gamma$  is called the Weisskopf-Wigner rate for spontaneous emission and is given by

$$\gamma = 2\pi \sum_{\vec{k}} |g_{\vec{k}}|^2 \delta(v_{\vec{k}} - \omega) \quad (5.18)$$

For large density systems,  $\sum_j e^{i(\vec{k}_0 - \vec{k}) \cdot \vec{r}_j} = \frac{N}{V} (2\pi)^3 \delta^3(\vec{k}_0 - \vec{k})$  and using the relation  $U_W^j |a_j\rangle = \hat{\gamma}_j^\dagger |b_j\rangle$ , we calculate the transition dipole matrix element between the excited and ground state atoms+single photon system as follows

$$\langle b_1, b_2, b_3, \dots, b_N | \Psi(N|1_{\vec{k}_0}) \rangle \approx \frac{\sqrt{N}}{V} \sum_{\vec{k}} \frac{(2\pi)^3 g_{\vec{k}}}{\frac{i}{2}\gamma + (v_{\vec{k}} - \omega)} \delta^3(\vec{k}_0 - \vec{k}) |1_{\vec{k}}\rangle \quad (5.19)$$

The right side of Eq. (5.19) shows that the emission probability (or transition dipole matrix element) is enhanced by  $\sqrt{N}$  provided the direction (wave vector) of the emitted light and the incoming absorbed photon is the same. This enhancement of the emission in a specific direction is called superradiance. These kinds of states are called the Tied-Dicke states. The Dirac-Delta function on the R.H.S of Eq. (5.19) ensures that the direction of the enhanced emission is the same as that of the absorbed light. This shows that in a larger density medium (in which the approximation  $\sum_j e^{i(\vec{k}_0 - \vec{k}) \cdot \vec{r}_j} = \frac{N}{V} (2\pi)^3 \delta^3(\vec{k}_0 - \vec{k})$  holds), the atoms can become entangled by the absorption-emission process alone. The large density requirement is very crucial as the approximations employed when calculating the Eq. (5.19) are only valid if the density is large. At smaller densities, the reverse of superradiance (subradiance) can occur<sup>[33]</sup>.

An important experimental hurdle in the observation of such superradiance emission is the difficulty to isolate the superradiance emission from the excitation light as both are in the same direction. A scheme that can change the direction of the superradiance emission while still satisfying the Dirac-Delta condition is thus necessary to extract useful information from the superradiance light without the background excitation light.

### 5.3 Superradiance Lattice

Now consider the case of a BEC in a superradiance lattice (SL). The construction of SL was discussed in the previous chapter (Photoassociation using Bragg scattering). The mathematical details are almost the same as for the superradiance discussed in the previous section. This time we add two more laser fields in addition to the first field that excites the atoms from the ground state “*a*” to the excited state “*b*”.

Let us change the labels of the ground and excited states respectively to *g* and *e* instead of *b* and *a* to keep the formalism similar to the one discussed in Ref.<sup>[34, 35]</sup>. The first field (weak laser beam) which excites the atom from ground state *g* to the excited state *e* is called the probe field (again this name is coming from the conventional role of a weak laser in the coherent systems like EIT). We chose the rubidium-87 atom for the implementation



of this SL scheme. The ground state  $g$  is the upper ground state  $g = |F = 2, m_F = 2\rangle$  of the 5S fine level and the excited state is the lower excited line  $e = |F' = 1\rangle$  state of the D1 line. The second field (strong laser beam) couples the excited state  $e$  with an intermediate level  $m$  and we call it the coupling field. The intermediate level is the lower ground hyperfine level  $m = |F = 1\rangle$ . If we arrange the coupling field in such a way that it shines on the atoms from two directions making an angle  $\theta$  with each other (two laser beams of the same coupling frequency intersect each other at the position of the atoms in the BEC having same direction of polarization and therefore forms interference pattern), then a lattice is formed by these two coupling fields/beams. The wave vectors of the two coupling fields are  $k_1$  and  $k_2$  respectively and that of the probe field is  $k_p$  as shown in Fig. 5.2(b). In case of single excitation (probe) field, there were only atoms with zero momentum and atoms with 1 quantum of momentum along the direction of the incident laser (as discussed in the preceding section), but now there will be several more momentum states in other directions too due to the introduction of two coupling fields (the coupling fields facilitate the quantum transport of atoms in the momentum space).

As we can see from Fig. 5.2(a, b), the probe field excites the ground state atom from the  $|g\rangle$  to  $|e\rangle$  (shown in Fig. 5.2(a) by  $e_0$ ) from where it decays to  $|m\rangle$  by emitting a photon

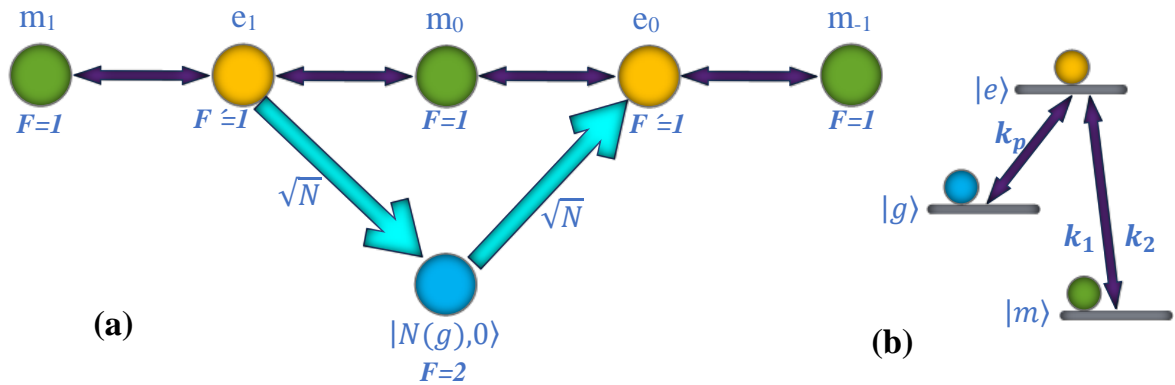


Figure 5.2. Figure (a) shows the quantum transport of atoms in the momentum chain in the SL. (b) The locking scheme of the lasers and the energy levels of the Rb atom.

in the direction of  $k_1$  to become  $|m_{k_p-k_1}, n_1 + 1, n_2\rangle$ , where  $n_1, n_2$  are the number of photons in the coupling beams 1 and 2 respectively while the atom is in the excited state. The state  $|m_{k_p-k_1}, n_1 + 1, n_2\rangle$  means that there are now  $n_1 + 1$  photons in the coupling 1 beam and  $n_2$  photons in the coupling 2 beam and the excited atom has now decayed to the state  $|m\rangle$ . In Fig. 5.2(a), this decayed state is shown by  $m_{-1}$ . From here the atom can absorb a photon from the coupling beam 2 to go back to an excited state in the momentum chain designated by  $e_{-1}$  (not shown in Fig. 2). This  $e_{-1}$  state can be represented by  $|e_{k_p-k_1+k_2}, n_1 + 1, n_2 - 1\rangle$ . Or it can absorb a photon from the coupling field 1 and go back to the same excited state  $e_0$ . The  $e_0$  can also go on the left side of the momentum chain and emit a photon into the coupling 2 beam direction and convert the atomic state to  $m_0$  from where it can absorb a photon from the coupling field 1 to get excited to the  $e_1$  state. This state can be represented by  $|e_{k_p+k_1-k_2}, n_1 - 1, n_2 + 1\rangle$ . This state can superradiantly couple to the original ground state by emitting a photon in a specific direction. Although many of the excited states are superradiant due to the large density of the BEC but the directional emission can only happen in only one of the excited state due to the fixed angle of the probe laser. Let us say that it is this  $e_1$  state. Atoms following the triangle formed by the arrows indicated in Fig. 5.2(a) will radiate superradiantly and will end up back in the same ground state.

The same Eq. (5.11) holds for the first excitation part of the atom from ground state to the excited state as the initial interaction Hamiltonian. However, the addition of the two coupling fields which couple the excited state  $e$  with an intermediate level  $m$ , introduces an extra Hamiltonian given by

$$H_{IC} = - \sum_j \hbar \left( g_1 \hat{a}_{\vec{k}_1} e^{i\vec{k}_1 \cdot \vec{r}_j} + g_2 \hat{a}_{\vec{k}_2} e^{i\vec{k}_2 \cdot \vec{r}_j} \right) |e_j\rangle \langle m_j| + adj. \quad (5.20)$$

Following the same procedure of the unitary evolution operator and then calculating the transition dipole matrix element between the excited state  $e_1$  and the ground state  $g$ , we will get an equation that will contain a Dirac-Delta function as a function of the wave-vectors  $k_p, k_1$  and  $k_2$ . Because of the addition of the two coupling fields, the superradiance emission direction will now be in some other direction and not in the direction of the probe field. Fortunately, this emission direction can be found by the conservation of linear

momentum relation  $k_e = k_p - l(k_1 - k_2)$  where  $l$  is an integer<sup>[7]</sup>. For those values of  $k_e$  the emission will be superradiant at which  $|k_e| = |k_p|$  and at all other values there will be normal spontaneous emission. In Ref.<sup>[34]</sup>, they found that the SL can be realized within a standing wave coupled electromagnetically induced transparency (EIT) scheme in a  $\Lambda$ -type system and that the density of states of the SL resemble that of the EIT absorption spectrum.

This was later experimentally demonstrated in Ref.<sup>[35]</sup>. The typical SL spectrum as a function of the probe laser frequency is shown in Fig. 5.3. The two peaks of the SL are coincident with the two dressed states of the EIT system but what makes it different from EIT is the transparency window as it still has some absorption due to the presence of small number of density of states.

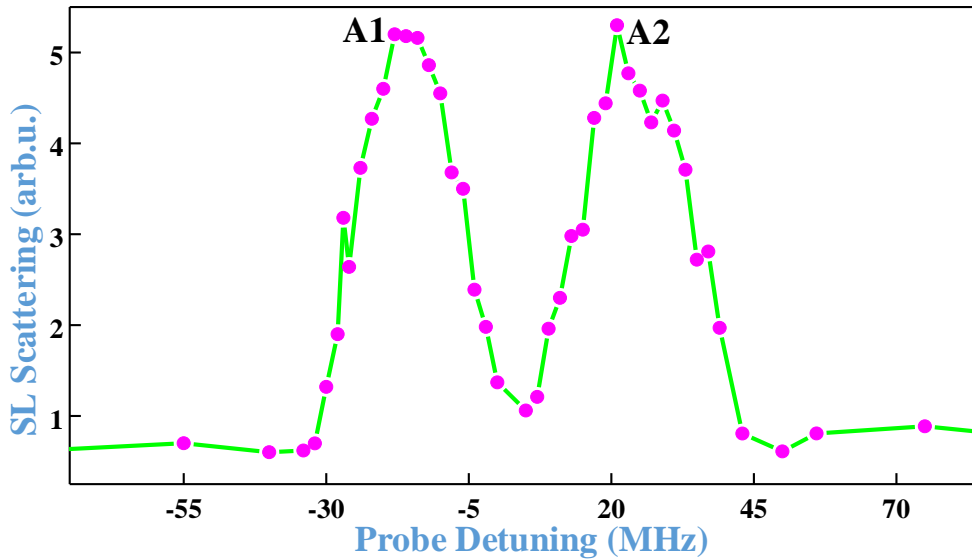


Figure 5.3. The SL scattering frequency domain spectrum as function of the probe laser frequency. The two main peaks of the SL spectrum coincides with the positions of the two dressed states of the EIT system and are marked by the letters A1 and A2.

These small number of density of states becomes important when we add another lattice standing wave field to the existing SL lattice<sup>[36]</sup>. This Fig. 5.3 was recorded by scanning the probe laser frequency while collecting the highly directional scattered light with the help of an EMCCD camera.

## 5.4 Superposition of the SL on a phase modulated BEC

If the BEC (in the  $|F = 2, m_F = 2\rangle$  state) is loaded into the optical lattice (made by the coupling laser at 795, which is blue detuned in the absence of the probe laser) in the Kapitza-Dirac regime (without turning ON the excitation probe laser) for a variable time, then we can see from Eq. (5.10a) that the population of the ground state and other momentum states will oscillate with time due to the time dependent phase modulation. All the atoms in this lattice will be in the ground electronic state as the coupling beams are locked around 6.8 GHz above the nearest resonance transition of the  $^{87}\text{Rb}$  atoms, and the potential energy experienced by the atoms is due to the AC stark shift of the lattice. The lattice will write a variable phase on the BEC wave function depending on the application time/depth of the lattice pulse. Now, if we suddenly turn on the probe laser while keeping the coupling lasers ON, all the ground state atoms in the lattice will be pumped by the probe laser to the lower excited hyperfine level (Fig. 5.2(b)). Those atoms in the phase modulated BEC which satisfy the  $k_e = k_p - l(k_1 - k_2)$  condition will emit light directionally in a superradiant manner (when using the SL) and as the population of these atoms for the variable delay between the probe and the lattice beams will oscillate according to Eq. (5.10a), we will observe oscillations in the scattering intensity also. This superradiance emission coming out of the total system actually carries the information of the phase imprinted by the application of the Kapitza-Dirac pulse of the coupling beams to the original BEC and can act as an in-situ technique for the measurement of the phase imprint from the Kapitza-Dirac lattice without waiting for the longer and noisy TOF times. Since the BEC's Thomas-Fermi size is around  $20\ \mu\text{m}$  and the recoil momentum imparted by the D1 line laser wavelength in each scattering event is just 3.6325 KHz, the time needed by the atoms to leave the BEC cloud and to arrange into a resolved momentum distribution is very large (tens of ms). Therefore, the use of the SL scattering for the observation of these oscillations in-situ is a very powerful tool. Another usefulness of the SL in-situ probing is the avoiding of the noise adding expansion times that are needed to properly resolve the scattered atoms into their momentum states. As discussed in previous chapter (Chapter 4), the vibrations in the imaging optics adds noise to the data in the form of interference fringes<sup>[37]</sup> and this noise can reduce the precision of the measurement of the actual phase imprinted by the Kapitza-Dirac pulsed lattice on the

BEC. Other measurements using the variable delay method include the precise measurement of the lattice depth<sup>[38]</sup> as the optical lattice depth measured from the power in the lattice beams directly has limitations as the power actually reaching the atoms inside the vapor cell may not be the same as measured outside the vapor cell.

If the lattice laser wavelength is changed to some other value (use 780 nm or 1064 nm lattice) while using the same probe (at 795 nm) so that the EIT configuration of Fig. 5.2b is no more, we can still have directional non-superradiant scattering of probe light (as a result of atoms excited by the resonant probe laser spontaneously emitting) provided that the atoms have a momentum state for which the condition  $k_e = k_p - l(k_1 - k_2)$  is still met<sup>[7, 25]</sup>. The use of a 780 nm lattice in the same configuration (same angles between the lattice/coupling and the probe beams discussed in 5.5.1) as in Fig. 5.4 (which is the SL setup for recording the SL scattering using the 795 nm laser as the coupling or lattice laser) will still give enough scattering as the wavelength difference is not big. However, the use of a 1064 nm lattice will need changing the probe laser angle so that the phase conservation condition  $k_e = k_p - l(k_1 - k_2)$  is satisfied<sup>[7, 25]</sup>. These lattices other than in the SL configuration will still show similar oscillations in the intensity of the scattered light (due to the oscillation in the population of the atoms having momentum that satisfy the phase conservation condition) depending on the depth and the application time of the lattice, as we will see in the next sections.

### 5.5 The Experiment and discussion

The experiment uses the same platform for the production of BEC that was used for the experiments in the previous chapters. However, the experimental scheme for the measurement of the SL or non-superradiance lattices (non-SL) with variable delay is different from the previous chapter sequences. In the following I discuss the setup and the sequence of the experiment in detail. If we use the 795 nm laser for the lattice, we call it the SL. The non-SL lattices are separately formed using the 785 nm or the 1064 nm lasers. The probe laser stays the same (795 nm) in all of these lattice scattering experiments.

### 5.5.1 Experimental setup

The sketch of the experimental setup is shown in Fig. 5.4. The three laser beams are shown incident on the BEC in the plane of the paper all having vertical (along the normal of the paper) polarization. For the SL lattice study, the two coupling beams (or lattice beams) make an angle of  $48^\circ$  degrees at the intersection point (at the BEC). A small magnetic field along the normal to the page is present during the application of the experimental beams to the BEC. The probe P and scattered beam S makes an angle of  $132^\circ$  with each other in the plane of the paper. The probe laser beam also makes a small angle of  $11^\circ$  with the plane of the paper. The coupling beams are switched ON and OFF with the help of an acousto-optic modulator (AOM) which is turned OFF and ON by the control PC with the help of driving electronics. The probe laser is switched ON and OFF with the help of an electro-optic intensity modulator (EOIM) (fiber coupled EO SPACE Broadband (10-40+ GHz), low-loss LiNbO<sub>3</sub> modulator AZ-0S5-20-PFU-780-UL). Additional beam blocking is done with the help of mechanical shutters used in combination with AOMs. The EOIM cannot change the frequency of the probe laser. The EOIM has a very sharp rise and fall time (limited by the driving Arbitrary Function Generator speed) and is controlled by the Arbitrary Function Generator (SG) (Tektronix AFG 3252). The same trigger sent by the computer (PC) activates the SG and the coupling beams controlling AOM but the SG is capable of introducing a time delay during the turning ON of the EOIM after it receives the trigger from the PC. This is useful in scanning the delay between the coupling and the probe laser beams. The same configuration of lattice beams and probe beam is used for studying the non-superradiance 780 nm laser lattice, but for the 1064 nm lattice a 1064 nm beam is retro reflected to form the lattice and the incident probe (795 nm) laser and the scattering light both now make angles of  $+41^\circ$  and  $-41^\circ$  with respect to the 1064 nm beam/lattice axis. The remaining control is done in the same manner as for the SL lattice. The EOIM output is very sensitive to temperature fluctuations and thus a Thorlabs temperature controller (model TED 200 C) is employed which, with the help of two thermoelectric coolers and a temperature sensor keeps the temperature of the EOIM stable (we set the TED 200 C controller at an easily achievable and stabilizable temperature, any temperature is okay just

the stability is important). The EOIM is mounted on a copper slab which is then mounted on the thermoelectric cooler which is then put on the optical table.

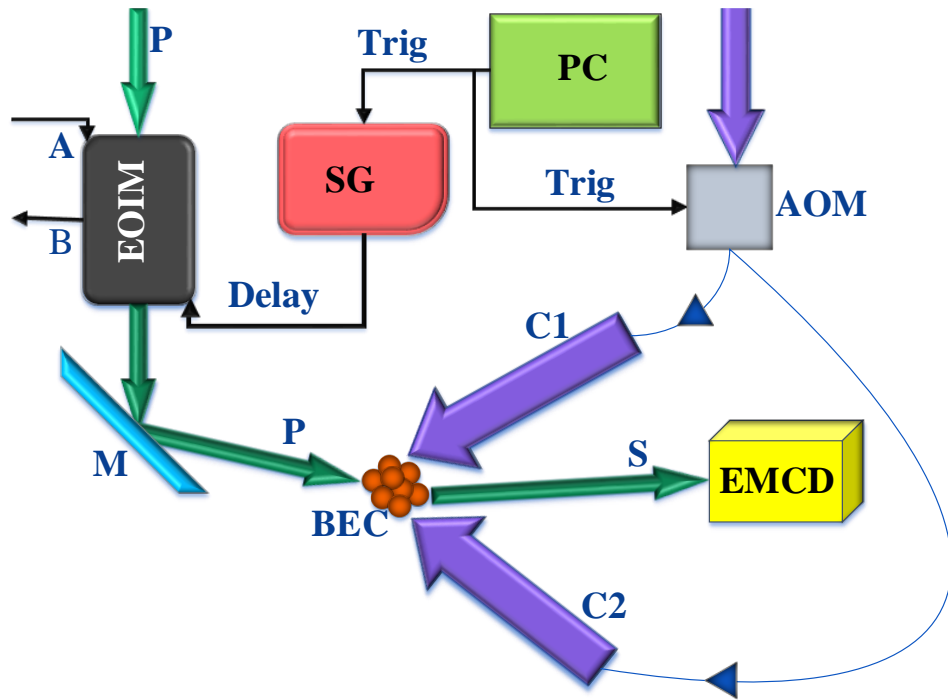


Figure 5.4. The experimental setup for the phase delay study of the lattice. C1 and C2 are the two coupling or lattice beams in the SL lattice configuration. P is the probe and S is the highly directional scattered light. AOM does the switching of the two coupling beams. PC is the personal computer that sends the triggers to the AOM and the SG (Arbitrary Function Generator). The signal generator switch (after a variable delay) the EOIM. M is the  $45^{\circ}$  highly reflective mirror. A and B are the temperature control and observation ports to maintain the EOIM at fixed temperature. Another port (not shown here) does the DC biasing of the EOIM which determines how much optical power it leaks when OFF.

The frequency of the coupling laser is fixed (Fig. 5.2(b)) and the frequency of the probe laser can be scanned via the OPLL discussed in the previous chapters. However, the OPLL is just used to keep the phase relationship between the coupling and the probe lasers in this experiment, and the probe frequency is kept fixed at either A1 or A2 peaks of Fig. 5.3.

### 5.5.2 Experimental sequence

Right after the BEC is prepared in the dipole trap, a minimum dipole trap depth is kept turned ON that still holds the atoms from falling down due to the force of gravity. Then the computer (PC) sends a trigger out which turns ON the AOMs controlling the coupling and probe laser beams. The same trigger activates the delay counter in the SG simultaneously. The coupling lasers forms the blue detuned standing wave on the BEC position while the probe laser beam is not allowed to pass through the EOIM and onto the BEC. The turning ON/OFF of the coupling/lattice beams (and its duration) is abrupt and falls in the Kapitza-Dirac regime for all of the data we present here. After a variable/programmable time delay  $\tau$ , the SG forwards the trigger (in the form of a single pulse of width 1  $\mu$ s) to the EOIM to turn ON the probe laser passing through the EOIM. The probe laser then illuminates the BEC together with the coupling beams for the pulse time  $t$  (1  $\mu$ s) and then turns OFF while the coupling beams in each experimental run stays ON for a fixed time and then turns OFF abruptly. During this illumination of the probe laser, the EMCCD camera records the

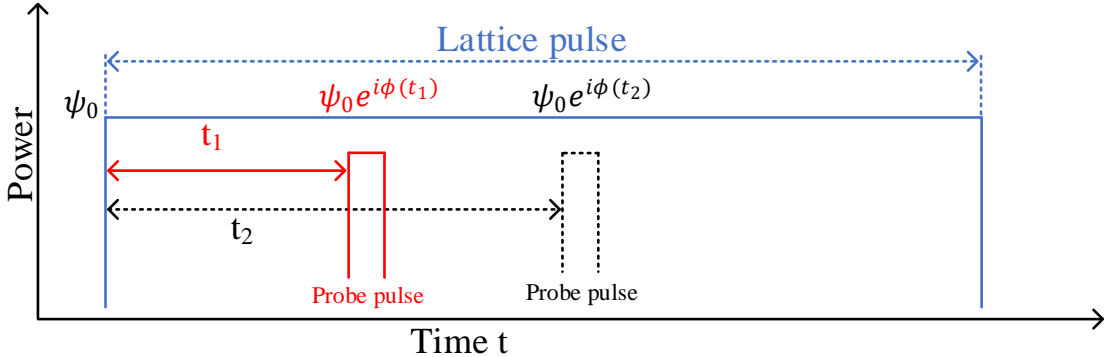


Figure 5.5. The time sequence of the experiment showing the evolution of the BEC wave function with time and its probing at different times by the probe laser. Times  $t_1$  and  $t_2$  correspond to two different measurement sequences on different BEC samples.

superradiance scattering from the SL (or spontaneous but directional scattering from the non superradiance lattice) and sends it to the PC for further processing by an image processing software. Then a new time delay is set and the experiment is repeated three times for each delay value. The scattering SL signal against each delay time between the coupling laser



and the probe laser is plotted to get the oscillations resulting from the Pendellösung. The probe laser frequency is set at one of the two peaks of the superradiance lattice spectrum. The frequency at A1 is -18 MHz red detuned from the  $F=1$  to  $F'=1$  transition resonance and the A2 peak is situated at 19 MHz blue detuned from the same atomic resonance transition at 200  $\mu\text{W}$  of coupling and 47  $\mu\text{W}$  of probe laser power. However, this value changes slightly for the non superradiance lattices which is found by scanning the probe laser frequency. In similarity to the two dressed states of the  $\Lambda$ -type system, the two peaks shift their position in response to change in the power and detuning of the coupling laser. After the experiment is finished, all the laser beams including the dipole trap beams are extinguished and the experimental sequence starts again from the loading of the MOT. The experimental sequence for the lattice and probe beams is shown in Fig. 5.5. The BEC wave function after its preparation is shown by  $\psi_0$  which after the application of the pulse changes with time and the probe laser probes it at these different times and this is how the population of the particular phase/momentum states is probed.

### 5.6 Experimental Data

In this section the experimental data is presented and the effect of various experimental parameters on the scattering signal is discussed. Each point in the figures is the average of three points.

#### 5.6.1 Effect of lattice power

Fig. 5.6 shows the SL scattering intensity as a function of the time delay for different coupling laser powers. The increasing power of the beams increases the depth of the lattice potential which out-couples atoms to higher and higher momentum states (as already seen from Eq. 5.10a and from Fig. 5.1). All the momentum states are pumped to and from the zero momentum state directly or connected through intermediate momentum states (in the absence of the probe laser). Increasing the number of momentum states increases the oscillation rate of the population in the zero order and higher order momentum states and hence of the SL scattering intensity. This oscillation of intensity of the superradiance scattering can be regarded as “superradiance–Pendellösung”.

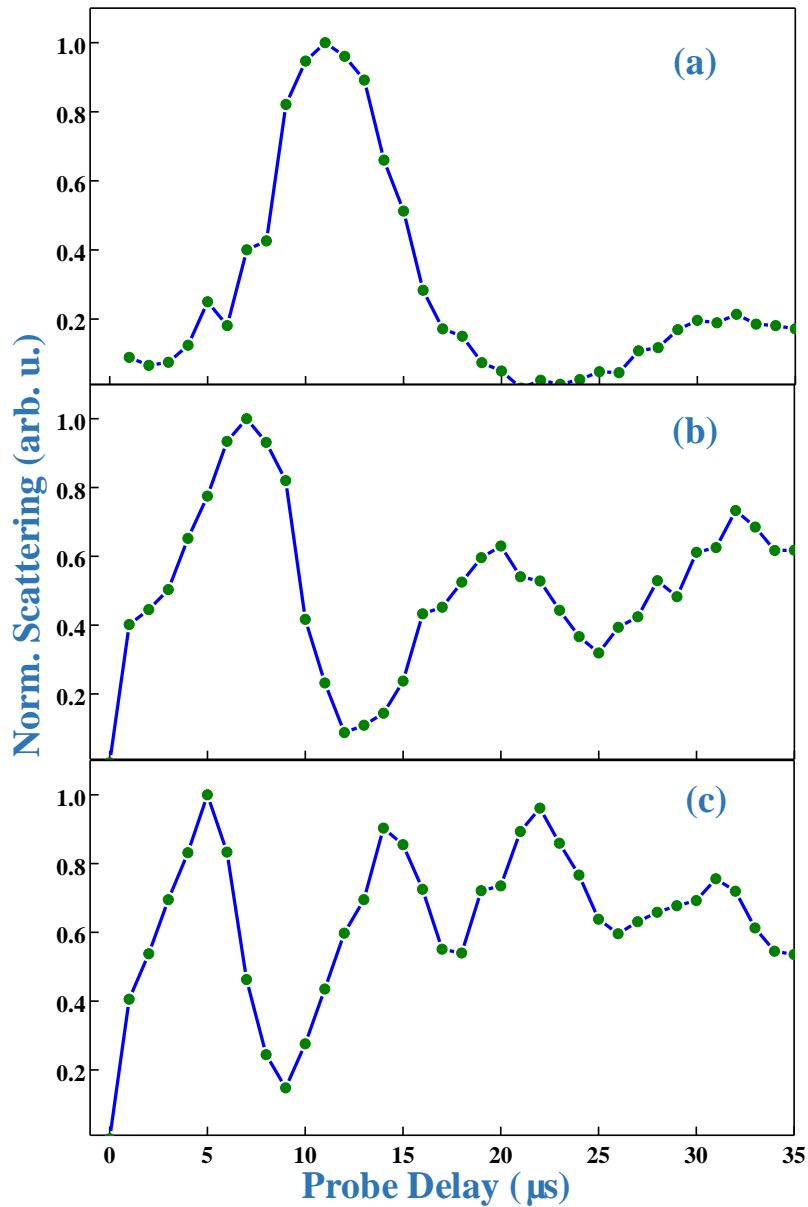


Figure 5.6. The effect of the coupling power on the oscillation rate of the scattered intensity. (a) Each coupling beam power is  $100 \mu\text{W}$  (b)  $200 \mu\text{W}$  (c) and  $400 \mu\text{W}$ . The probe laser power was  $47 \mu\text{W}$  and its frequency was kept fixed at the A1 peak in Fig. 5.3. The illumination time for coupling beams is  $50 \mu\text{s}$  in each run of the experimental sequence. The scattering superradiance intensity recording by the EMCCD takes place during the probe illumination time only. Each point in these figures is the average of three points. The points are connected with each other by the solid lines. Each signal is independently normalized due to the difference in total scattered intensity.

## Chapter 5: Temporal dynamics of BEC in a 1D Optical Lattice

Although I do not present the complete mathematical model<sup>[24]</sup> here for what exactly is happening, but the description presented here gives an acceptable understanding of the dependence of the superradiance scattering amplitude on the instantaneous population of the superradiant state momentum ( $e_1$  state). As the probe laser is OFF in the beginning, there should be no  $e_1$  state. However, as the coupling laser already out-couples atoms into various momentum states (atoms situated at different locations of the interference pattern experience different force or phase) in the absence of the probe laser, there is one momentum state with atoms in the ground state that becomes superradiant immediately after the application of the probe laser (it satisfies the phase conservation condition for directional emission) and thus the instantaneous population in that state gives how much light should be emitted through the directional SL scattering. Similarly, the non SL lattices provide the directional scattering because of the phase conservation requirement and the spontaneous emission of the atoms from these lattices carry the BEC phase information in the same way as the SL but the intensity of the scattered light is less than the SL.

The SL scattering intensity also changes with the coupling beams power and therefore the height of each curve in Fig. 5.6 is not the same (and thus each curve is independently normalized so that we can focus on the oscillation period only). This is because with increase in the coupling laser power, not only the frequencies of the Peaks A1 and A2 shifts but also the heights of these peaks change. Also, the SL scattering light intensity reduces with increasing the probe delay due to that fact that at higher delays the higher and higher momentum states gets populated and with time the atomic cloud expands and it becomes difficult to bring back the atoms to the zero momentum state and thus the visibility of the oscillating signal becomes smaller and smaller (at higher delay times, the atoms actually move in real space and the lattice pulse is not just imprinting a phase on the BEC but its AC stark force is moving the atoms in real space)<sup>[7]</sup>. Also, at larger delay times, the lattice may enter the beyond Raman-Nath regime and later the Bragg regime and even the beyond Bragg regime (which means that the lattice pulse is now not capable of diffracting any atoms into any momentum states and thus the oscillations appear to damp)<sup>[1]</sup>.

### 5.6.2 Effect of delay on Peaks A1 and A2

The height of the two peaks in the SL spectrum changes with angle of the probe laser and is already studied in Ref.<sup>[35]</sup>. But we have found that the height of two peaks can also change with the probe delay (or the exposure time of the atoms to the coupling beams only).

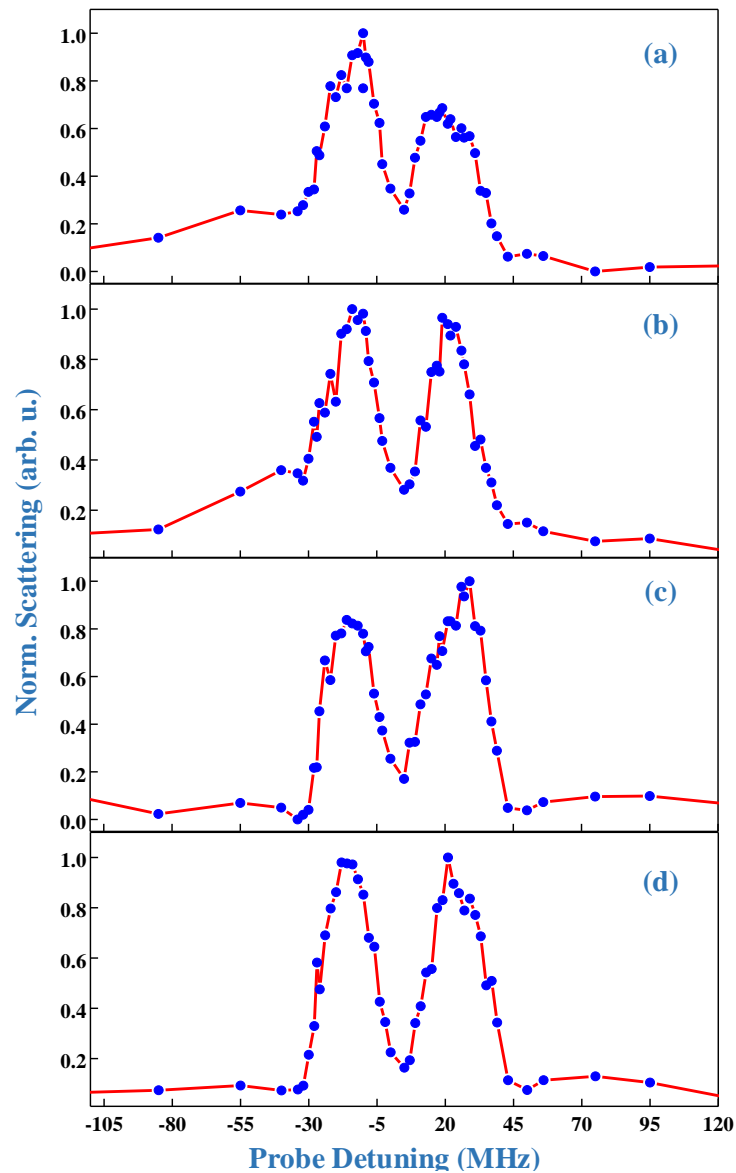


Figure 5.7. The changing probe delay time clearly changes band structure of the SL, especially on the main SL peaks A1 and A2. The intensity vs probe detuning is plotted for a probe delay of (a)  $8\ \mu\text{s}$  (b)  $12\ \mu\text{s}$  (c)  $20\ \mu\text{s}$  and (d)  $26\ \mu\text{s}$ .

This means that the different SL band regions do not repopulate at the same rate when the delay between the two coupling beams and the probe is increased. This effect is shown in Fig. 5.7. This kind of effect was not detected in previous studies on slightly hotter atoms in

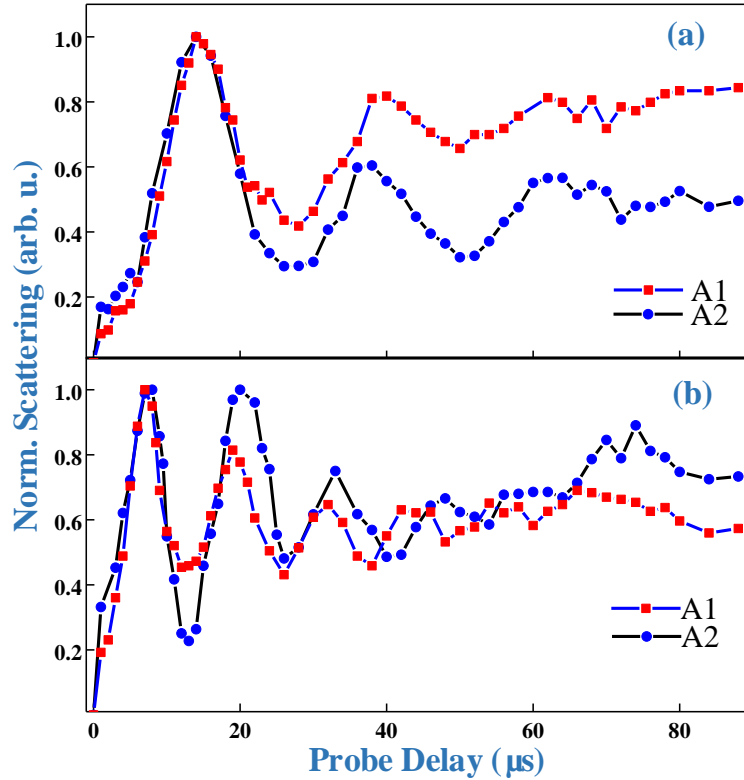


Figure 5.8. A comparison of the SL signals recorded using the SL peaks A1 (squares) and A2 (circles). The intensity vs probe delay plots shown here are (a) When the coupling beams power  $50\mu\text{W}$  and (b)  $200\mu\text{W}$  each is used. The small relative phase between the two SL peaks A1 and A2 becomes evident when a stronger coupling power is used. The two curves start departing after  $20\mu\text{s}$  of delay showing the population in one of the peaks (A1) changes faster compared to the other peak (A2).

a MOT (inset of Fig. 2 in Ref.<sup>[7]</sup>) and thus need further studies, from both experimental and theoretical viewpoints. Our experiments (both Fig. 7 and 8) however confirms the existence of a phase relationship between the two peaks. In Fig. 5.8 this becomes more clear when the delay signal is recorded using the two peaks separately. The phase delay between the two peaks is not clear for lower coupling laser power (because of the low oscillation frequency at low power) but at higher power the two signals starts to depart and one starts lagging the other one in time, showing the population in one of the peaks (A1) changes faster compared

to the other peak (A2) (this implies that the SL energy band has a temporal dispersion as well!). This effect predicts that the time at which the probe laser is turned ON (and thus the blue detuned lattice becomes an SL) is also important and thus plays a role in the population of the different states of the SL band and thus the other momentum states do play a role in the SL. To verify this result we need a complete theory of the SL with a phase modulated (in the Kapitza-Dirac regime) BEC and also need to further design clever experiments.

This behavior of the change of the peaks is characteristic of the superradiance lattice (SL) only, as only the SL has a spectrum with two prominent peaks. BEC in the 780 nm or 1064 nm lattices shows just a single peak at the probe resonance at the  $F=2$  to  $F \simeq 1$  atomic transition (the peak shifts slightly due to the AC Stark shift of the energy of the given transition) and there are no other peaks in these lattices. The atoms in the 780 nm are excited by the probe resonant with the before-mentioned transition while in the 1064 nm lattice the probe is red detuned by around 700 MHz due to low scattering at the resonance frequency.

### 5.6.3 Effect of the dipole trap

The experimental data shown so far is for the cases when the experimental beams (two coupling and one probe) are applied to the BEC in the presence of a weak dipole trap. The experimental beams can also be applied to the BEC immediately after the dipole trap power is turned OFF and similar behavior can be observed. In Fig. 5.9, a comparison is shown between the scattering from the lattices inside and outside the dipole trap. A small phase difference can be observed between the signals during the first oscillation period showing that the atoms oscillation inside the dipole trap is faster compared to when outside the trap. The exact reasons are not clear as a detailed theoretical treatment is needed which should simulate the Eq. (5.10a) in the presence of dipole trap potential and consider the GP equation for any mean field effects<sup>[25]</sup> (although this potential is weak as this is the last step of the dipole trap evaporation and is used only to stop the BEC from falling down due to gravity). However, the data suggests that the dipole trap helps the atoms repopulate the zero and other momentum states after scattering by the two lattice (coupling) beams. Outside the

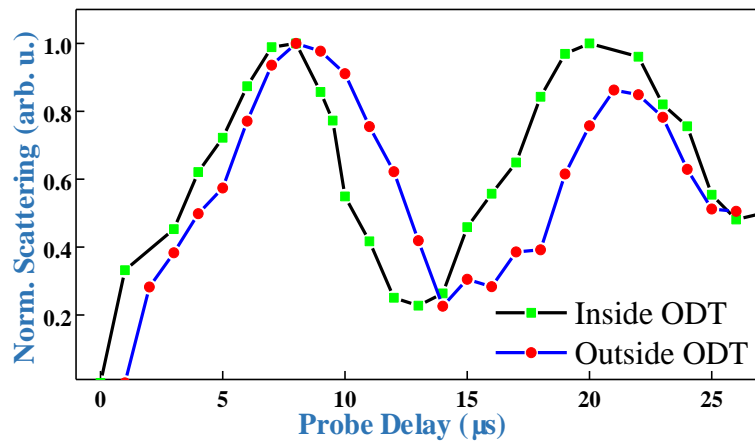


Figure 5.9. A comparison of the two SL scattering vs probe delay signals when the experiment is performed inside and outside the optical dipole trap. The coupling laser power in each beam is  $200 \mu\text{W}$  while the probe laser power is  $47 \mu\text{W}$  for both cases.

dipole trap, the atoms find it harder to come back to the starting position (both in real and momentum space).

#### 5.6.4 Probe scattering when the coupling laser is turned OFF first

Fig. 5.10 shows the comparison of the two cases showing different overlap durations between the probe and the coupling laser beams in time. Since the SL has a high directional scattering intensity compared to the normal BEC being illuminated by the probe laser alone, the SL scattered light must fall abruptly after the coupling beams are turned OFF. This is the case in both of the signals shown in Fig. 5.10. Both the signals go down in intensity after the coupling laser is extinguished but not very abruptly. This is because the AOM and the mechanical shutters still leak some coupling light while in the process of turning OFF and thus the lattice still exists for a while (weakened by the turning OFF process) and thus the intensity does not go down immediately.

As described in our upcoming paper, a fast switching of the probe laser while the lattice laser beams are ON can give us the fast superradiance decay of the SL. The small bump at around  $30 \mu\text{s}$  in the green curve (red circles) is probably noise.

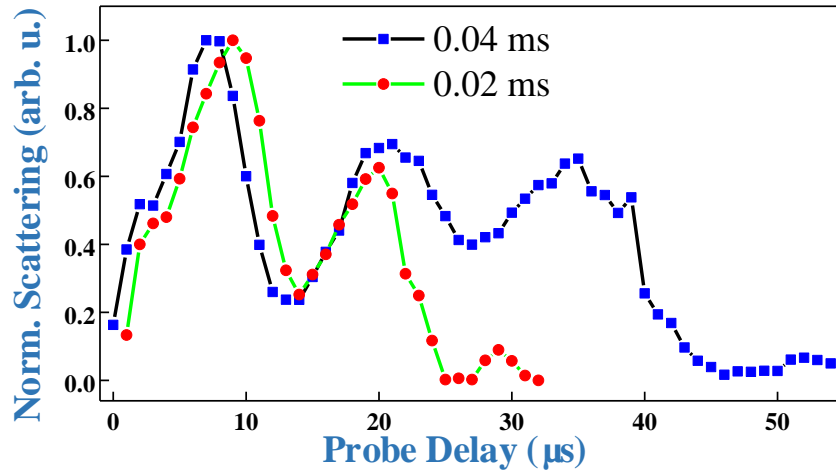


Figure 5.10. The fig. shows the SL scattering intensity vs probe delay when the coupling laser imprints a phase on the BEC but at later time is turned off while the probe scans the phase at different times. The coupling laser stays ON for 0.02 ms (circles) and 0.04 ms (squares) and is then turned OFF. The probe still turns ON for  $1 \mu\text{s}$  in each run of the experiment but at different delay time. The coupling laser power in each beam is  $200 \mu\text{W}$  while the probe laser power is  $47 \mu\text{W}$  for both cases.

### 5.6.7 Effect of different powers in the two lattice beams

Having a lattice in which the power of the two beams is different is similar to introducing a DC offset in the harmonic trap like lattice potential. This offset will not result in affecting the typical modulation of the BEC phase although it may lower the lattice potential due to this offset AC stark (or as said above, DC) force. Lowering the lattice potential means the oscillation period may be slightly changed from an otherwise same power beams lattice potential. This effect can be simulated in our lattice by reducing or increasing the power in one of the coupling beams. The effect will be the same and should not depend on whether C1 has a higher power or C2 has a higher power.

This effect is shown in Fig. 5.11(a). The higher and lower power beam is alternated between C1 and C2 but the oscillation is the same (this would not be the case when one of the beam is not as perfectly overlapped on the BEC as the other one. This also shows how both of our coupling beams are perfectly overlapped on the BEC).



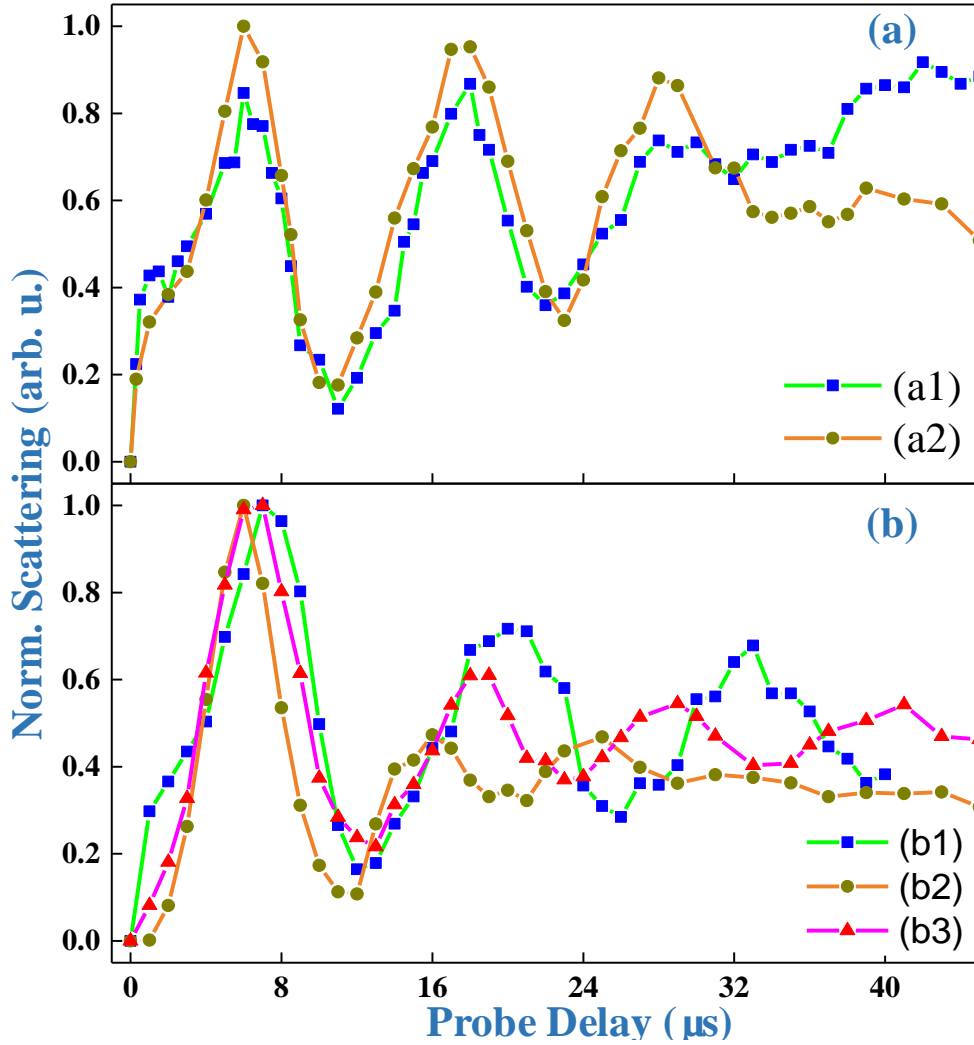


Figure 5.11. Dependence of the SL scattering signal on different powers of the coupling beams. (a) Shows a combination of (a1) coupling beams  $C1=200 \mu\text{W}$  and  $C2=400 \mu\text{W}$  (a2) a combination of  $C1=400 \mu\text{W}$  and  $C2=200 \mu\text{W}$ . Both schemes use the SL made by the 795 nm ( $^{87}\text{Rb}$  D1 line) coupling beams. The two signals shows the same oscillation frequency in the first 32  $\mu\text{s}$ . The data becomes noisy around at around 40  $\mu\text{s}$  due to increased spontaneous scattering. (b) When (b1) both  $C1$  and  $C2$  use 200  $\mu\text{W}$  of 795 nm laser (b2) both  $C1$  and  $C2$  use 200  $\mu\text{W}$  of 780 nm laser (D2 line of  $^{87}\text{Rb}$ ). (b3) When we use a double lattice with  $C1$  and  $C2$  each having 200  $\mu\text{W}$  power of 795 nm laser and 50  $\mu\text{W}$  of 780 nm laser. The 780 nm laser is locked by saturation absorption spectroscopy from  $F=1$  level to the  $F \simeq 2$  of the D2 line. The A1 peak frequency is used for the data in all the cases.

The signal of Fig. 5.10(b2) is recorded with 780 nm laser lattice only by sending this light in the coupling beams  $C1$  and  $C2$ . The probe laser frequency is slightly changed towards the atomic resonance from the peak A1 (still shifted from atomic resonance position

## Excitation spectrum and coherent phenomena in 87Rb Bose-Einstein condensates

due to the AC stark shift by the 780 nm lattice) as now there is no SL but just resonant spontaneous Bragg scattering of the probe light by the 780 nm lattice. The high density of the BEC may lead to some superradiance in the direction of the probe but the Bragg scattering direction (of light) now can't have superradiance as there is no coherent momentum chain as in SL. As discussed above, the 780 lattice also phase modulate the BEC and there are momentum states that satisfy the phase conservation condition and thus we have directional (Bragg) emission coming straight into the EMCCD without changing the position of the EMCCD or the probe.

The 780 nm lattice however makes a deeper lattice for the same 200  $\mu\text{W}$  of optical power and thus the oscillation frequency is higher than that of signal (b1) of the same figure having 795 nm lattice at 200  $\mu\text{W}$  optical power.

Combining the two lattices (50  $\mu\text{W}$  of 780 nm and 200  $\mu\text{W}$  of 795 nm, sent through the same C1 and C2 beams via optical fiber) results in a super-lattice with complex potential that is deeper than the 795 nm lattice but shallower than the only 780 nm lattice at 200  $\mu\text{W}$  and thus the oscillation frequency of the SL scattered light is in between the other two (between that of b1 and b2). This is a very interesting result and can be used to measure the depths of even more complex lattice potentials. Lattices of two and three dimensions can be probed very precisely using this probe delay technique.

The data presented in Fig. 5.12 shows similar phase modulation of the BEC phase by a 1064 nm lattice at two different powers. This lattice was made by retro-reflecting a single 1064 nm laser beam and shining the probe beam making an angle of  $41^\circ$  with the direction of the 1064 nm lattice beam. The scattered light from this lattice is recorded with the EMCCD now placed at  $-41^\circ$  angle to the 1064 nm lattice beam. We have observed that the scattering intensity of the probe in the 1064 nm lattice is very low due to optical pumping of the atoms to the low hyperfine state by the probe laser and thus used a far red detuned frequency (-700 MHz below the given hyperfine transition) to collect a reasonable amount of scattering (in the 780 nm lattice the 780 nm laser acts as a repumper also so this problem is not present in that lattice).

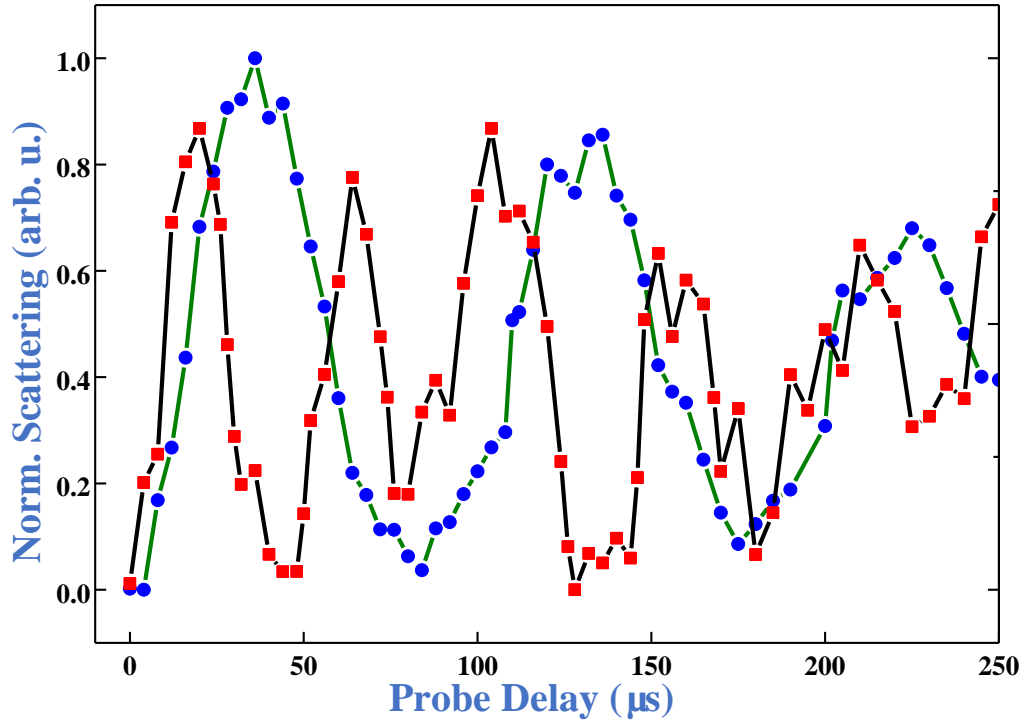


Figure 5.12. The oscillations of the scattering intensity recorded in a 1064 nm lattice at two different lattice laser powers. The blue circles data is recorded with a lattice power of 220 mW while the red squares data was recorded with a 600 mW power. The probe laser frequency was kept at -700 MHz below the  $F \simeq 1$  transition.

However, the use of the different frequency does not affect the observation of the oscillations in the scattering intensity.

### 5.6.8 Effect of moving lattice

So far we have been using static lattices in the position space. The minima and maxima of a static potential stays fixed in the position space. A moving lattice can be created by the introduction of a detuning between the two lattice/coupling beam frequencies (by first passing each beam in a separate AOM operating at different RF frequency). The static lattice can scatter atoms from the zero momentum state into momentum states of even order but the moving lattice can scatter them into both odd and even order momentum states<sup>[22]</sup>. It means that the number of momentum states increases in a moving lattice without increasing the power of the coupling beams and we expect an increase in the oscillation frequency of the SL scattering signal in the moving lattice. This increase of the oscillation frequency with

increase in mutual detuning of the coupling beams is present in the experimental data shown in Fig. 5.13 (a).

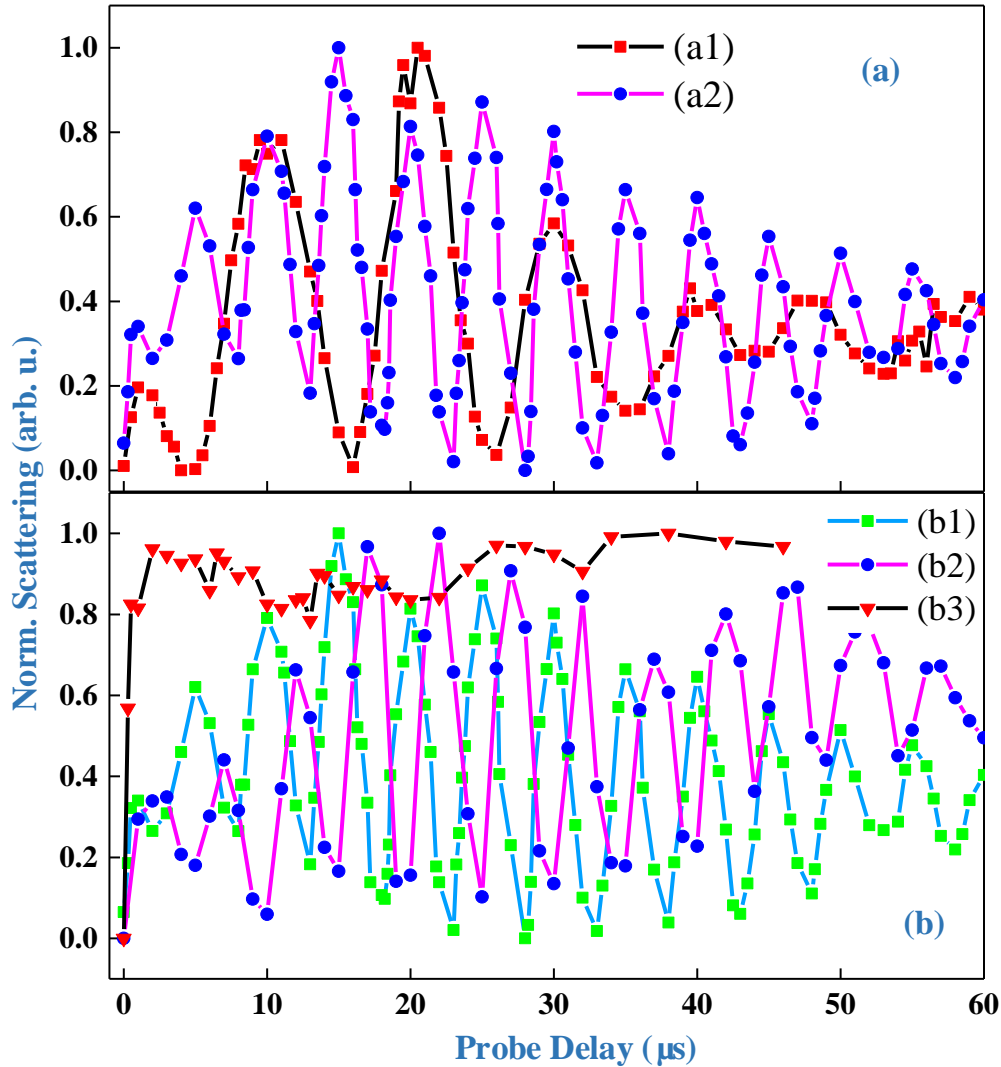


Figure 5.13. The effect of mutual detuning of coupling beams on the oscillation frequency. (a1) C1 is detuned by  $+0.05\text{MHz}$  and C2 by  $-0.05\text{MHz}$  from the resonance. (a2) C1 is detuned by  $+0.1\text{MHz}$  and C2 by  $-0.1\text{MHz}$ . (b) The effect of reversing the sign of the detuning (b1) when C1 is detuned by  $+0.1\text{MHz}$  and C2 by  $-0.1\text{MHz}$  (b2) C1 is detuned by  $-0.1\text{MHz}$  and C2 by  $+0.1\text{MHz}$ . The time lag between (b1) and (b2) is clearly visible. (b3) C1 is detuned by  $+22\text{MHz}$  and C2 by  $-22\text{MHz}$ . Probe power is  $47\text{ }\mu\text{W}$  at peak frequency A1 and coupling power is  $200\text{ }\mu\text{W}$  in all the cases.

Using the same magnitude detuning combination but reversing its sign in the two lattice beams C1 and C2 (shown in Fig. 5.13(b1, b2)) shows an interesting feature. The

## Chapter 5: Temporal dynamics of BEC in a 1D Optical Lattice

oscillation frequency in each case stays the same which means that the phase imprinted by the moving lattices in both cases on the BEC wave function is the same. But the two configurations also show a temporal lag (temporal phase) right from the start in the two oscillation signals which could be a characteristic of the SL lattice responding differently to moving lattices in different directions. This initial lag stays the same way till the end of the signal until the signal becomes very small and noisy.

The speed of a moving lattice in any particular direction is given by  $\frac{\delta}{k}$ , where  $\delta$  is the magnitude of the detuning between the two coupling beams and  $k$  is the wavenumber of the coupling laser. The detuning in Fig. 5.13(a1, a2, b1, b2) can produce lattices moving at the slower speeds of  $0.12 \mu\text{m}/\mu\text{s}$  and  $0.25 \mu\text{m}/\mu\text{s}$ . This means that the moving lattice recovers to its original shape (in position space) after moving for a time  $\frac{\pi}{\delta}$  of  $3.14 \mu\text{s}$  and  $1.57 \mu\text{s}$  respectively<sup>[34]</sup> (the lattice maxima and minima recovers, not the superradiant momentum state population!). But at higher mutual detuning of the coupling beams (as in Fig. 5.13(b3)), the lattice speed increases to  $5.57 \mu\text{m}/\mu\text{s}$  and the lattice recovery time reduces to just  $71 \text{ ns}$ . The atoms experience a very fast varying potential. Such fast phase modulation of the BEC wave function is not possible to observe at the time resolution our setup employs currently. The signal of Fig. 5.13(b3) stays the same (apart from the initial increase of the SL scattering) due to this fast moving lattice and the atoms seems to not feel any potential at the timescale we are using. The initial increase in the SL scattering intensity in the first two or three  $\mu\text{s}$  is common among all the figures and it is due to the fact that the coupling laser is being in the turn ON phase (the AOMs and the mechanical shutters are in the process of turning ON).

In all of these figures of the experimental data presented in this chapter, the visibility of the oscillations decay for large lattice application times and this kind behavior is also observed in the data of Ref.<sup>[22]</sup> in which they attributed it to inhomogeneity of the lattice beams and the power fluctuations in each run.

### 5.7 Summary

In this chapter the use of the SL was discussed for the probing of the dynamics of the BEC wave function modulated by an optical lattice in the Kapitza-Dirac regime. The

## Excitation spectrum and coherent phenomena in $^{87}\text{Rb}$ Bose-Einstein condensates

concepts of BEC phase modulation was briefly discussed, and also the superradiance phenomenon in a large cloud of atoms and also in the superradiance lattice was discussed. The use of the SL technique is beneficial for studying of such small phase modulations that need higher free fall times in the absorption imaging methods of measurements but the SL can study them in-situ. Not only this but also the SL technique avoids the various sources of noise typical of the absorption imaging technique. The same SL can be used in the future for high speed moving lattices and their effects on the BEC wave function. The complex lattice potential depths can be very easily measured using this time delay technique. The observation of the relative phase between the different density of states with time delay is a new feature and that should be considered when studying superradiance lattices in already modulated BECs. The effects like BEC phase modulation by optical lattice inside and outside the optical dipole trap and the subsequent superradiance gives insight into the helping role of the trapping potential in the re-population of the different momentum states after its phase modulation by the Kapitza-Dirac pulses. It was also seen that the moving lattices in different directions with same speed had a constant phase lag but the oscillation frequency was not affected by the direction of the motion of the lattice. These findings are of great importance for the field of optical lattices in BECs and would definitely help the future adaptation of the optical lattices in different practical applications.

## References

- [1] M. Kozuma, L. Deng, E. W. Hagley, J. Wen, R. Lutwak, K. Helmerson, S. L. Rolston, and W. D. Phillips. Coherent Splitting of Bose-Einstein Condensed Atoms with Optically Induced Bragg Diffraction. *Phys. Rev. Lett.*, 1999, 82, 871.
- [2] J. Stenger, S. Inouye, A. P. Chikkatur, D. M. Stamper-Kurn, D. E. Pritchard, and W. Ketterle. Bragg Spectroscopy of a Bose-Einstein Condensate. *Phys. Rev. Lett.*, 1999, 82, 4569.
- [3] Y. B. Ovchinnikov, J. H. Müller, M. R. Doery, E. J. D. Vredenbregt, K. Helmerson, S. L. Rolston, and W. D. Phillips. Diffraction of a Released Bose-Einstein Condensate by a Pulsed Standing Light Wave. *Phys. Rev. Lett.*, 1999, 83, 284.
- [4] P. Verkerk, B. Lounis, C. Salomon, C. Cohen-Tannoudji, J.-Y. Courtois, and G. Grynberg. Dynamics and spatial order of cold cesium atoms in a periodic optical potential. *Phys. Rev. Lett.*, 1992, 68, 3861.
- [5] P. S. Jessen, C. Gerz, P. D. Lett, W. D. Phillips, S. L. Rolston, R. J. C. Spreeuw, and C. I. Westbrook. Observation of quantized motion of Rb atoms in an optical field. *Phys. Rev. Lett.*, 1992, 69, 49.
- [6] A. Hemmerich and T. W. Hänsch. Two-dimensional atomic crystal bound by light. *Phys. Rev. Lett.*, 1993, 70, 410.
- [7] G. Birkl, M. Gatzke, I. H. Deutsch, S. L. Rolston, and W. D. Phillips. Bragg Scattering from Atoms in Optical Lattices. *Phys. Rev. Lett.*, 1995, 75, 2823.
- [8] K. Wen, Z. Meng, P. Wang, L. Wang, L. Chen, L. Huang, L. Zhou, X. Cui, and J. Zhang. Observation of sub-wavelength phase structure of matter wave with two-dimensional optical lattice by Kapitza-Dirac diffraction. *Scientific Reports*, 2020, 10, 5870.
- [9] H. Son, J. J. Park, W. Ketterle, and A. O. Jamison. Collisional cooling of ultracold molecules. *Nature*, 2020, 580, 197.
- [10] W. S. Bakr, A. Peng, M. E. Tai, R. Ma, J. Simon, J. I. Gillen, S. Fölling, L. Pollet, and M. Greiner. Probing the Superfluid-to-Mott Insulator Transition at the Single-Atom Level. *Science*, 2010, 329, 547.
- [11] W. S. Bakr, J. I. Gillen, A. Peng, S. Fölling, and M. Greiner. A quantum gas microscope for detecting single atoms in a Hubbard-regime optical lattice. *Nature*, 2009, 462, 74.

- [12] D. Jaksch, C. Bruder, J. I. Cirac, C. W. Gardiner, and P. Zoller. Cold bosonic atoms in optical lattices. *Phys. Rev. Lett.*, 1998, 81, 3108.
- [13] R. Jördens, N. Strohmaier, K. Günter, H. Moritz, and T. Esslinger. A Mott insulator of fermionic atoms in an optical lattice. *Nature*, 2008, 455, 204.
- [14] P. B. Blakie and J. V. Porto. Adiabatic loading of bosons into optical lattices. *Phys. Rev. A*, 2004, 69, 013603.
- [15] U. Schneider, L. Hackermüller, S. Will, Th. Best, I. Bloch, T. A. Costi, R. W. Helmes, D. Rasch, and A. Rosch. Metallic and Insulating Phases of Repulsively Interacting Fermions in a 3D Optical Lattice. *Science*, 2008, 322, 1520.
- [16] L. Tarruell, D. Greif, T. Uehlinger, Gr. Jotzu, and T. Esslinger. Creating, moving and merging Dirac points with a Fermi gas in a tunable honeycomb lattice. *Nature*, 2012, 483, 302.
- [17] E. Toth, A.M. Rey, and P. B. Blakie. Theory of correlations between ultracold bosons released from an optical lattice. *Phys. Rev. A*, 2008, 78, 013627.
- [18] G. Wirth, M. Ölschläger, and A. Hemmerich. Evidence for orbital superfluidity in the P-band of a bipartite optical square lattice. *Nature Phys.*, 2011 7, 147.
- [19] G. E. Marti, R. B. Hutson, A. Goban, S. L. Campbell, N. Poli, and J. Ye. Imaging Optical Frequencies with 100  $\mu\text{Hz}$  Precision and 1.1  $\mu\text{m}$  Resolution. *Phys. Rev. Lett.*, 2018, 120, 103201.
- [20] M. Takamoto, F. Hong, R. Higashi, and H. Katori. An optical lattice clock. *Nature*, 2005, 435, 321.
- [21] W. F. McGrew, X. Zhang, R. J. Fasano, S. A. Schäffer, K. Beloy, D. Nicolodi, R. C. Brown, N. Hinkley, G. Milani, M. Schioppo, T. H. Yoon, and A. D. Ludlow. Atomic clock performance enabling geodesy below the centimetre level. *Nature*, 2018, 564, 87.
- [22] J. H. Denschlag, J. E. Simsarian, H. Haffner, C. McKenzie, A. Browaeys, D. Cho, K. Helmerson, S. L. Rolston, and a.W.D. Phillips. A Bose-Einstein condensate in an optical lattice. *J. Phys. B: At. Mol. Opt. Phys.*, 2002, 35, 3095.
- [23] S. Gupta, A. E. Leanhardt, A. D. Cronin, and D. E. Pritchard. Coherent manipulation of atoms with standing light waves. *C. R. Acad. Sci.*, 2001, 2, 479.



- [24] B. Gadway, D. Pertot, R. Reimann, M. G. Cohen, and D. Schneble. Analysis of Kapitza-Dirac diffraction patterns beyond the Raman-Nath regime. *Optics Express*, 2009, 17, 19173.
- [25] J. H. Huckans, I. B. Spielman, B. Laburthe Tolra, W. D. Phillips, and J. V. Porto. Quantum and classical dynamics of a Bose-Einstein condensate in a large-period optical lattice. *Phys. Rev. A*, 2009, 80, 043609.
- [26] R. H. Dicke. Coherence in Spontaneous Radiation Processes. *Phys. Rev.*, 1954, 93, 99.
- [27] N. Skribanowitz, I. P. Herman, J. C. MacGillivray, and M. S. Feld. Observation of Dicke Superradiance in Optically Pumped HF Gas. *Phys. Rev. Lett.*, 1973, 30, 309.
- [28] R. G. DeVoe and R. G. Brewer. Observation of Superradiant and Subradiant Spontaneous Emission of Two Trapped Ions. *Phys. Rev. Lett.*, 1996, 76, 2049.
- [29] A. Goban, C. Hung., J. D. Hood, S. Yu, J. A. Muniz, O. Painter, and H. J. Kimble. Superradiance for Atoms Trapped along a Photonic Crystal Waveguide. *Phys. Rev. Lett.*, 2015, 115, 063601.
- [30] S. Inouye, A. P. Chikkatur, D. M. Stamper-Kurn, J. Stenger, D. E. Pritchard, and W. Ketterle. Superradiant Rayleigh Scattering from a Bose-Einstein Condensate. *Science*, 1999, 285, 571.
- [31] K. Baumann, C. Guerlin, F. Brennecke, and T. Esslinger. Dicke quantum phase transition with a superfluid gas in an optical cavity. *Nature*, 2010, 464, 1301.
- [32] M. O. Scully, E. S. Fry, C. H. Raymond Ooi, and K. Wołkiewicz. Directed Spontaneous Emission from an Extended Ensemble of  $N$  Atoms: Timing Is Everything. *Phys. Rev. Lett.*, 2006, 96, 010501.
- [33] D. Das, B. Lemberger, and D. D. Yavuz. Subradiance and superradiance-to-subradiance transition in dilute atomic clouds. *Phys. Rev. A*, 2020, 102, 043708.
- [34] D. Wang, R. Liu, S. Zhu, and M. O. Scully. Superradiance Lattice. *Phys. Rev. Lett.*, 2015, 114, 043602.
- [35] L. Chen, P. Wang, Z. Meng, L. Huang, H. Cai, D. Wang, S. Zhu, and J. Zhang. Experimental Observation of One-Dimensional Superradiance Lattices in Ultracold Atoms. *Phys. Rev. Lett.*, 2018, 120, 193601.

## Excitation spectrum and coherent phenomena in $^{87}\text{Rb}$ Bose-Einstein condensates

- [36] P. Wang, L. Chen, C. Mi, Z. Meng, L. Huang, K. S. Nawaz, H. Cai, D. Wang, S. Zhu, and J. Zhang. Synthesized magnetic field of a sawtooth superradiance lattice in Bose Einstein condensates. *npj Quantum Inf.*, 2020, 6, 18.
- [37] M. A. Kristensen, M. B. Christensen, M. Gajdacz, M. Iglicki, K. Pawłowski, C. Klempt, J. F. Sherson, K. Rz, a`zewski, A. J. Hilliard, and J. J. Arlt. Observation of Atom Number Fluctuations in a Bose-Einstein Condensate. *Phys. Rev. Lett.*, 2019, 122, 163601.
- [38] H. Chen, D. Xiong, P. Wang, and J. Zhang. Pulse loading  $^{87}\text{Rb}$  Bose-Einstein condensation in optical lattice: the Kapitza-Dirac scattering and temporal matter-wave dispersion Talbot effect. *Chin. Opt. Lett.*, 2010, 8, 348.

## Appendix A

### A.1 Biasing Circuit for IGBT

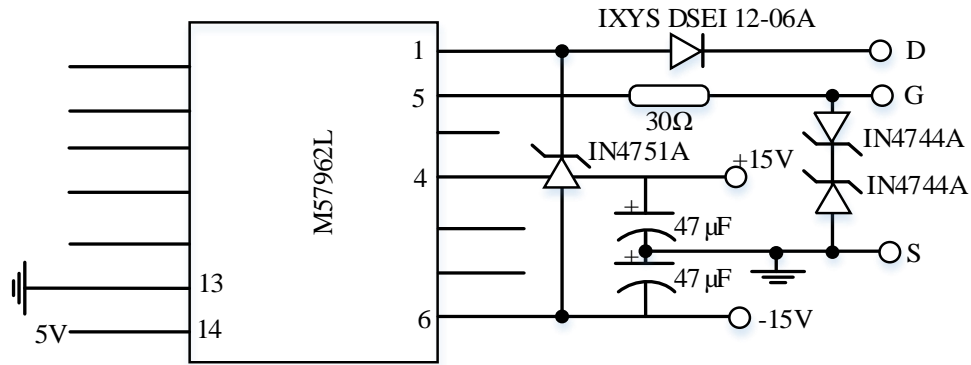


Figure A.1 The circuit for turning ON and OFF the IGBT switches which in turn controls the current in the dual MOT/Feshbach coils.

### A.2 Adder Circuit

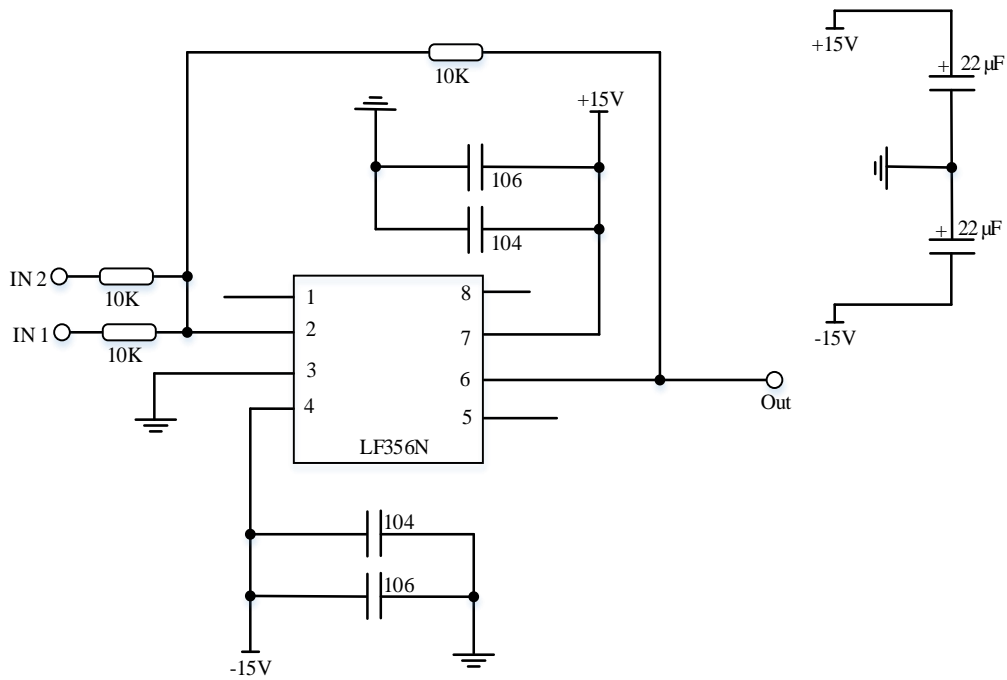


Figure A.2. The adder circuit used to add the signal from the Lock-in amplifier (in KHz) to the signal from the RF driver (POS-PAS) (in MHz) in the SAS setup.

### A.3 Feedback Circuit

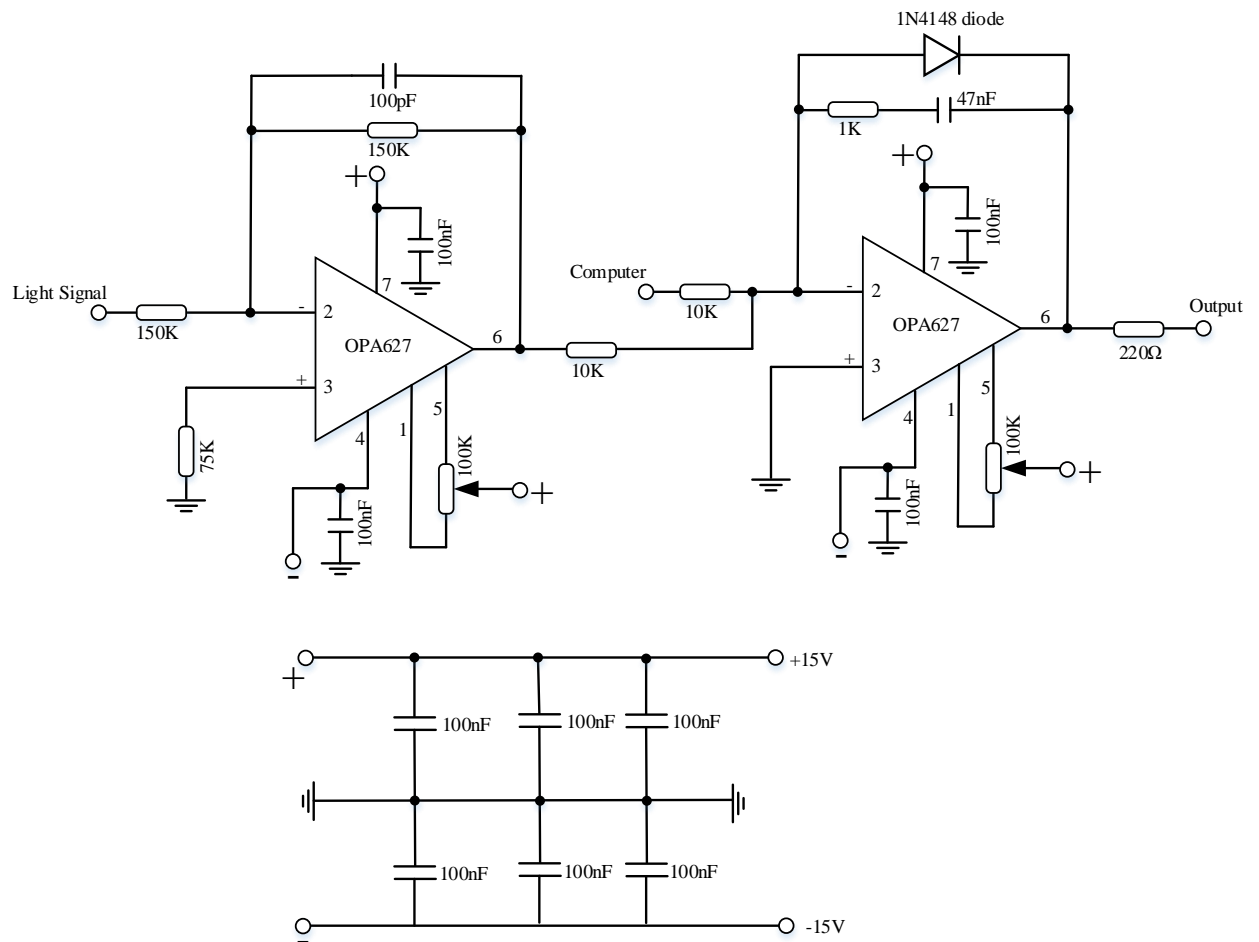


Figure A.3 The feedback circuit used to control the depth of the dipole trap by controlling the power in each dipole trap beam. The output in this schematic goes to the PAS-300+ of the RF driver (POS-PAS) circuit.

**A.4 Circuit for AOM switch ON/OFF**

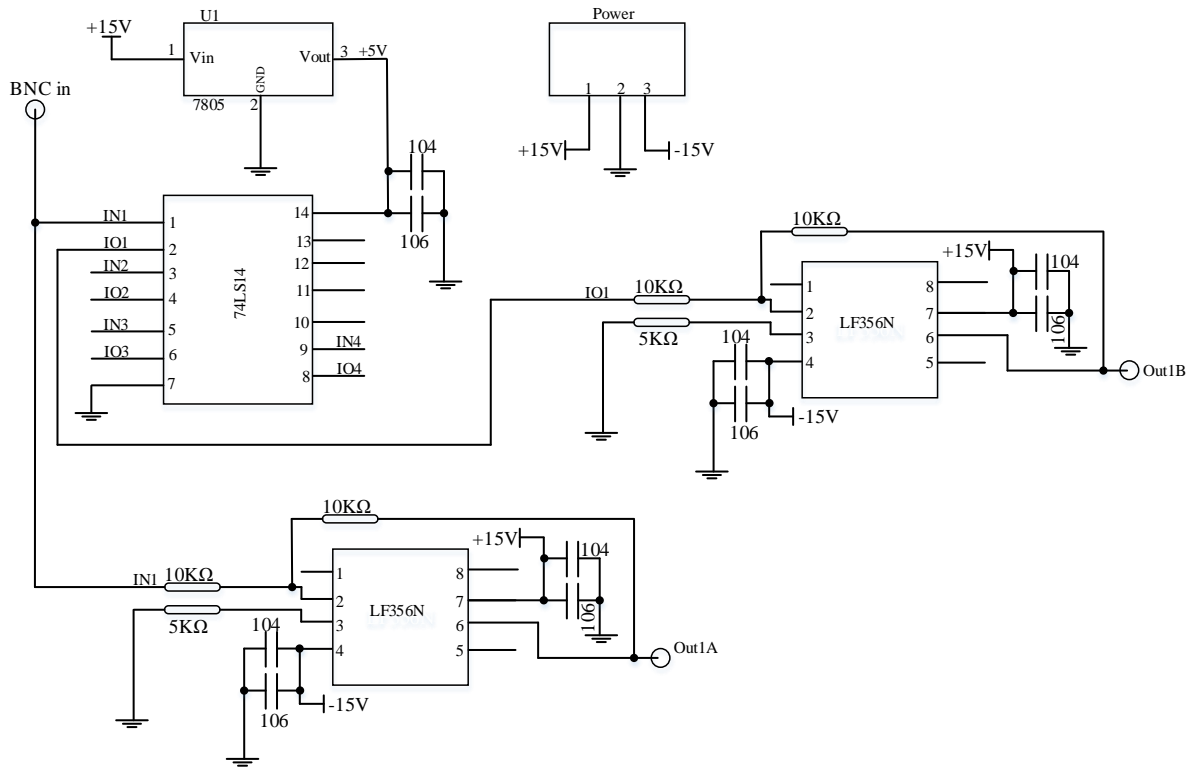


Figure A.4 The logic circuit for turning ON/OFF the RF signal fed to the AOMs using the Mini Circuits switch. This circuits converts the single ON/OFF signal brought by a BNC line into two ON/OFF voltage signals as required by the Mini Circuits switch.

### A.5 Circuit for Analog Optical Isolator/Analog box

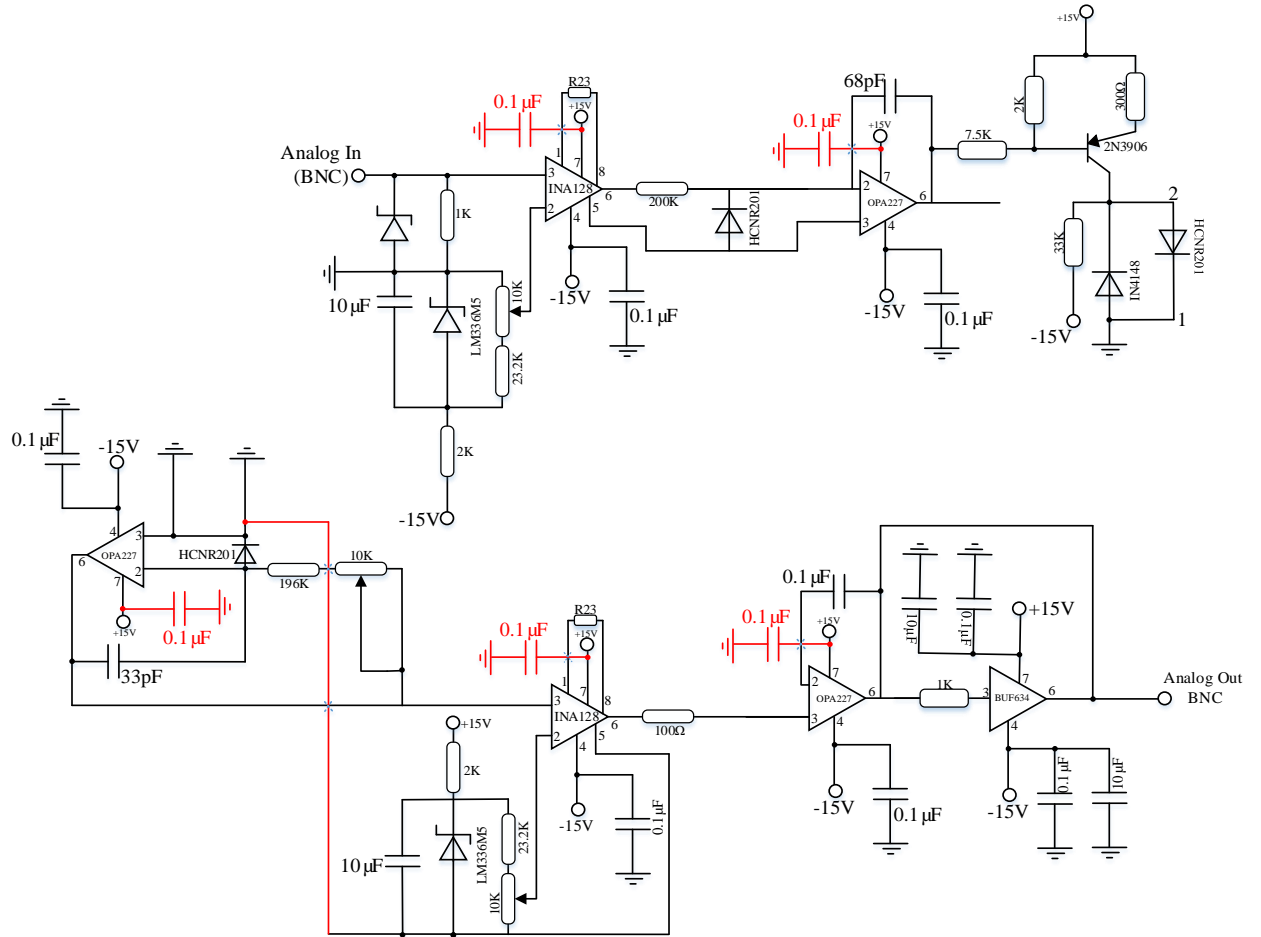


Figure A.6 This circuit isolates the computer (Control PC) from the high voltage devices during sending the programming signal. The programming analog signal of power supplies is first fed into this circuit and from here it is sent to these destinations. The signal used to actively control the amplitude or frequency of the RF driver (POS-PAS) circuit does not need to be first sent to this isolator box and can be directly sent from the Control PC analog output pins.

**A.6 Optical setup**

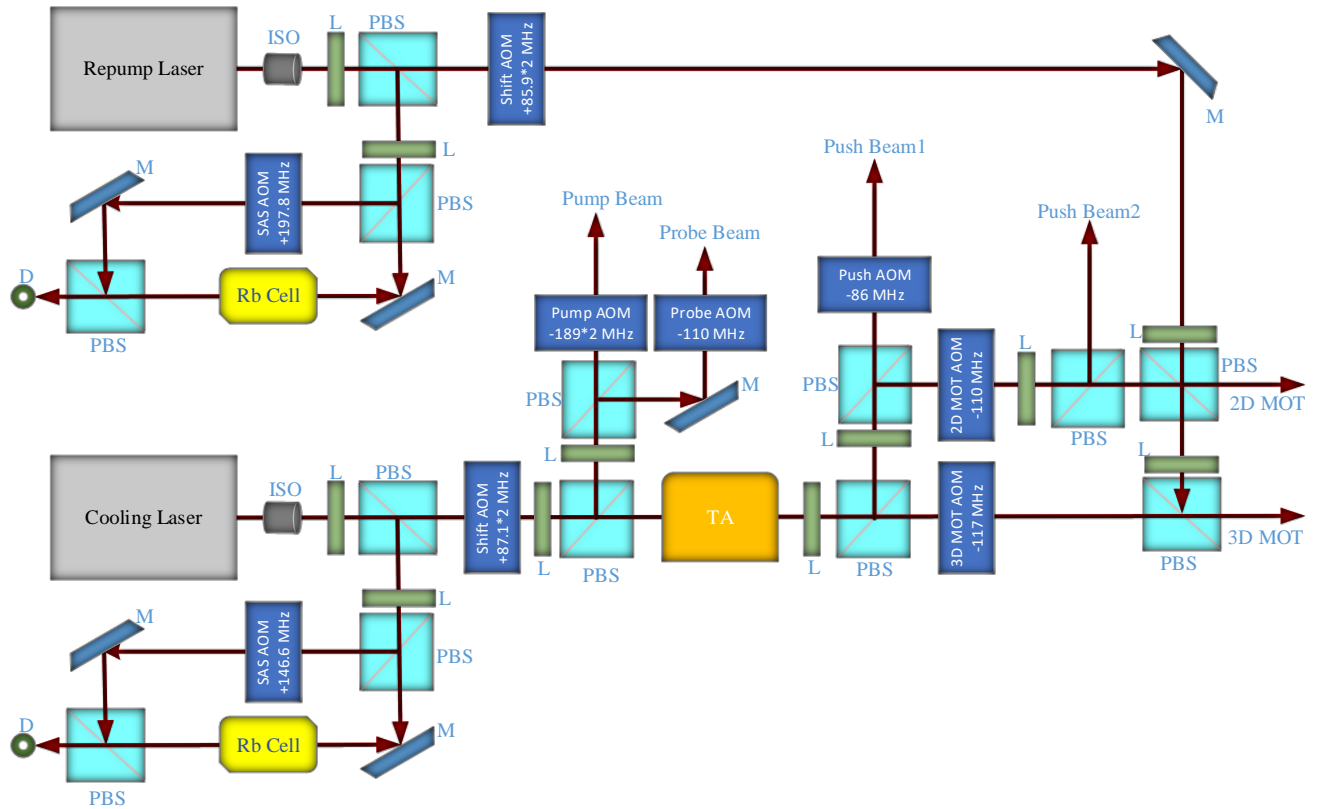


Figure A.7 The optical setup for the various laser beams and their frequencies tuning sequence needed during the preparation of the BEC.

### A.7 RF driver (POS-PAS) circuit

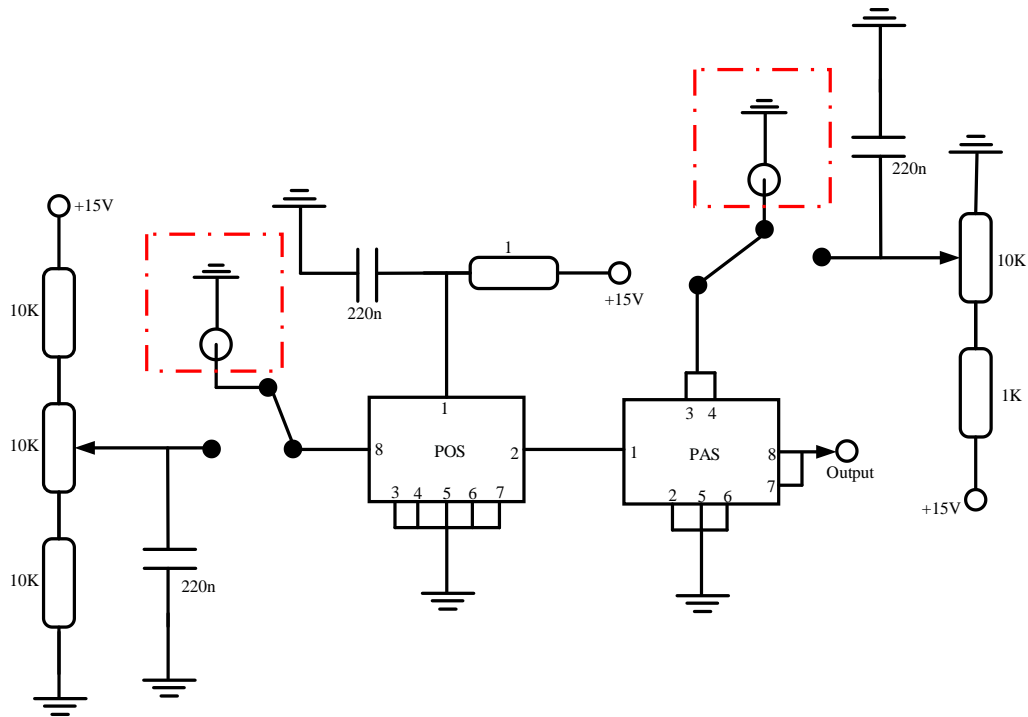


Figure A.8 The AOM RF Driver circuit that we label as the POS-PAS circuit in the thesis. The red dashed-dotted squares shows the computer programmable (or potentiometer tuning) option of the POS and PAS input pins.



# Appendix A

## A.8 PID for laser locking

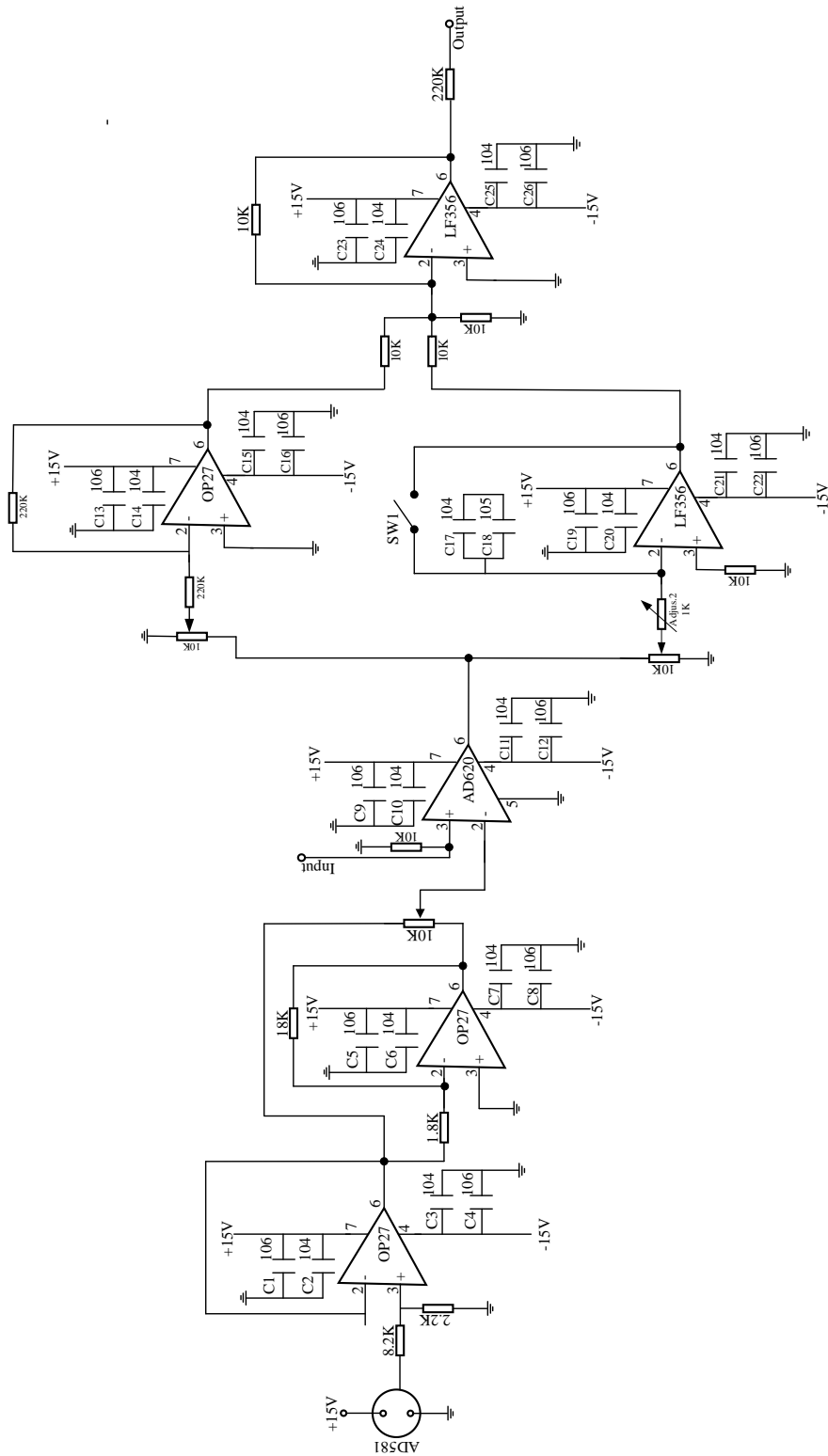


Figure A.9 The PID circuit used in our lab for locking the ECDL lasers via the SAS.

### A.9 Detector

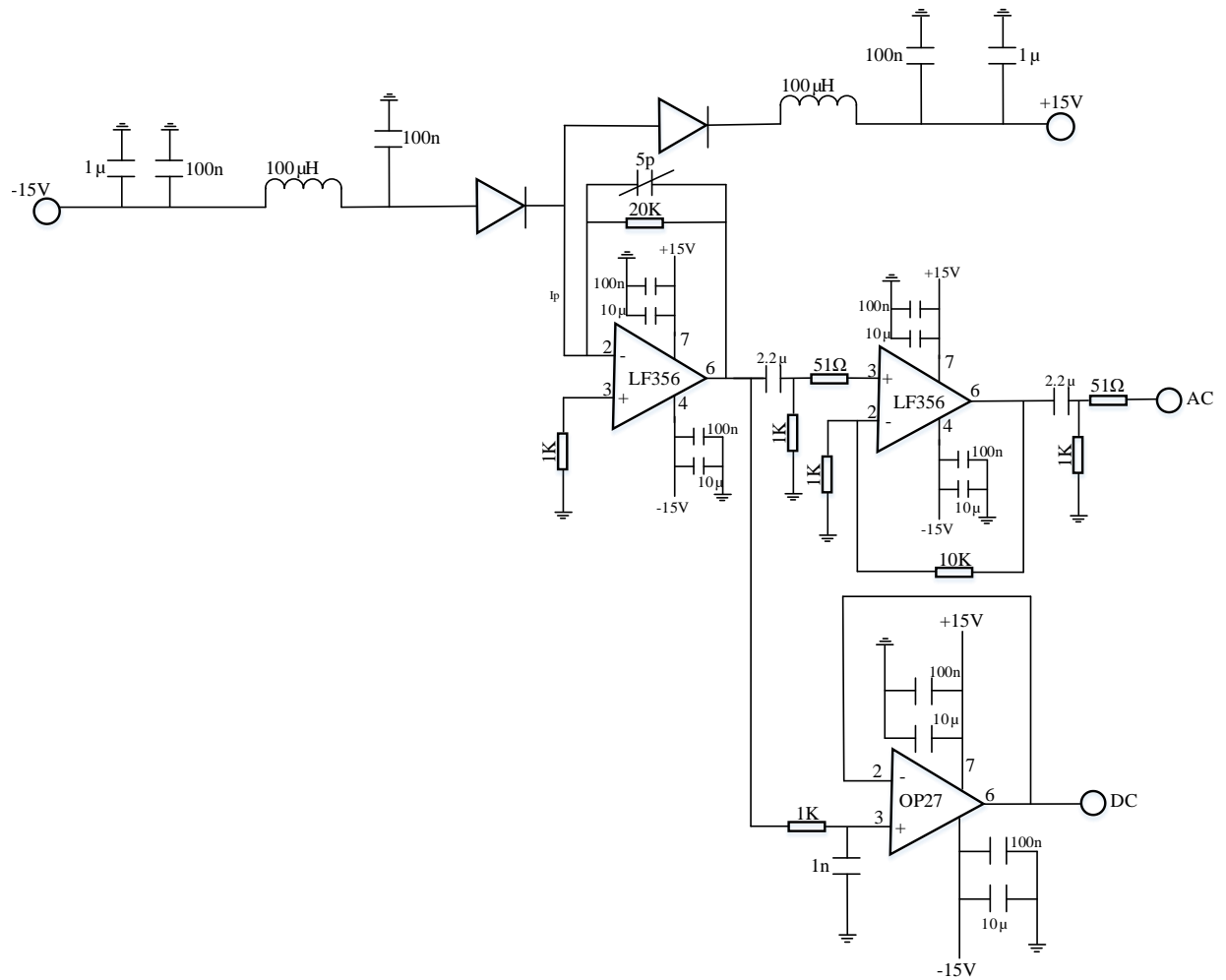


Figure A.10 The detector circuit used in the SAS and the feedback setups of the experiments.

**A.10 OPLL Schematic**

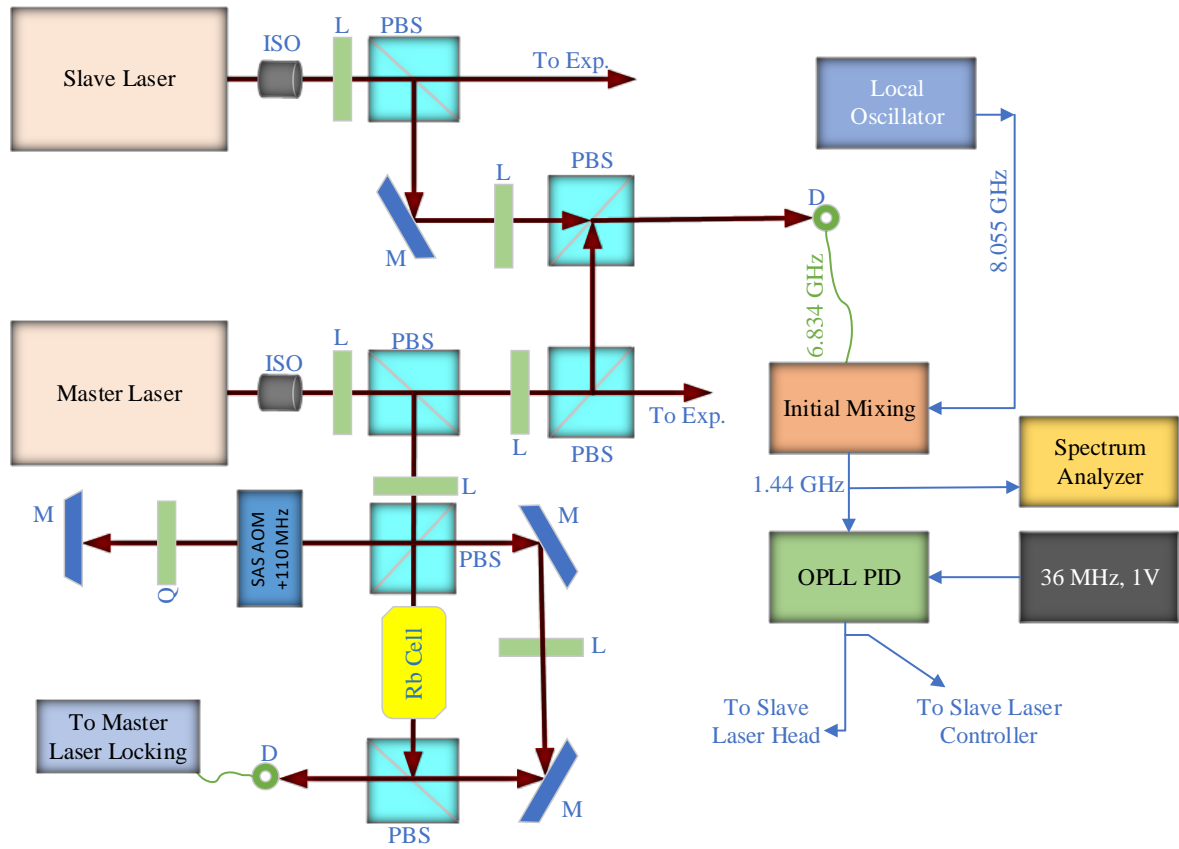


Figure A.11 The OPLL optical and MW/RF components block diagram setup used to lock the two ECDL lasers in master-slave configuration and scan the slave laser frequency.

### A.11 Circuit for Digital Optical Isolator/Digital Box

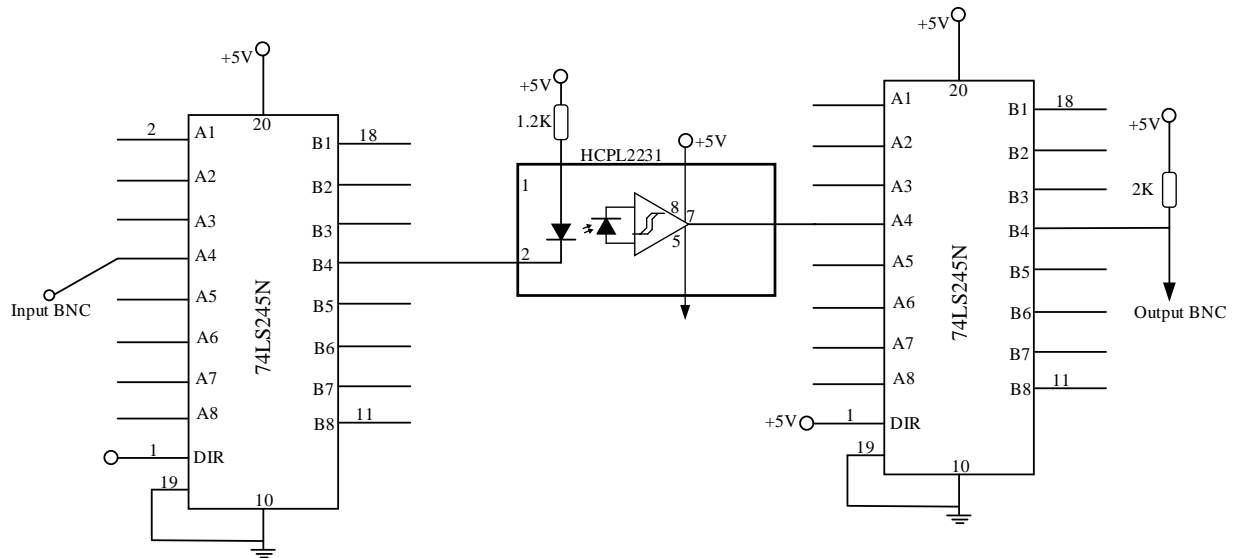


Figure A.12 The optical isolator circuit for isolating the Control PC from the high voltage devices through the digital output pins. The IGBT switches are turned ON/OFF using the digital pins of the Control PC which are first fed into this isolator and later are sent to the IGBT control box. Similarly the control signal for the switch ON/OFF of the AOMs via the Mini Circuits switch is also sent after passing through this circuit.

**A.12 Amplifier circuit for shutter ON/OFF**

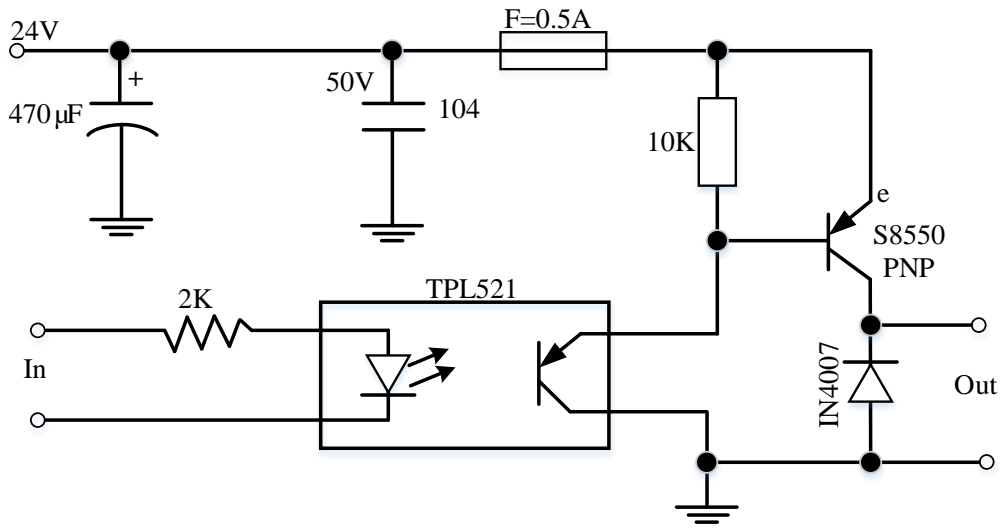


Figure A.13 The shutter control box that amplifies the digital box output and turns ON and OFF the shutter.

## Summary and outlook

In this thesis, I have discussed briefly the theoretical and experimental topics needed to create the BEC. Later, I have discussed the use of  $^{87}\text{Rb}$  BEC for the simulation of an N-type system using three laser beams. The N-type system is studied with the help of absorption imaging technique and the number of atoms left after exposure to the three experimental laser beams (making the N-type system) are counted. Several interesting features of the N-type system are retrieved using the absorption imaging technique. Some of the findings, especially the behavior of the N-type system when the polarizations of the coupling and the driving lasers are rotated still needs some theoretical modeling which can be a future work.

Next is the study of the creation of the excited state weakly bound  $^{87}\text{Rb}$  dimers via photoassociation. Not only new, previously undetected quantized states are produced and detected in the BEC but also some of their properties are studied using different detection techniques. The most important property of these states is their role in the mixing with the atomic resonance and changing the atomic resonance line-shape even at modest laser powers. This mixing is very important in the theoretical modeling of the coherent systems in the future (systems such as the N-type system or the lambda-type systems). Another point is that we don't know for sure to which potential energy curve these newly discovered excited molecular states belong. The tagging of these states with exact vibrational quantum numbers is the next step of this work. This finding will indeed draw a lot of attention from the theoretical physics community as these nearby states can accurately tell about the extent of hyperfine mixing in the otherwise  $1/R^3$  type potential energy curve.

The last study was related to the phase retrieval of the BEC phase using the superradiance lattice scattering. The in-situ technique of reading the BEC phase when it's acted upon by one or more lattices for a variable time is promising as we have demonstrated in the thesis. The exact strengths of the lattice beams can be measured using this technique

## Summary and outlook

no matter how many lattices are acting on the BEC provided we have an accurate knowledge of the angles between these lattices. The other finding in this study is that the population of the superradiance lattice different bands is not recovered simultaneously at the same rate and this needs more experimental and theoretical verification.

## Research achievements

1. **Khan Sadiq Nawaz**, Liangchao Chen, Chengdong Mi, Zengming Meng, Lianghai Huang, Pengjun Wang, and Jing Zhang. Photoassociation spectroscopy of weakly bound  $^{87}\text{Rb}_2$  molecules near the  $5P_{1/2} + 5S_{1/2}$  threshold by optical Bragg scattering in Bose-Einstein condensates, *Phys. Rev. A*, 2020, 102, 053326.
2. Pengjun Wang, Liangchao Chen, Chengdong Mi, Zengming Meng, Lianghai Huang, **Khan Sadiq Nawaz**, Han Cai, Da-Wei Wang, Shi-Yao Zhu and Jing Zhang. Synthesized magnetic field of a sawtooth superradiance lattice in Bose-Einstein condensates, *npj Quantum Information*, (2020) 6, 18.
3. **Khan Sadiq Nawaz**, Cheng-Dong Mi, Liang-Chao Chen, Peng-Jun Wang, Jing Zhang. Experimental Investigation of the Electromagnetically Induced-Absorption-Like Effect for an N-Type Energy Level in a Rubidium BEC, *CHIN. PHYS. LETT.*, 2019, 36, 043201.
4. Zhenlian Shi, Ziliang Li, Pengjun Wang, **Khan Sadiq Nawaz**, Liangchao Chen, Chengdong Mi, Zengming Meng, Lianghai Huang, and Jing Zhang. Production  $^{23}\text{Na}$  Bose-Einstein condensates in the  $F=2$  state using  $\text{D}_2$  gray molasses, *JOSA B*, 2021, 38, 1229.
5. Cheng-Dong Mi, **Khan Sadiq Nawaz**, Peng-Jun Wang, Liang-Chao Chen, Lianghai Huang, and Jing Zhang. Production of dual species Bose-Einstein condensates of  $^{39}\text{K}$  and  $^{87}\text{Rb}$ , *CHIN. PHYS. B*, 2021 (s <https://doi.org/10.1088/1674-1056/abee6d>).



## Acknowledgments

### **Acknowledgments**

First of all I thank my supervisor Professor Zhang Jing for providing me the opportunity to work in his lab as his first international student. The facilities and working environment he provided was great and it is here in his lab that I learned about the secret to the development of China at such an unprecedented pace. And the secret is hard work and more hard work. Professor Zhang not only himself has dedicated all his efforts to the hard work but he also expects his students to do the same. Coming from a different working environment, it was very difficult for me in the beginning to adopt to the new environment but in a month or two I finally tuned myself to the Chinese style of doing hard work. Professor Zhang gave me enough time to fully integrate into the group. The language barrier was also a real issue and my senior and now Dr. Liangchao Chen helped me a lot to understand the basic science and technology behind the BEC apparatus. He always encouraged me to ask questions and also help me a lot in the beginner's literature. But he graduated very soon and from there I was greatly supported by Mi Chengdong. We both were new students so we used to ask a lot of questions from each other that benefitted both of us. Mi Chengdong was the first of my lab mates who introduced me to Chinese food and to the Chinese culture in general. I wish him a great success in his future and an early graduation next year. The next person I would like to thank is Professor Wang Pungjun who always helped me in understanding a lot of difficult topics especially related to electronics and to computer control of the experiment. He always gave me time to discuss any difficulty that I faced during the four year time that I spent here. Our lab hosts several groups working on almost similar setups and it was really helpful to interact with the students working on these setups. Wen Kai (coldKevin) was one of the senior students from whom I learned a lot. He always agreed to share his expertise with me during the free time. He is also a genius in computer and software related subjects and he always solved our computer and internet related problems. Next I would like to mention is Li Ziliang who knew everything related to the experimental setup. He always offered help in solving my problems. I am very thankful to him for his help. I would also like to pay special thanks to Shahjee Khan who accompanied me during the hard times of lockdown during the corona pandemic and stayed

## Acknowledgments

with me in the hospital for almost a month. There are not enough words to describe my gratefulness to him. I am also very thankful to Professor Yu Xudong for all the help he offered both regarding the technical and also the administrative matters in the institute. He has such a wonderful, and always welcoming personality and always put a welcoming smile on his face. I would also like to say special thanks to Professor Meng Zengming. He always treated me and Shah Jee Rahman with great love and consistently shared the mooncake celebrations with us. Another great faculty member that I would like to thank is Professor Lianghui Huang. He is a wonderful person and he always offered his help to me both in technical and also in the outside world. In the end, I would like to thank Yang Guangyu, Shi Zhenlian, Wang Liangwei, Jin Yuanbin, Liu Fangde, Wang Jiangwei, Zhou Fang, Li Donghao, Bian Guoqi, Nie Liang, Zhang Yue, Miao Jie, Li Yunda (the photographer) and all the young guys and the administration at the institute especially Teacher Qu for their help. I am also thankful to the Chinese scholarship council for funding my study and the international student's office at Shanxi University (Miss Liyan, Meiga and the other teachers) who helped me from applying to the scholarship and also during my stay in China.

Sadiq Nawaz Khan

March 2021, Shanxi University.

## Personal Profile

### **Personal Profile**

Name: Sadiq Nawaz Khan

Gender: Male

Native place: Dist. Lower Dir, Khyber Pakhtunkhwa, Pakistan.

Degree duration: 2017/9-2021/6 Ph.D.

Institute of Opto-electronics, Shanxi University, Taiyuan, Shanxi, China

Mobile contact: 15534062849

E-Mail: [zaidan3333@gmail.com](mailto:zaidan3333@gmail.com).

承诺书

## 承 诺 书

本人郑重声明：所提交的学位论文，是在导师指导下独立完成的，学位论文的知识产权属于山西大学。如果今后以其他单位名义发表与在读期间学位论文相关的内容，将承担法律责任。除文中已经注明引用的文献资料外，本学位论文不包括任何其他个人或集体已经发表或撰写过的成果。

作者签名：

2021 年 月 日

## 学位论文使用授权声明

本人完全了解山西大学有关保留，使用学位论文的规定，即：学校有权保留并向国家有关机关或机构送交论文的复印件和电子文档，允许论文被查阅和借阅，可以采用影印，缩印或扫描等手段保存，汇编学位论文。同意山西大学可以用不同方式在不同媒体上发表，传播论文的全部或部分内容。

保密的学位论文在解密后遵守此协议。

作者签名：

导师签名：

2021 年 月 日